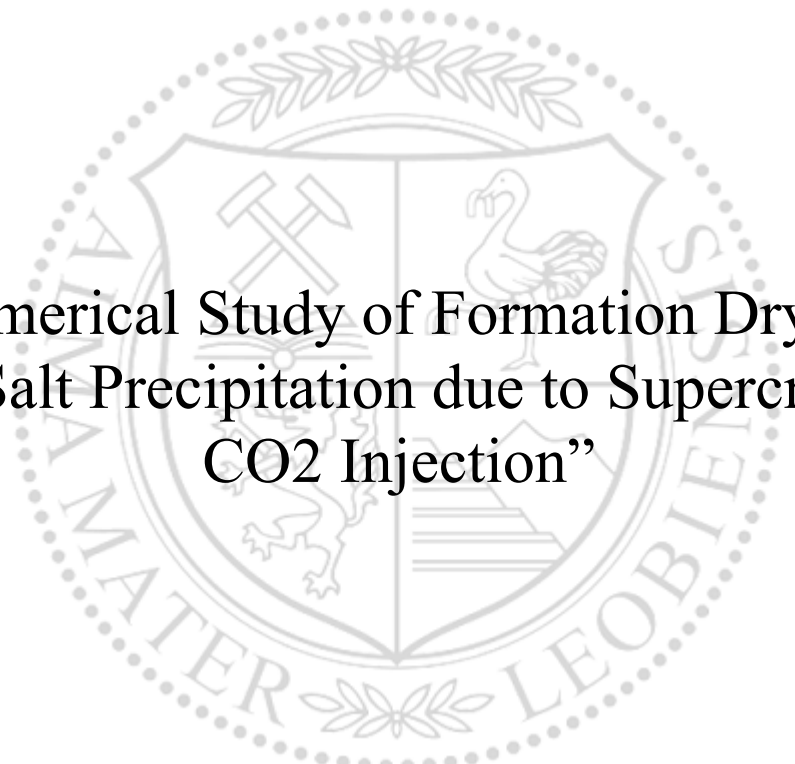




Chair of Reservoir Engineering

Master's Thesis



“Numerical Study of Formation Dry-out
and Salt Precipitation due to Supercritical
CO₂ Injection”

Denis Martynov

November 2022



AFFIDAVIT

I declare on oath that I wrote this thesis independently, did not use other than the specified sources and aids, and did not otherwise use any unauthorized aids.

I declare that I have read, understood, and complied with the guidelines of the senate of the Montanuniversität Leoben for "Good Scientific Practice".

Furthermore, I declare that the electronic and printed version of the submitted thesis are identical, both, formally and with regard to content.

Date 19.11.2022

Signature Author
Denis Martynov

Martynov Denis
Master Thesis 2022
Petroleum Engineering

“Numerical Study of Formation Dry-out and Salt Precipitation due to Supercritical CO₂ Injection”

Utilizing publicly available multiphysics frameworks Dumux and Moose

Supervisor: Univ.-Prof. Dipl.-Phys. Dr.rer.nat.
Holger Ott
Co-supervisor: Dipl.-Ing. Boris Jammernegg

Chair of Reservoir Engineering

To my love Maija, my parents, grandparents, and everyone who contributed to this paper

Acknowledgements

I would like to thank Dipl. Ing. Boris Jammerneegg and Prof. Holger Ott for supervising my work, the time have been allocated to me during brainstorming and evaluating the simulation models and providing insightful ideas to improve my knowledge of underground CO₂ storage.

Finally, yet importantly, I would like to thank my family and friends who always supported me throughout my studies.

Abstract

Climate change has become one of the main concerns for humankind over the last decade, the environmental consequence is linked to the increase in global average temperatures. It can be explained by the gradual increase in greenhouse gas emissions, such as carbon dioxide (CO_2). Therefore, the society aims to become carbon-neutral by 2050. To achieve this target, one of the most promising solutions is Carbon Capture and Storage (CCS), which involves capturing CO_2 from industrial sources or the atmosphere, underground injection, and ultimately storing CO_2 in deep geological formations. The most favorable option includes saline aquifers, because of their high storage capacity potential. The realization of the CCS projects would require highly precise modeling tools, which are capable to describe the geochemical and physical processes, which lead to the evaporation of the saline formation water due to the injection of dry supercritical CO_2 into brine aquifers. This mechanism leads to an increase in brine salinity and salt precipitation, which mainly happens because of water vaporization inside the CO_2 -saturated (dry-out) region. Therefore, permeability and porosity are altered and injectivity impairment arises. It is vital to understand the parameters which enhance salt precipitation, patterns of precipitation, and the displacement process of brine by CO_2 . The study will use publicly available multiphysics frameworks DuMux and Moose to evaluate the displacement process of brine by CO_2 at the near injection region (assuming partitioning phase equilibrium is already achieved). The flow is described by two-phase immiscible displacement, but with slightly mutual solubility between phases. The final target is to analyze the role of different parameters in the salt precipitation process, considering different injection rates and evaluating the role of relative permeability and the stabilizing effect of capillary pressure by using the extended Brooks-Corey and Van Genuchten models. The obtained results and observations were compared with the benchmark simulator TOUGH2, which is utilized as commercial software and can be considered a proven simulator. All simulators - Moose, DuMux, and TOUGH2 are using the same principle of local equilibrium assumption, therefore all of them showed an accumulation of salt near the core inlet consistently with more prominent precipitation under the capillary-driven back flow of brine.

Zusammenfassung

Der Klimawandel ist in den letzten zehn Jahren zu einem Hauptanliegen der Menschheit geworden, dessen wichtigste Umweltfolge der Anstieg der globalen Durchschnittstemperatur ist. Der Temperaturanstieg lässt sich durch die allmähliche Steigerung der Treibhausgasemissionen, wie Kohlendioxid (CO_2), erklären. Daher ist es das Ziel der Gesellschaft, bis 2050 Kohlenstoffneutral zu werden. Um dieses Ziel zu erreichen, ist eine der vielversprechendsten Lösungen, die Kohlenstoffabscheidung und -speicherung (Carbon Capture and Storage, CCS) einzusetzen. Dabei wird das CO_2 aus den industriellen Quellen oder aus der Atmosphäre abgeschieden, in den Untergrund injiziert und schließlich in tiefen geologischen Formationen gespeichert. Die günstigste Option sind salzhaltige Aquifere, da sie über ein hohes Speicherpotenzial verfügen. Die Realisierung von CCS-Projekten würde hochpräzise Modellierungswerkzeuge erfordern, und eines der Hauptprobleme ist die Beschreibung der geochemischen und physikalischen Prozesse, die bei der Injektion von trockenem überkritischem CO_2 in Sole-Aquifere zur Verdunstung des salzigen Formationswassers führen. Dieser Mechanismus führt zu einem Anstieg des Salzgehalts und zu Salzausfällungen, die hauptsächlich durch die Wasserverdampfung innerhalb der CO_2 -gesättigten (ausgetrockneten) Region verursacht werden. Dadurch verändern sich Durchlässigkeit und Porosität, und die Injektivität wird beeinträchtigt. Es ist von entscheidender Bedeutung, die Parameter zu verstehen, die die Salzausfällung, die Muster der Ausfällung und den Verdrängungsprozess der Sole durch CO_2 fördern. In der Studie werden die öffentlich zugänglichen Multiphysik-Frameworks DuMux und Moose verwendet. Mit Hilfe dieser zwei Programmen kann der Verdrängungsprozess von Sole durch CO_2 in der Nähe der Injektionsregion bewertet werden (unter der Annahme, dass bereits ein Teilphasengleichgewicht erreicht ist). Die Strömung wird durch eine zweiphasige, leicht mischbare Verdrängung beschrieben, wobei die primäre Entwässerung dominiert. Das endgültige Ziel ist die Ermittlung der Auswirkungen der ausgewählten Parameter im Salzausfällungsprozess. Darüberhinaus werden verschiedene Injektionsraten berücksichtigt. Weiters wird die Rolle der relativen Permeabilität und der stabilisierenden Wirkung des Kapillardrucks unter Verwendung erweiterter Brooks-Corey- und Van-Genuchten-Modelle bewertet. Die erzielten Ergebnisse und Beobachtungen wurden mit dem Benchmark-Simulator TOUGH2 verglichen, der als kommerzielle Software eingesetzt wird und als bewährter Simulator angesehen werden kann. Alle Simulatoren - Moose, DuMux und TOUGH2 - verwenden dasselbe Prinzip, und zwar die Annahme eines lokalen Gleichgewichts. Aus diesem Grund zeigten alle Simulatoren eine Anhäufung von Salz in der Nähe des Kerneingangs mit einer stärkeren Ausfällung unter dem kapillargetriebenen Rückfluss der Sole.

Table of Contents

Acknowledgements	iii
Abstract.....	iv
Zusammenfassung	v
Chapter 1.....	7
Introduction	7
1.1 Background and Context.....	7
1.2 Scope and Objectives	8
1.3 Achievements.....	8
1.4 Technical Issues	9
1.5 Overview of Master's Thesis	9
Chapter 2.....	11
Literature Review	11
2.1 Introduction / Background	11
2.2 Mechanisms and physics of CO ₂ underground behavior.....	19
2.3 The principals behind the CO ₂ /Brine numerical simulation	22
2.4 Physics behind the salt precipitation mechanisms in saline aquifers during CO ₂ injection.....	34
Chapter 3.....	46
Multiphysics frameworks used in this study	46
3.1 TOUGH2 - ECO2N.....	46
3.2 DuMux	47
3.3 Moose.....	53
Chapter 4.....	55
Results and Discussion	55
4.1 Input parameters.....	55
4.2 Results and Discussion Section.....	59
Chapter 5.....	75
Conclusion.....	75
5.1 Summary	75
5.2 Future Work	76
References	77
List of Figures.....	87
List of Tables	90

Chapter 1

Introduction

1.1 Background and Context

The geochemical and physical mechanisms behind large volumes of continuous CO₂ injection in saline aquifers lead to brine displacement and evaporation. Initially, two-phase immiscible displacement during primary drainage causes water to be pushed out by the injected CO₂. The propagation of the critical CO₂ phase results in the residual water to be trapped in pore throats or bypassed brine in the form of thin film covering grain surface. After the formation of the constantly flowing dry CO₂ stream, this residual brine starts to vaporize into it. Consequently, the continuous evaporation process creates a reactive drying front that propagates into the formation, creating the conditions for the salt mineralization and precipitation of the secondary minerals from the residual brines. Summing up, the most promising Carbon Capture and Storage technology is CO₂ sequestration in saline aquifers however, it brings uncertainties in underground characterization due to significant disequilibrium in the geochemical and physical properties of the reservoir. The existing papers have established that the potential clogging effect on the porosity and permeability near the injection point is controversial, showing that some models have identified a significant reduction in formation properties and others have no impairment. The purpose of this study is to provide the benchmark numerical model, which would be able to mimic the experimental results of the CO₂ injection into the fully brine-saturated Berea sandstone core plug. The main advantage of the provided model is, it can be easily modified and adapted for further investigation, after performing the laboratory experiment, due to publicly available multiphysics frameworks code.

1.2 Scope and Objectives

In this study, publicly available multiphysics frameworks DuMux and Moose were used to simulate and analyze CO₂ plume migration in a saline aquifer. The objective was to evaluate the abilities of these simulators in predicting salt precipitation during CCS operations and prove the existence of an effective porosity reduction and hence, permeability. In addition, to determine the key processes controlling the drying of the porous media during the injection of dry gas, and identify the parameters needed to predict the behavior of the salt (dissolved and solid) inside the core. The sensitivity analysis was performed, where parameters, such as - injection rate, capillary forces back flow (using different equations) and relative permeability were tested. For the evaluation, the obtained results and observations were compared with the benchmark simulator TOUGH2, which is utilized as commercial software and can be considered a proven simulator. The experimental conditions from the CT-lab experiment were mimicked and introduced into the simulator. The simulation setup was described by one meter, ten centimeters in diameter core plug, which was generated in GMSH software. The conditions for the experiment assume 100 bar pressure and 45 degrees temperature to achieve supercritical conditions for CO₂ injection, which corresponds to a pressure and temperature windows in a depth of about 1000 meter. The scenario will require the injection rates of 2 and 20ml/min, the recordings will be made after 1, 5, 10 and 25.5 pore volumes injected.

1.3 Achievements

The numerical models for this thesis were built and demonstrated that it would be possible to achieve the desired simulation work with only one assumption where the local equilibrium approach is applied to CO₂ injection modeling. Both simulators used in this study were able to precisely reproduce both the propagation of the CO₂ saturation front within represented core plug domain and the salt precipitation at the inlet with a given brine salinity and various injection parameters. The displacement process has shown a strong dependency on the Relative Permeability – Saturation – Capillary pressure model, which is signified by the large variations in plume extent and saturation distribution. Further, the geochemical and physical mechanisms, such as two-phase brine displacement by the injected front, vaporization of residual brine into the dry CO₂ phase, molecular diffusion of dissolved salt into the aqueous phase, and enhanced brine mineralization due to capillary forces, were well reproduced using laboratory experiment scale and slightly heterogeneous porous domain. The results have revealed that the salt precipitation mechanism was initiated only in the dry-out region around the injection boundary, excluding the two-phase zone beyond the dry-out region.

1.4 Technical Issues

The main challenge has come due to the absence of proven results from the laboratory experiment, which has been performed on an identical scale. This may be the reason that there are just very few CO₂ numerical simulation experiments reported in the literature, which would include not only displacement mechanism but vaporization of brine into the dry supercritical CO₂ front. Another issue has arisen due to the non-iterative mass transfer approach between the brine phase and the CO₂ phase. Since 2005 (Spycher and Pruess, 2005; Spycher et al., 2003) there were limited attempts to create the kinetic model for phase partitioning. Therefore, most of the simulators are still considering the non-iterative local equilibrium phase partitioning assumption. According to this approach, the solubility of the displacing phase in the displaced phase happens instantaneously, approximately 5% of the CO₂ is immediately dissolved after contacting the brine, which leads to the fact that the reaction rate becomes infinite. Some projects have revealed that the local equilibrium assumption does not correspond to the real physical and geochemical mechanism inside the porous medium and the mass transfer occurred along the whole length of the core. However, the experiments on the bigger scale are still in progress and the reaction kinetic data is pending for the kinetic model update and progressive development.

1.5 Overview of Master's Thesis

In this master's thesis, for the background, it is important to provide the most recent update regarding the path to the net-zero transition via CSS (Carbon Capture and Storage), the most recent projects and technologies, mainly associated with storage in saline aquifers, the discussion is provided in Chapter 2. The geochemistry and physics description behind salt precipitation and previous numerical simulations work for the CO₂ injection, including the analytical approach for the reaction kinetics model are revised. The most recent ambiguities between static equilibrium and kinetic models in the literature were identified and, therefore, the shortcomings of the clogging models used for numerical simulations. The models' setup and mathematical explanation behind the simulation mechanism are fully described in Chapter 3. The description and capabilities of the publicly available multiphysics frameworks – DuMux and Moose, are extensively provided in Chapter 3 as well. Chapter 4 discusses the obtained results and compares them with the TOUGH2 simulator, the main observations include the influence of the injection rate, the effect of the capillary forces, different mobility ratios from the relative permeability curves, and the salt patterns formed.

Chapter 2

Literature Review

2.1 Introduction / Background

The recent report of the Intergovernmental Panel on Climate Change (IPCC) (2022) has revealed that there is ongoing climate change leading to related consequences, like global warming and temperature increase. The main reason for such changes is the abundance of heat-trapping greenhouse gases in the atmosphere, such as CO₂ (Carbon Dioxide) and CH₄ (Methane). The purpose of greenhouse gases is to maintain natural processes, and ensure that the heat exchange between the atmosphere, surface, and reflection of the excess into space is in equilibrium, keeping the planet's temperature stable. However, due to humankind's activity more emission of greenhouse gasses has been reflected, as a result, more heat was trapped, and the Earth's temperature has increased. The sources of the GHG emissions can be allocated to the five broad sectors, distinguished in the Intergovernmental Panel on Climate Change (IPCC) Working Group III (WG3) as energy systems, industry, buildings, transport, and AFOLU (agriculture, forestry, and other land use) (W. F. Lamb *et al*, 2021). It was mentioned that anthropogenic sources which are described by burning fossil fuels, the metallurgy industry, deforestation, cement manufacturing, etc., have significantly altered the exchange rates between surface and atmosphere, leading to alarmingly more carbon flux, breaching the established nature eco-system (Carlson *et al.*, 2009; Hannah, 2015; Steele *et al.*, 2009). For example, only from the fossil fuel industry, it was predicted that existing and planned petroleum infrastructure alone could reach 850 Gt, which exceeds the agreed limit by over 340 Gt (Figure 1). The recent statistics from the IPCC report (2022) have confirmed the tendency of the increasing concentration of GHG emissions, reaching 59 gigatonnes of CO₂ equivalent (GtCO₂e) in 2019 — roughly 12% higher than emissions in 2010 and 54% greater than in 1990 (Figure 1). In 2015, the Paris Agreement (2015) it was mentioned that is vital is utilize all the

possible mitigation pathways to limit warming to 1.5 – 2 °C above pre-industrial levels. In addition, it was predicted using a modelled pathway that the GHG emissions peak will be reached by 2025 and then fall by 43% by 2030.

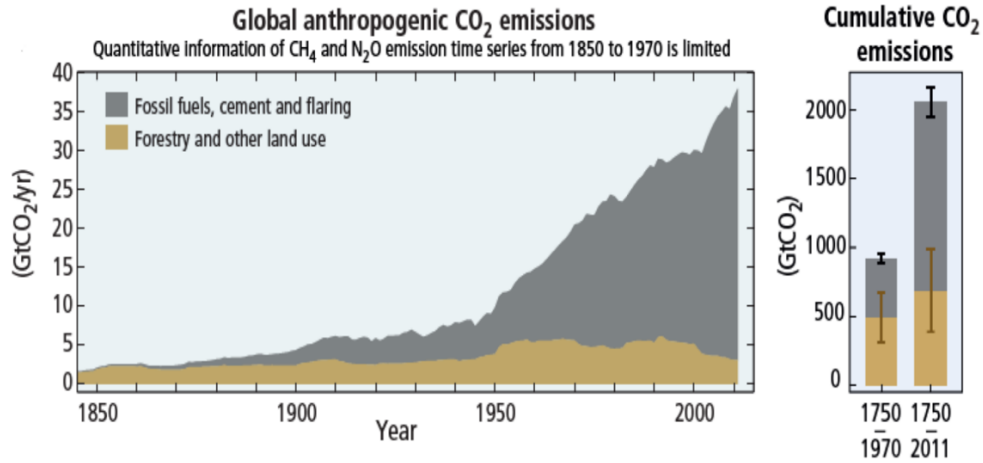


Figure 1 Globally averaged greenhouse gas concentrations and global anthropogenic CO₂ emissions (IPCC, 2014).

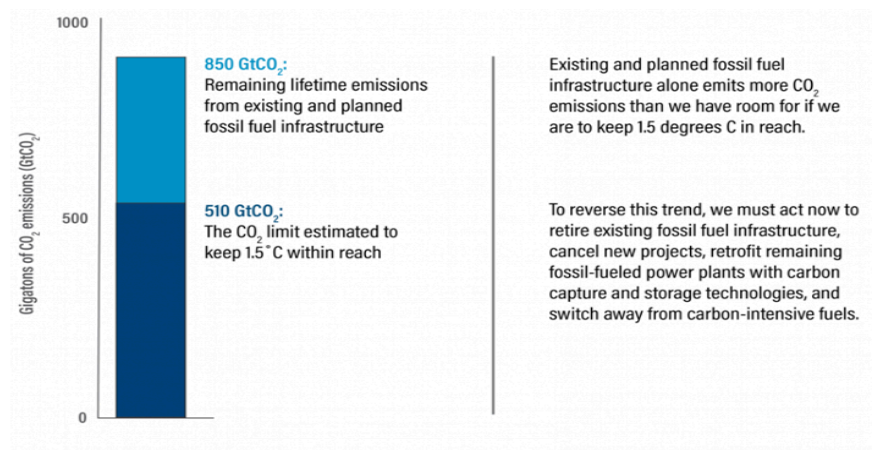


Figure 2 Comparison of CO₂ emissions from fossil fuel projects vs. global CO₂ limits (C. Schumer et al, 2022).

From Figure 3 it is visible that the averaged atmospheric CO₂ concentration was constantly gradually rising and reached a new high of 413.2 ppm in 2020. However, as can be seen on the right graph, there is a reduction trend in the CO₂ concentration growth rate between 2019 to 2020, but overall growth was larger than the average annual growth rate over the last decade. This year society has seriously thought about the consequences of global warming, in addition to the reduction of approximately 5.6% in fossil fuel CO₂ emissions in 2019-2020 due to the COVID-19 restrictions and the agreement of OPEC+ to decline the production by extra 500,000 barrels of oil a day from the global market (OPEC, 2019). Nevertheless, the situation is worsening day by day because of constant perturbations of the ecosystem due to droughts and

the melting of the polar icecaps, and consequently, the increasing ocean levels. The ability of these ecosystems and oceans to act as “sinks” is reducing, thus their ability to absorb CO₂ is suppressed and the natural “shield” is at stake against larger temperature increases.

Carbon Dioxide (CO₂)

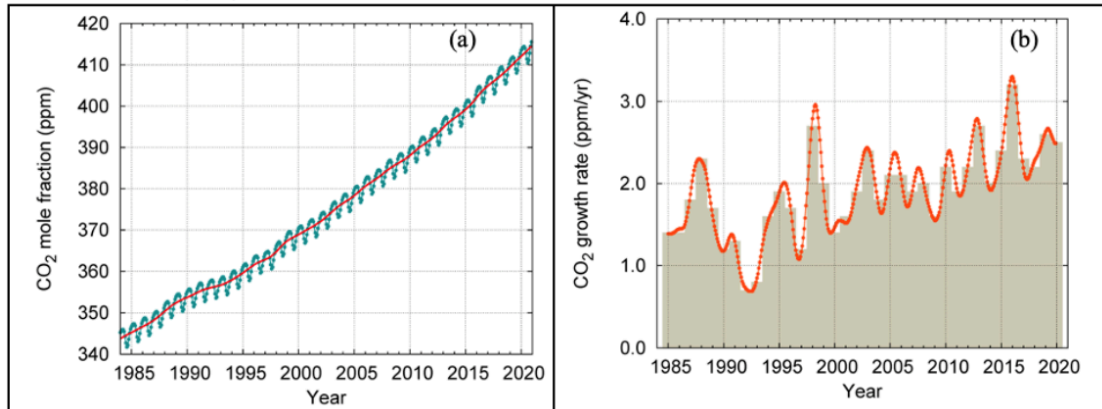


Figure 3 Globally averaged CO₂ mole fraction (left) and its growth rate (right) from 1984 to 2020. Increases in successive annual means are shown as the shaded columns on (right). The red line on (left) is the monthly mean with the seasonal variation removed; the blue dots and blue line on (left) depict the monthly averages (WMO Global Atmosphere Watch, 2021).

Different strategies are trying to achieve the net-zero path of the CO₂ emissions, considering: retiring unproductive fossil fuel infrastructure, avoidance of the new carbon-inefficient projects, retrofitting fossil-fueled power plants with carbon capture and storage (CCS) technologies, and switching to energy-efficient, lower-carbon fuels (for example, coal to natural gas) or prioritize the usage of renewable and nuclear energy sources. Carbon Capture and Storage (CCS) has become an indispensable tool and a great reflection of humanity’s efforts to withstand climate change and reach its goal of net-zero emissions. The most demanding energy industries as diverse as iron and steel, cement, natural gas, electricity generation, refineries, and fertilizer production can reduce the emission output by utilizing the ability of CCS. The recent innovative steps into carbon dioxide removal (CDR) are the applications of Direct Air Capture (DAC) and Bioenergy with CCS (BECCS) (IEA, 2022), capturing historical CO₂ emissions from the atmosphere. From that first indirect attempt to store CO₂ (injection was used as EOR) in 1972 to today, the term “CCS” has grown to a global project and relief for the heavy industry, with 26 CCS facilities currently in operation around the world that were managed to capture and sequester 300 million metric tons of CO₂ (P. Loria 2021). Nevertheless, future CCS projects provide promising results regarding storage capacity, but the number of projects is not enough for a considerable impact on climate change. To achieve the requirement of IEA SDS, 5,635 Mtpa of CO₂ must be stored by 2050, which demands 70–100 new facilities annually (Townsend and Gillespie, 2020).

The storage capacity and well injectivity are the parameters to review for the storage potential and success of a CCUS project. There are several suitable geological formations for carbon dioxide storage to consider: depleted oil and gas reservoirs, sequestration through enhanced oil recovery (EOR), coal seams, and deep saline aquifers (Figure 4). In terms of economic feasibility, CO₂ application in (EOR) projects and sequestration in depleted oil and gas reservoirs, are currently assumed to be the most economically attractive options. CO₂ storage in geothermal reservoirs would also be prescribed for this category. However, the highest storage potential in terms of volume available to hold CO₂ is related to the saline aquifers (Intergovernmental Panel on Climate Change, 2005). To sum up, the perspective of geological storage can be confirmed by the example of the natural carbon dioxide reservoir, where CO₂ was stored over millions of years. The Pisgah field was discovered by Shell in 1960 with tremendous amounts of CO₂ under the Mississippi river (Shell, 2015).

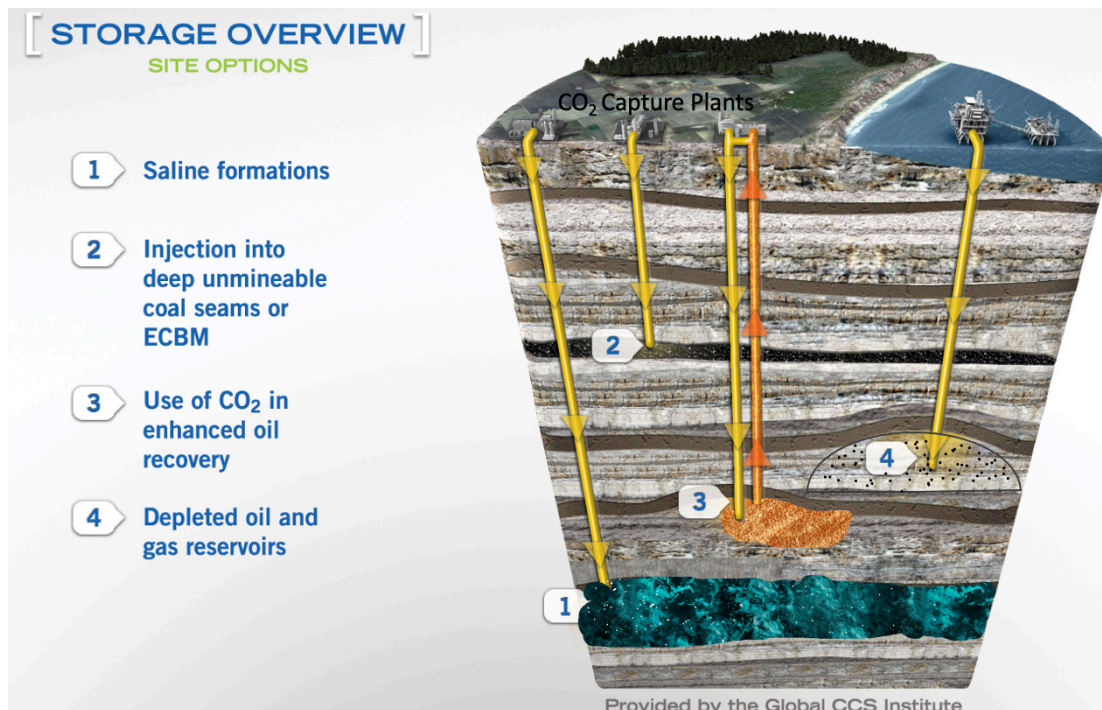


Figure 4 Overview of the suitable geological formations for carbon dioxide storage (Global CCS Institute, 2022).

The first example of a successful storage project is related to the facility which was in operation since 1972, the Terrell Natural Gas Plant (US), it utilizes CO₂ in the Enhance Oil Recovery application and still permanently captures and stores at a rate of 0.4 Mtpa. Another significant successful attempt was made at the Shute Creek Gas Processing Plant in the US, it can capture 7 Mtpa annually, making it the largest industrial Carbon Storage project in the world (P. Loria 2021). In addition, good results were achieved for Sleipner and Snohvit in Norway (Maldal and Tappel, 2004; Torp and Gale, 2004), Weyburn in Canada (Preston et al.,

2005), and Quest in Canada (Shell, 2015). As can be noted from Figure 5, the leading CCS project countries are still the US and Canada, however, promising intentions are made by China as well. Nevertheless, as was already mentioned, these facilities are not enough to reach climate goals. The possibility of the such slow development of the CCS industry would be described by uncertainties in CO₂-capturing technologies and underground processes related to the interaction between carbon dioxide and highly saline brines. Bette and Heinemann(1989) and Miri; Hellevang (2016) have assumed that injection of CO₂ into a very saline environment would lead to mineralization and precipitation of salts, like Halite, after reaching critical CO₂ saturation, hence, evaporation of the brine into the dry-CO₂ phase. This mechanism has side effects on porosity and permeability reduction, leading to major injectivity impairment problems. To make the CCS projects efficient, it is important to consider impairment issues, otherwise, it would require drilling more wells, because maintaining high injection rates within one well, potentially could lead to formation clogging and pressure drop (Kim et al., 2012, p. 398) (Miri et al., 2015) (Peysson, 2012).

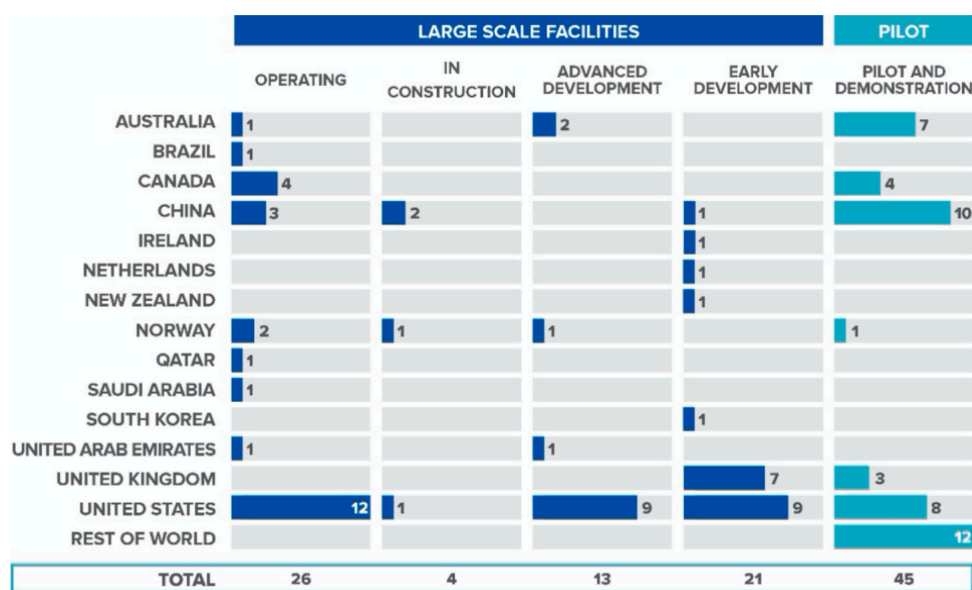


Figure 5 Number of CCS facilities by scale, location, and phase of development as of June 2021 (P. Loria 2021).

For geological disposal, the trapping processes of CO₂ can be differentiated into two major mechanisms – physical and geochemical (Figure 6). These stages are well represented as the function of time in Figure 7. Physical trapping is a mostly instantaneous process, by means, the storage operation is initiated just after the CO₂ injection and tends to last less than a century (Juanes et al. 2006). The first physical barrier to be encountered is structural trapping, mainly it is a tight sealing rock on top of a formation that avoids the upward migration of CO₂. During the storage procedure, carbon dioxide is maintained in either the supercritical or the gas phase as a function of depth at the associated pressure and temperature. The propagation of the CO₂

front can be described by the domination of the viscous forces (T. Ajayi et al, 2019). From the start of the injection, the supercritical CO₂ tends to form the plume, which migrates upward through the porous and permeable rock due to the buoyancy effect under the influence of density difference compared to the host fluids, for example, brine, and laterally via permeable pathways, reaching cap rock, fault, or other sealed structures (Han, 2008). This will maintain the CO₂ under the “cap” and prevent further migration. The best example to describe structural trapping is the salt dome formations. Another physical process of CO₂ sequestration can be described by acting capillary forces or residual trapping. This mechanism is an example of immobile trapping, where capillary forces prevail over viscous and buoyancy forces, leading to CO₂ trapping without the existence of a physical barrier (Bennion, 2010). Saadatpoor et al. (2010) have suggested that surface tension between CO₂ and host fluid prevents the CO₂ from migration, it can be explained by higher capillary entry pressure than the average pore pressure, leading to immobilization of the CO₂ in the pores at residual gas saturation. Such behavior is typical for rocks with small-scale capillary heterogeneities (T. Ajayi et al, 2019). According to recent observations, it was proposed that capillary trapping provides better efficiency for CO₂ underground disposal, but mainly in the short-term perspective (Burnside and Naylor 2014; Lamy et al. 2010). In addition, it minimizes the risks of major failure related to stratigraphic traps over a short time scale.

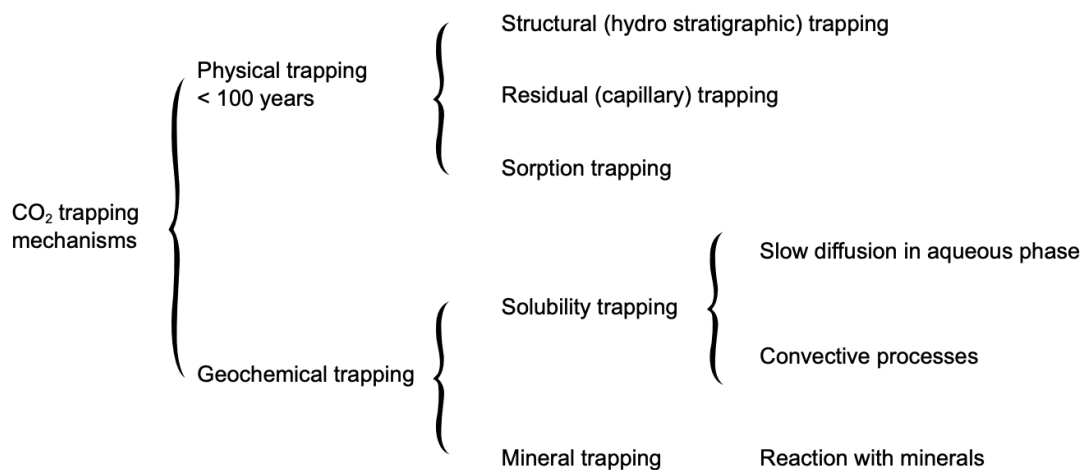


Figure 6 Different CO₂ trapping mechanisms during the geological storage process (T. Ajayi et al, 2019).

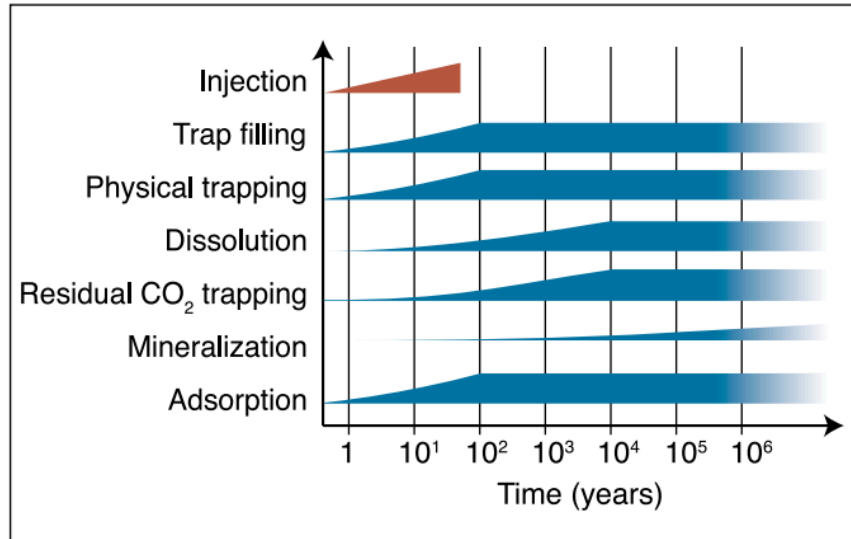
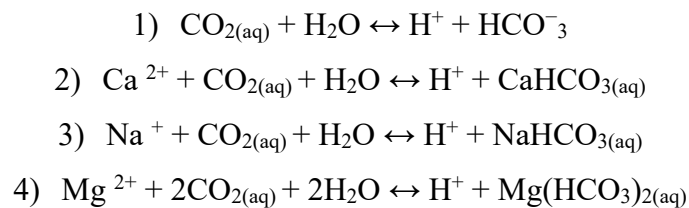


Figure 7 Governing processes after the injection of CO₂ into saline aquifers (IPCC Special Report, 2005).

In the case of geochemical trapping, it occurs when CO₂ interacts with the formation brine and the rock employing geochemical reactions, suspended to reside in the mobile phase – solubility trapping or immobile phase – mineral trapping. This solubility trapping signifies the dissipation of CO₂ as a separate phase, providing the opportunity for massive storage capacity, and leading to the long-term, most efficient, and stable storage option for CO₂ underground disposal. T. Ajayi et al (2019) have described the solubility trapping in a similar procedure, where sugar dissolves in hot water during a tea or coffee break. In the same manner, CO₂ dissolves in brine in both supercritical or gaseous states, leading to denser CO₂-saturated brine and, hence, the downward fingering of this compositional phase, which eliminates any buoyancy effect. The CO₂-saturated brine sinks to the bottom of the formation over time, providing secure storage. The solubility trapping is manifested by the formation of insoluble ionic species as described below Eqn. 1- 4, but mainly weak carbonic acid (Eq. 1). The CO₂ dissolution in the formation brine is strongly controlled by an increase in temperature and salinity, as a result, solubility decreases.



The mineral trapping happens due to the conversion reactions between CO₂ and solid minerals, causing calcite precipitation. However, the reaction process is relatively slow, because it is initiated just after solubility trapping, but considered the most permanent and secure storage

mechanism. In contact with the aqueous phase, carbon dioxide results in weak acid, then bicarbonate ions are formed after a reaction between acid and resident rock, which are influenced by the mineralogy of the formation. For example, potassium basic silicate (Eq. 5) and calcium (Eq. 6) are formed, the reactions are shown below. The geochemical effects gain importance due to influence on the rock permeability and porosity (Benson and Cole 2008; Darcis et al., 2011). The formation impairment problems have gained extreme importance in predicting the success of the CCS operation, mainly geochemical modeling is vital for the analysis of the future carbon storage plays. The visual representation of the trapping mechanisms is well described in Figure 8.

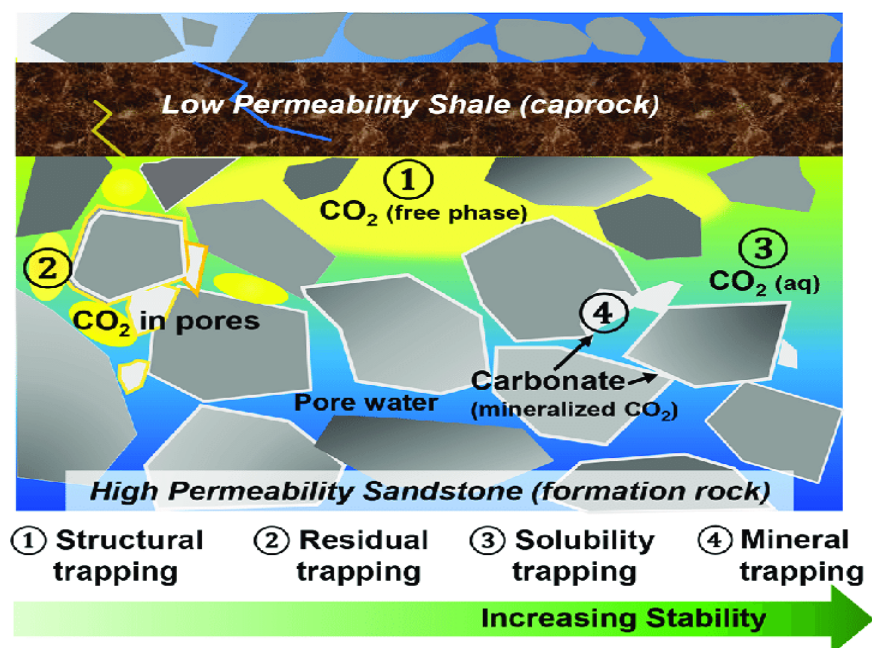
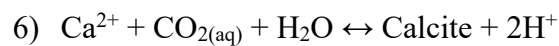
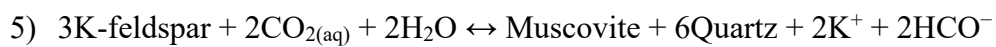


Figure 8 CO₂ trapping mechanisms at Geologic CO₂ Sequestration sites (Jun, Young-Shin & Zhang, Lijie & Min, Yujia & Li, Qingyun., 2017).

2.2 Mechanisms and physics of CO₂ underground behavior

Injection of CO₂ requires storage which provides sufficient depth, hence, temperature and pressure exceed the CO₂ critical point ($T \sim 31.1$ °C; $P \sim 73$ Bar), making the carbon dioxide supercritical (Figure 9). Supercritical CO₂ is superior compared to other phases because it provides the density of the liquid - between about 250 and 800 kg/m³, and viscosity of the gas, so the main benefits are related to the injectivity and storage capacity (Celia et al., 2015). While a significant volume of CO₂ can be stored per volume of pore space, the density of the formation brine is still higher, and CO₂ is only slightly soluble, hence, the injected phase will remain as a separate fluid phase for a significant period. The injection and post-injection periods of CO₂ storage in saline aquifers can be described by many physical mechanisms, including buoyancy (gravity migration), and viscous and capillary forces. The injection phase is mainly characterized by viscous forces in the vertical and lateral directions and the movement is explained by the pressure gradient. Then, the displacement process starts, and the plume migrates as primary drainage of immiscible fluids if the fluids are mutually saturated (Ott et. al, 2014), where both buoyancy and capillary forces act to trap the CO₂. The relative permeability and capillary pressure are the important parameters to consider for the plume evolution in deep saline aquifers, as they have a great impact on CO₂ saturation distribution and residual saturation, hence, trapping. The macroscopic displacement efficiency is predominantly determined by relative permeability and capillary pressure functions. The main impacts to consider are described by the spatial extent of the CO₂ plume, the extent of capillary trapping, and the injectivity of the well. The post-injection migration, mainly plume extension is described by the drainage along the leading edge of the propagating CO₂ plume and imbibition along the trailing edge. Consequently, the imbibition along the trailing edge leaves some carbon dioxide trapped behind the migrating plume of the CO₂, at residual saturations or slightly above corresponding to CO₂ (Celia et al., 2015).

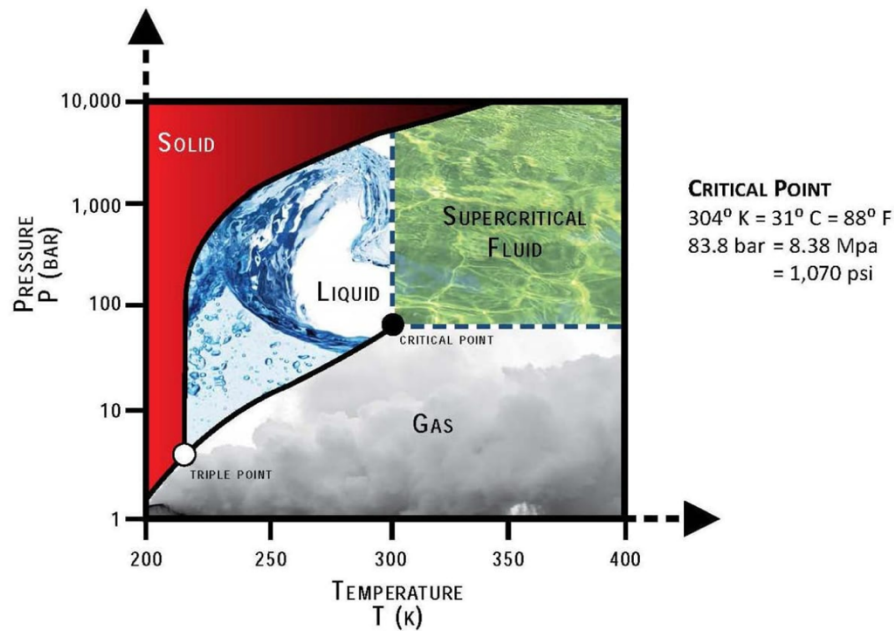


Figure 9 Phase diagram of CO₂ (S.Patel, 2019).

In addition, the phenomenon hysteresis occurs after the drainage and imbibition-like processes, which can signify the pathways change of the capillary pressure and relative permeability curves. It was suggested that hysteresis is vital for the precise description of the trapping processes related to CO₂ modelling (Juanes et al. 2006). The injected carbon dioxide migrates upwards due to density difference, however, the series of blobs is observed at the top, because water displaces CO₂ at the trailing edge and the remaining CO₂ plume gets disconnected. These blobs are characterized by the CO₂ trapped inside and dissolving in the brine under the governance of residual or capillary forces. This dissolution is manifested by three principal mechanisms:

- (a) diffusion of CO₂ into the water phase.
- (b) geochemical reactions with the host rock and minerals (mineral trapping).
- (c) convective mixing, described by the density difference between the saturated brine with dissolved CO₂ and the unsaturated brine (T. Ajayi et al, 2019).

According to Ennis-King and Paterson (2003), long-term dissolution is governed by the prevailing mechanism of convective mixing rather than pure diffusion. Convective mixing is much faster and leads to gravitational instabilities, bringing additional benefit to solubility trapping. The mentioned above properties are strongly connected to the heterogeneity and wettability of the aquifer. Heterogeneity is described by the small and large scales. For the small scale, viscous and capillary forces are responsible for the flow, and gravity forces are usually neglected. Considering the large scales, the formation possesses are dependent on the variable pore throat sizes, which are responsible for the different capillarity. The difference in capillarity

pressure is strongly connected to the amount of injected CO₂ required to displace the formation brine, resulting in more volume of CO₂ being trapped as the entry pressure is overcome (T. Ajayi et al, 2019). Wettability and interfacial tension are also integral attributes in governing the underground flow processes. It was proposed that changes in them would mostly alter the capillary pressures in a porous medium (Bennion and Bachu, 2006; Jung and Wan 2012; Park et al. 2015; Yang et al. 2005). In most cases, CO₂ is referred to as the non-wetting phase, while water is the wetting phase, however, the conditions may change during the CO₂ upward migration. As can be noted from Eq. (7) (Young–Laplace equation), there is a straight dependency between Pc (capillary pressure), the pore throat size (R), the interfacial tension (σ), and the contact angles (θ) between the wetting fluid and the rock surface.

$$7) P_c = P_{CO_2} - P_w = \frac{(2\sigma_{w,CO_2} \cdot \cos\theta)}{R}$$

The main attention of this thesis is dedicated to the process of water evaporation into the CO₂-rich phase when the dry CO₂ is injected. In this section, the mechanism of dry-out and precipitation is just briefly explained. The injection of dry-CO₂ leads to water evaporation into it, until the CO₂ phase becomes reached with water vapor, to form “wet” CO₂, leaving the dry-CO₂ behind. Consequently, the dry-out zone near the injection well and so-called “drying front” (leading edge of the dry zone) is formed, where eventually all the water in this area has evaporated (Celia et al., 2015). In the case of injection in the highly saline aquifer, brine is evaporated, leaving the precipitated salt in the pore space (Pruess and Muller, 2009). From Figure 10 the sharp interface between the invading CO₂ front and the drying front can be noted.

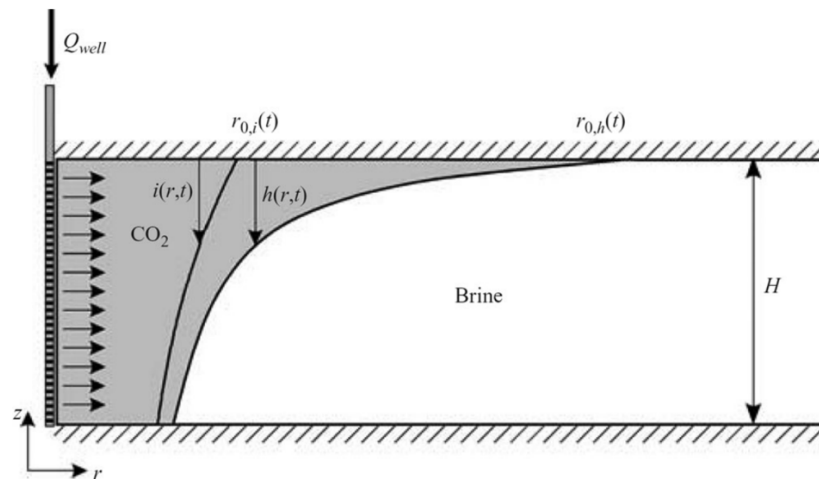


Figure 10 Schematic of the CO₂ injection front, with the thickness of the CO₂ denoted by $h(r,t)$, and the drying front, with thickness denoted by $i(r,t)$ (Nordbotten and Celia, 2006a).

2.3 The principals behind the CO₂/Brine numerical simulation

For the successful CSS implementation at a real field scale, it is vital to test the number of “what ifs” utilizing efficient numerical tools. These simulation tools are essential in all phases of the CCS deployment, from the project planning phase to the post-injection/plume migration phase. In addition, the numerical simulations can provide benefits in estimating the storage capacity of the reservoir, evaluation of the risk assessment and efficient injection strategies, mitigation of the hydraulic properties reduction and options for tracking CO₂ underground behavior under the governance of certain reservoir conditions, such as formation pressure, temperature, permeability, porosity, relative permeability, capillary pressure, assessment of plume extent and shape, and monitoring the leakage potential and formation clogging. In the ideal case, numerical simulators should be capable of mimicking the four primary trapping mechanisms for CO₂ storage, which were described before (Doughty, 2010). In general, numerical simulators are based on the multiphase, multicomponent framework, including non-isothermal behavior, with advection term, diffusion and dispersion of fluid components, and conduction and advection of heat. To describe the fluid properties during the flow, a specialized, high-accuracy equation of state for CO₂ and brine is required. Nevertheless, the auxiliary important parameter in the description of CO₂/Brine displacement is the formulation of the mutual solubility of CO₂ into the liquid brine and vice versa water into the CO₂-rich gas phase. The majority of numerical simulators assume the CO₂/Brine displacement is immiscible with instantaneous mutual solubility. By instantaneous it means after the first contact the phases are mutually saturated, for example in some studies the first contact (instantaneous) solubility is stated to be around 5% by mass dissolving into the brine, and less than 1% by volume of H₂O, can evaporate into the CO₂ phase (Celia et al., 2015).

Mathematical models are an integral part of the description of the fluid movement in the subsurface. The basis of every numerical simulator starts from the mass balance equations governing the flow of multiphase, multicomponent fluids in permeable media. For example, TOUGH2 uses the integral finite difference method (IFDM) to solve the mass and heat balance equations. The system includes NK components and NPH phases in equilibrium, the formulation can be written in the following Eq. (8) (K.Pruess, N.Muller, 2009):

$$8) \quad \frac{d}{dt} \int_{V_n} M^k dV_n = \int_{\Gamma_n} F^k d\Gamma_n + \int_{V_n} q^k dV_n$$

The investigated flow system is integrated over an arbitrary subdomain V_n . The flow is bounded by the closed surface Γ_n . The quantity M (on the left part of eqn.) represents the

accumulation term, which is described by mass per volume, with $k = 1, \dots, NK$ denotes the components that participated in the flow (H_2O , $NaCl$, CO_2). The term F governs mass flux (Eq. 12), and q indicates sinks and sources. The unit n defines the normal vector on surface element $d\Gamma n$, pointing in the direction of Vn . The Eq. (8) can be described by the rate of fluid mass change in Vn , which is equal to the net inflow across the surface of Vn , plus net gain from injection or any other source (K.Pruess, N.Muller, 2009).

The accumulation term is provided by Eq. (9), where the mass of species κ per volume of rock is written as a sum over all phases (liquid, gas, and solid phases) β present in the system:

$$9) M^K = \varphi \sum_{\beta} S_{\beta} \rho_{\beta} X_{\beta}^K + (1 - \varphi) C^K$$

Where φ denotes the porosity, S_{β} is the saturation of phase β , ρ is the density of phase β ($kg.m^{-3}$), and X_{β}^K is the mass fraction of component κ present in phase β . The final term on the right side describes the fluid absorption into the porous rock where C^K is the mass of adsorbed component per volume of solid rock-grain material ($kg.m^{-3}$). In addition, the density ρ_{β} is typically a function of pressure and temperature but also depends on the mass fraction of individual components, as described in the specific equation of state used in each model. These equations are bounded by constitutive equations for the saturation and mass fractions, obeying the following equations (C. Green et al, 2018).

$$10) \sum_{\beta} S_{\beta} = 1 \text{ saturation fraction}$$

$$11) \sum_k X_{\beta}^k = 1 \text{ mass fraction}$$

The fluid flux is a sum of the advective flux (sum over all phases in equilibrium) and diffusive-and-dispersive flux:

$$12) F^k = \sum_{\beta} X_{\beta}^k F_{\beta}^{advective} + F_{diffusion+dispersion}^k$$

From Eq. (12), $F_{\beta}^{advective}$ - advective flux of each phase is described by a multiphase version of Darcy's law, where each phase has its density (ρ_{β}), relative permeability ($k_{r,\beta}$), viscosity μ_{β} ($kg.m^{-1}.s^{-1}$), and pressure P_{β} (Pa):

$$13) F_{\beta}^{advective} = \rho_{\beta} v_{\beta} = -\rho_{\beta} \frac{k k_{r\beta}}{\mu_{\beta}} (\nabla P_{\beta} - \rho_{\beta} g)$$

In the Darcy's equation above (13), v_{β} is the Darcy velocity $m.s^{-1}$ (volume flux) in phase β , k (m^2) is absolute permeability, $k_{r\beta}$ is the relative permeability of the phase β and is a function of the saturation, μ_{β} is viscosity, and P_{β} (the fluid pressure of the certain phase) is the sum $P_{\beta} = P_{\beta} + P_{c\beta}$, where P_{β} is the reference pressure (usually taken to be the gas phase), and $P_{c\beta}$ is the

capillary pressure of the investigated phase (often a function of effective saturation), g is the vector of gravitational acceleration.

Most of the numerical simulators also consider diffusive and dispersive fluxes in all phases, in addition to coupling between diffusion and phase partitioning, this can be very beneficial in investigating volatile solutes in multiphase conditions (Pruess, 2002).

$$14) F_{diffusion+dispersion}^k = - \sum_{\beta} \rho_{\beta} D_{\beta}^k \nabla X_{\beta}^k$$

D denotes the hydrodynamic dispersion tensor ($m^2 \cdot s^{-1}$):

$$15) D_{\beta}^k = D_{\beta,T}^k I + \frac{D_{\beta,L}^k - D_{\beta,T}^k}{v_{\beta}^2} v_{\beta} v_{\beta}$$

$$16) D_{\beta,L}^k = \phi \tau_0 \tau_{\beta} d_{\beta}^k + \alpha_{\beta,L} |v|_{\beta}$$

$$17) D_{\beta,T}^k = \phi \tau_0 \tau_{\beta} d_{\beta}^k + \alpha_{\beta,T} |v|_{\beta}$$

$D_{\beta,L}^k$ and $D_{\beta,T}^k$ are the longitudinal and transverse dispersion coefficients, d_{β}^k means the molecular diffusion coefficient corresponding to the k component and β phase ($m^2 \cdot s^{-1}$), $\tau_0 \tau_{\beta}$ is the tortuosity, including porous medium dependent factor τ_0 and a coefficient τ_{β} – which depends on phase saturation, and α_L and α_T are the longitudinal and transverse dispersivities (m) (C. Green et al, 2018). Optionally, the hydrodynamic dispersion model, which is described by Fick's law, can be implemented upon request (K.Pruess, N.Muller, 2009).

To describe the heat flow for the non-isothermal models, energy conservation for heat is required. Most simulators are assuming that the liquids and solids are in local thermal equilibrium, so there is a single temperature for all phases. The heat flow can be explained by the continuity Eq. (18):

$$18) 0 = \frac{\partial \epsilon}{\partial t} + \epsilon \nabla * v_s + \nabla * F^T - v(1 - \phi) \sigma_{ij}^{eff} \frac{\partial}{\partial t} \epsilon_{ij}^{plastic} - q^T$$

From the Eq. (18) above, E denotes the heat energy per unit volume in the rock-fluid system ($J \cdot kg^{-1}$), v_s represents the velocity of the porous solid skeleton ($m \cdot s^{-1}$), F^T describes the heat flux ($J \cdot m^{-2} \cdot s^{-1}$), σ_{ij}^{eff} is the ratio of plastic-deformation energy to heat energy, σ_{ij}^{eff} is the effective stress (Pa), $\epsilon_{ij}^{plastic}$ is the plastic strain, and q^T is an external heat source/sink ($J \cdot m^{-3} \cdot s^{-1}$). The solid mechanics terms are represented by the $\epsilon \nabla * v_s$ and $v(1 - \phi) \sigma_{ij}^{eff} \frac{\partial}{\partial t} \epsilon_{ij}^{plastic}$, as well as via changes in porosity and permeability (C. Green et al, 2018).

To model the flow of CO_2 /Brine in porous media of the saline aquifers, the thermophysical properties must be calculated, including density, viscosity, partitioning of components among the fluid phases, and specific enthalpy. These parameters are strongly related to the temperature, pressure, and composition of the flowing phases.

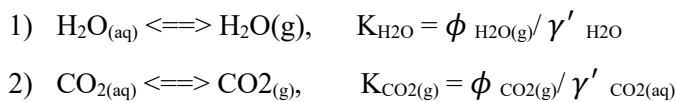
The fluid properties of the gas phase are mainly calculated using the equation of state. For example, the TOUGH2 simulator uses the cubic EOS summarized in Spycher and Pruess (2010), and Moose and DuMux calculations are based on the Span and Wagner EOS (Span and Wagner, 1996). Viscosity is calculated using the formulation presented in Fenghour et al. (1998) or Vesovic et al. (1990), while thermal conductivity is taken from Scalabrin et al. (2006) (C. Green et al, 2018).

The aqueous phase density, on the example of the TOUGH2 simulator (Pan et al., 2015), is calculated assuming the additivity of the volumes of brine and dissolved CO₂ (Eq. 19). The density of the brine and dissolved salt is provided as in Battistelli et al. (1997) from the correlations of Haas (1976) and Andersen et al. (1992). The impact of dissolved CO₂ and the density of CO₂ by itself is determined as a function of temperature. The appropriate correlation was proposed by García (2001), where the molar volume of dissolved CO₂ is found at infinite dilution. Brine viscosity is found from a correlation presented by Phillips et al. (1981) and the viscosity of pure CO₂ is provided as a function of pressure and temperature, obtained through bivariate interpolation from a tabulation of CO₂ viscosity using the correlations developed by Altunin (1975).

$$19) \frac{1}{\rho_{aq}} = \frac{1-X_2}{\rho_b} + \frac{X_2}{\rho_{CO_2}}$$

Where X_2 denotes the mass fraction of CO₂ in the aqueous phase, and ρ_{CO_2} is the partial density of dissolved CO₂.

Dissolution of CO₂ into pure water, as for liquids with very low miscibility, is calculated using Henry's. where the Henry constant for the solutes and the saturated vapor pressure are both divided by phase pressure. However, this formulation is only valid for pure water and CO₂ dissolution. The modelling of the CO₂ injection into saline aquifer requires a different mutual solubility approach, where NaCl is treated as a separate component and, hence, a separate solid phase, because of the formation dry-out and precipitation of NaCl near the injection point. The non-iterative solution for the phase partitioning, including three different components – CO₂, H₂O, and NaCl, was proposed by Spycher and Pruess (2003). The basic equilibrium between water and CO₂ (without salt effect) is expressed by two reactions:



The equilibrium constant K is expressed by the fugacity (ϕ) for gaseous H₂O and CO₂, and activities (γ') for aqueous CO₂ and liquid H₂O. The values of constant K are strongly related to the temperature and pressure.

The mutual solubilities of the water mole fraction in the CO₂-rich phase (y_{H_2O}) and the CO₂ mole fraction in the aqueous phase (x_{CO_2}), with additional effect from the dissolved salts, which is expressed by the activity coefficients, are represented below (20),(21):

$$20) y_{H_2O} = \frac{K_{H_2O}^0 a_{H_2O}}{\phi_{H_2O} P_{tot}} \exp\left(\frac{(P-P^0)V_{H_2O}^-}{RT}\right)$$

$$21) X_{CO_2} = \frac{\phi_{CO_2}(1-y_{H_2O})P_{tot}}{55.508\gamma'_x K_{CO_2(g)}^0} \exp\left(-\frac{(P-P^0)V_{CO_2}^-}{RT}\right)$$

Where K^0 is the thermodynamic equilibrium constant for each component at temperature T and reference pressure P^0 (1 bar). P denotes the total pressure, V^- is the average partial molar volume of each pure condensed phase over the pressure range $P^0 - P$; ϕ describes the fugacity coefficient of each component in the CO₂-rich phase, and R is the gas constant. The effect of the brine salinity is included in the activity coefficient of water a_{H_2O} , and γ'_x denotes the activity coefficient for aqueous CO₂. According to Spycher and Pruess (2005), the best result is achieved with the activity coefficient provided by the Duan and Sun (2003) study, because it was fitted over a wider Pressure/Temperature range.

The above equations are solved, by rearranging and expressing them as A and B, resulting in:

$$22) A = \frac{K_{H_2O}^0}{\phi_{H_2O} P_{tot}} \exp\left(\frac{(P-P^0)V_{H_2O}^-}{RT}\right)$$

$$23) B = \frac{\phi_{CO_2} P_{tot}}{55.508\gamma'_x K_{CO_2(g)}^0} \exp\left(-\frac{(P-P^0)V_{CO_2}^-}{RT}\right)$$

Rewriting Eq. (20) in the form, where the water activity is approximated as water mole fraction, getting:

$$24) y_{H_2O} = A (1 - X_{CO_2} - X_{salt})$$

The mutual solubilities are represented by Eq. (25),(26):

$$25) y_{H_2O} = \frac{(1-B-X_{salt})}{(1/A-B)}$$

$$26) X_{CO_2} = B (1 - y_{H_2O})$$

X_{salt} expresses the mole fraction of the dissolved salt with additional dissolved CO₂. It can be governed by the equation below (27):

$$27) X_{salt} = \frac{\nu m_{salt}}{55.508 + \nu m_{salt} + m_{CO_2(aq)}}$$

Where: m stands for molality, ν refers to the stoichiometric number of ions represented in the dissolved salt (in the case of NaCl - 2). The formula for the CO₂ molality is provided below (28):

$$28) m_{CO_2} = \frac{x_{CO_2}(vm_{salt}+55.508)}{(1-x_{CO_2})} \text{ or } m_{CO_2} = \frac{x_{CO_2}55.508}{x_{H_2O}}$$

The application of the salt molality provides more benefits than mole fraction as input property, due to its independency of m to the CO_2 solubility. The derivation can be observed in Spycher and Pruess's (2005) paper. The final equation of the water mole fraction in the gas phase (y_{H_2O}) after some rearrangements, yields (29):

$$29) y_{H_2O} = \frac{(1-B)55.508}{\left(\frac{1}{A-B}\right)(55.508+vm_{salt})+vm_{salt}B}$$

Finally, after obtaining the fugacities coefficients from Spycher and Pruess(2005), Eq. (26) and (29), can be solved non-iteratively, providing the desired mutual solubilities of CO_2 and $H_2O+NaCl$ (salt can be presented as a separate component). However, an important remark should be made, this approach provides the assumption of an instantaneous local equilibrium in the description of phase partitioning between CO_2 and brine. This behavior can be seen in Figure 11. Assuming the CO_2 is maintained under the super-critical conditions ($T \sim 31.1 \text{ }^\circ\text{C}$; $P \sim 73 \text{ Bar}$), reading from Figure 11, the mass fraction of dissolved CO_2 in the brine phase is already around 5%, which does not reflect the real picture, it was suggested that CO_2 did not become saturated with water instantaneously, leading to the mass transfer along the whole length of the core (S.M.Roels, H.Ott, 2014). However, the local equilibrium assumption is beneficial when the mass transfer time scale is faster than the advection time scale (Niessner and Hassanizadeh, 2009); in this case, the reaction kinetics becomes infinite and phase partitioning occurs instantaneously.

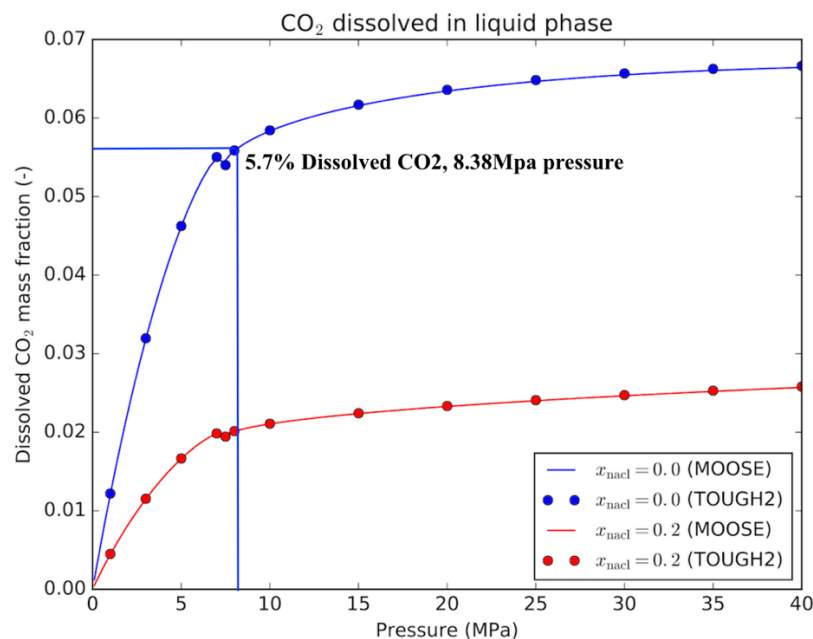


Figure 11 Dissolved CO_2 mass fraction in brine - comparison between MOOSE and TOUGH2 (C. Green., et al, 2018).

2.3.1 Plume migration-associated parameters

Besides the mentioned fluid flow equations and parameters for the numerical model's calculation, in these simulators' propagation of the injected CO₂ phase and further interaction between the reservoir brine (wetting phase), CO₂ (nonwetting phase), and porous medium expressed by the constitutive relations between relative permeability (k_r), fluid saturation (S), and capillary pressure (P_c) (M. Oostrom., *et al*, 2015). Relative permeabilities and capillary pressure have a significant effect on the channelling or viscous instabilities of the displacement process, providing the characterization of the local pore space occupation (displacement efficiency) and the macroscopic bypassing (sweep efficiency) (Garcia et al., 2003).

The consequence of both mechanisms is bypassing on a macroscopic scale. However, the reasons behind them are different, for example, channelling occurs due to variation of the rock properties: porosity and permeability. For the successful performance of the numerical simulator the spatial variation of the rock properties must be known beforehand – from the laboratory experiments or the existing literature examples, then the saturation distribution can in principle be correctly described. Nevertheless, the second cause of instability - viscous fingering, is caused by hydrodynamic perturbations and is independent of the porous medium properties, so can arise even in the homogeneous case. Ott et al. (2012) have assumed that channeling and viscous instability are likely to have a combined effect and enhance each other, leading to the reduction of the available pore space for CO₂ storage and unpredictable plume migration. Therefore, it is a critical task for the numerical simulation to predict and test under what conditions a displacement gets unstable. The storage in saline aquifers results in the larger mobility of the injected CO₂, rather than the displaced brine, leading to a significant increase in instabilities occurrence.

The stability of the propagation front can be expressed through the mobility ratio, which means the ratio of the mobilities of displacing (CO₂) and displaced (brine) phase (Eq. 30). The first input parameter in numerical simulators to affect the mobility ratio is relative permeability data.

$$30) M = \frac{k_{r,nw}/\mu_{nw}}{k_{r,w}/\mu_w}$$

Where, k_r represents the relative permeability of the wetting and non-wetting phases, μ denotes the viscosity of these phases. It was proposed that the best explanation can be obtained by the shock front relative permeability concept (Figure 12).

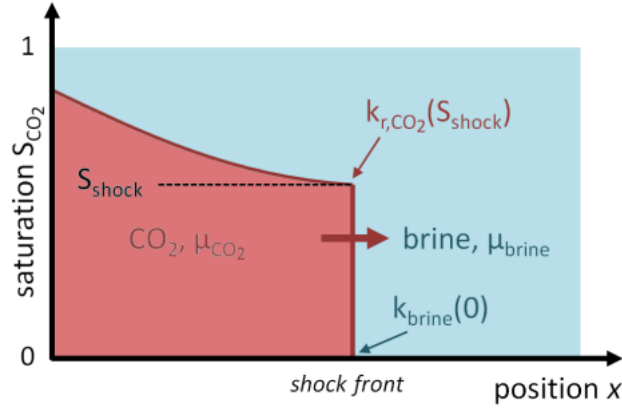


Figure 12 Immiscible displacement of brine by CO₂ (Berg and Ott, 2012).

The suggestion of the shock front relative permeability for the CO₂/Brine is expressed by the following mobility Eq. (31), where the main difference is reflected by the end-point relative permeability term:

$$31) M_S = \frac{k_{r,co2}(S_{shock})/\mu_{co2}}{k_{r,brine}(S_w=1)/\mu_{brine}}$$

There are three different models to express the relative permeability in numerical simulation. Most S – Pc – Kr relations reported in the subsurface scCO₂ literature use the empirical model proposed by Corey (1954), Brooks and Corey (1966) and van Genuchten (1980). The most widely used is the Brooks-Corey's (1966) simple polynomial functions. In modeling tools, the calculation of the relative permeability change is performed through the concept of effective saturation (Eq. 32):

$$32) S_{eff}^{\beta}(S^{\beta}) = \frac{S^{\beta} - S_{res}^{\beta}}{1 - \sum_{\beta'} S_{res}^{\beta'}}$$

Where, S_{eff}^{β} is the effective saturation for phase β ; S^{β} is the saturation for phase β and S_{res}^{β} is the residual saturation for phase β . The term $\sum_{\beta'} S_{res}^{\beta'}$ denotes the sum of the residual saturations of both phases.

The first model (33) is the relative permeability of the phase is given by Corey (1954). It can be considered the simplest because it does not provide any interconnection to the porous medium properties:

$$33) K_r = kr(S_{end-point}) * S_{eff}^n, \text{ where } n \text{ is a Corey exponent}$$

The study of Ott et al. (2012) has shown the clear effect of the relative permeability and Corey exponents on the front stability can be seen. There is a transition between stable to unstable displacement if the Corey exponent for the displacing fluid is higher or equal to the displaced fluid.

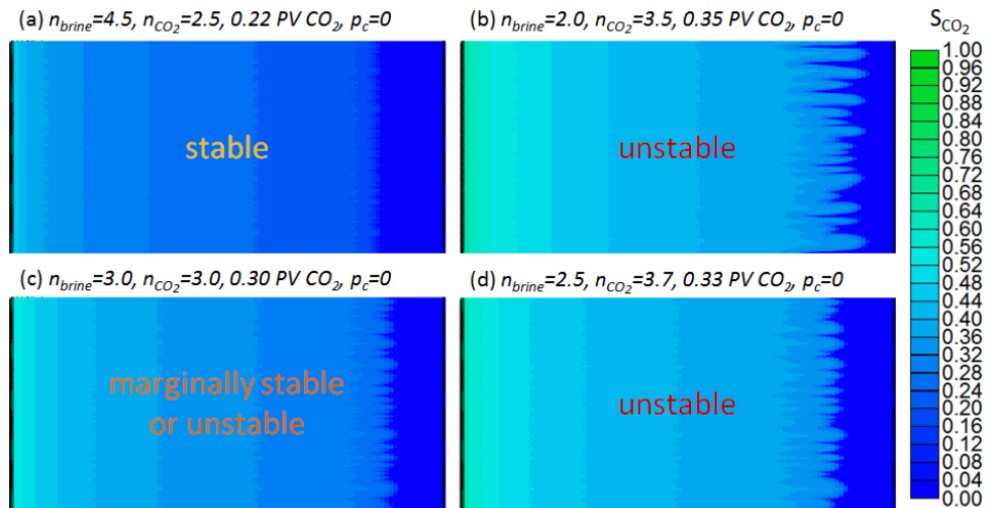


Figure 13 Flood displacement simulation model with 0 P_c and different Corey exponents (Berg and Ott, 2012).

The same simulation was performed to investigate the effect of the capillary pressure, by testing different interfacial tension values. Capillary forces provide a stabilization effect on the viscous fingering, but only along the short scale. There is Young's Laplace Eq. (34) (Bear, 1972), to provide an understanding of the relationship between capillary pressure and interfacial tension. Higher IFT leads to higher P_c . However, obtaining IFT and contact angle values in real porous rocks is challenging, so empirical and semi-empirical formulations for predicting the capillary pressure have been proposed. The Brooks-Corey (Brooks and Corey, 1966) and the van Genuchten (van Genuchten, 1980) capillary-pressure relationship relate capillary pressure to effective saturation. These models will be discussed further.

$$34) P_c = \frac{2\sigma_{F1F2}\cos\theta}{R}, \text{ where } \sigma_{F1F2} \text{ is IFT between phases, } \theta \text{ is the contact angle of the wetting phase on the surface of the porous medium and } R \text{ - radius of curvature}$$

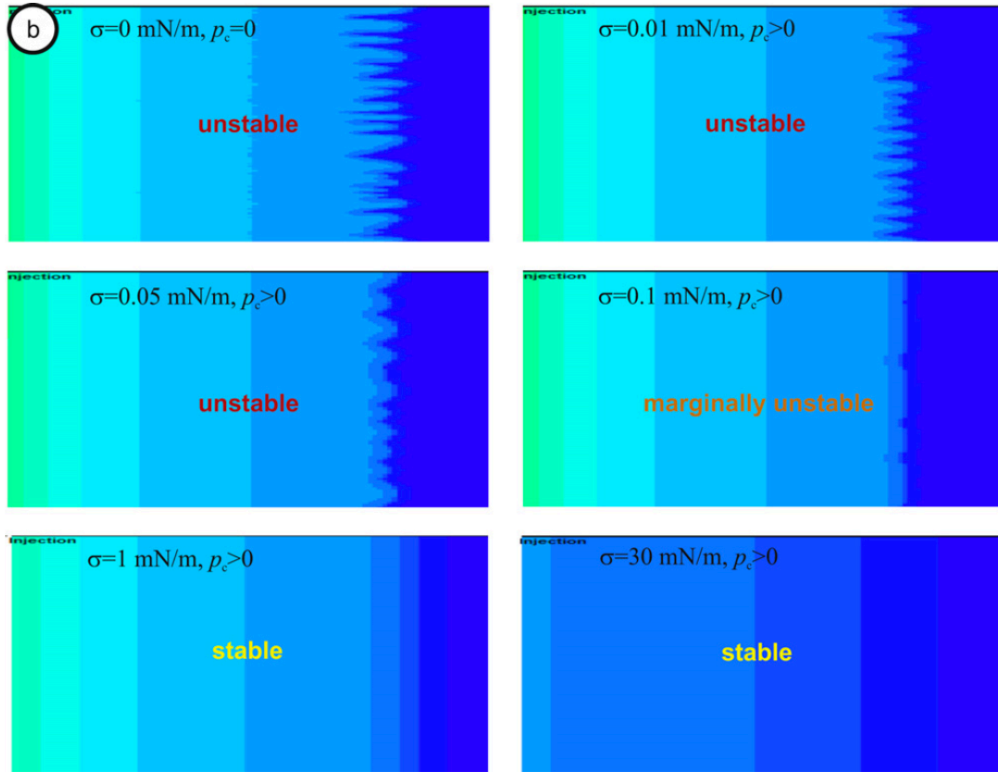


Figure 14 Transition from unstable to stable displacement with increasing IFTs – P_c (Corey exponents were the same) (Berg and Ott, 2012).

The most widely used $kr - S - P_c$ model was proposed by Brooks and Corey (1966). It can be considered as an extension of the previous Corey (1954) formulation and assumes that the pore space is represented in a form of a bundle of capillary tubes, where P_c and kr are coupled through the pore-geometry parameter (Dury et al., 1999). This model has received recognition in benchmarking simulations (Class et al., 2009; Ebigbo et al., 2007; Kolditz et al., 2012), and was proposed to use for the analysis of coupled wellbore-reservoir flow during the injection. The wetting phase is given by Equation (35) and non-wetting by Eq. (36):

$$35) k_{r,w} = (S_{eff})^{(2+\frac{3\lambda}{\lambda})}$$

Where λ is the Brooks–Corey pore geometry factor (statistical distribution of pore sizes in the porous medium).

$$36) k_{r,nw} = (1 - S_{eff})^2 (1 - (S_{eff})^{(2+\lambda)/\lambda})$$

The capillary pressure using the Brooks-Corey relationship is expressed (37):

$$37) P_c = P_e S_{eff}^{-1/\lambda}, P_e \text{ is the threshold entry pressure}$$

The Van Genuchten (1980) relative permeability and capillary pressure model is used as the default for the TOUGH2 simulator. It is another example of coupled $kr - S - P_c$ model, where

the same pore-geometry parameter m is used in both the $S - Pc$ and $k_r - S$ relations. Term m denotes the van Genuchten shape parameter, which describes pore-geometry. Another parameter that is related to $S - Pc$ is α (Pa^{-1}), which can be roughly described by the inverse of the gas entry pressure (M. Oostrom, et al., 2015).

The Van Genuchten relative permeability model is provided below for the wetting phase Eq.(38) and non-wetting (39):

$$38) k_r = \sqrt{S_{eff} \left(1 - \left(1 - S_{eff}^{\frac{1}{m}}\right)^m\right)^2}$$

$$39) k_{r,nw} = \sqrt{S_{eff} \left(1 - \left(1 - S_{eff}^{\frac{1}{m}}\right)^{2m}\right)}$$

The numerical problem may arise because the derivative of $S_{eff} \rightarrow 1$ tends to infinity. It means, when the S_{eff} oscillates around 1, the simulation does not converge well.

The capillary pressure is expressed by Eq. (40):

$$40) Pc = \begin{cases} 0 \\ \frac{1}{\alpha} (S_{eff}^{-1/m} - 1)^{1-m} \end{cases}, \quad \text{if } S_{eff} \geq 1 \text{ then } Pc = 0; \text{ the parameter } m \text{ must} \\ \text{satisfy } 0 < m < 1$$

The comparison of the both Brooks-Corey and Van Genuchten models was provided by (M. Oostrom, et al., 2015), using the STOMP-CO2 simulator, using the Berea sandstone as a core sample. The 2-D simulation results are provided below to evaluate the effects of buoyancy, relative permeability, and capillary pressure on the plume development. As can be seen in Figure 15, there is no evident displacement instability can be observed, mainly due to the capillary pressure stabilizing effect. The Van Genuchten model has provided a larger extent of the migrated plume. In addition, there is obvious gravity overrun, because of buoyancy effects associated with a less dense CO_2 phase than the brine phase.

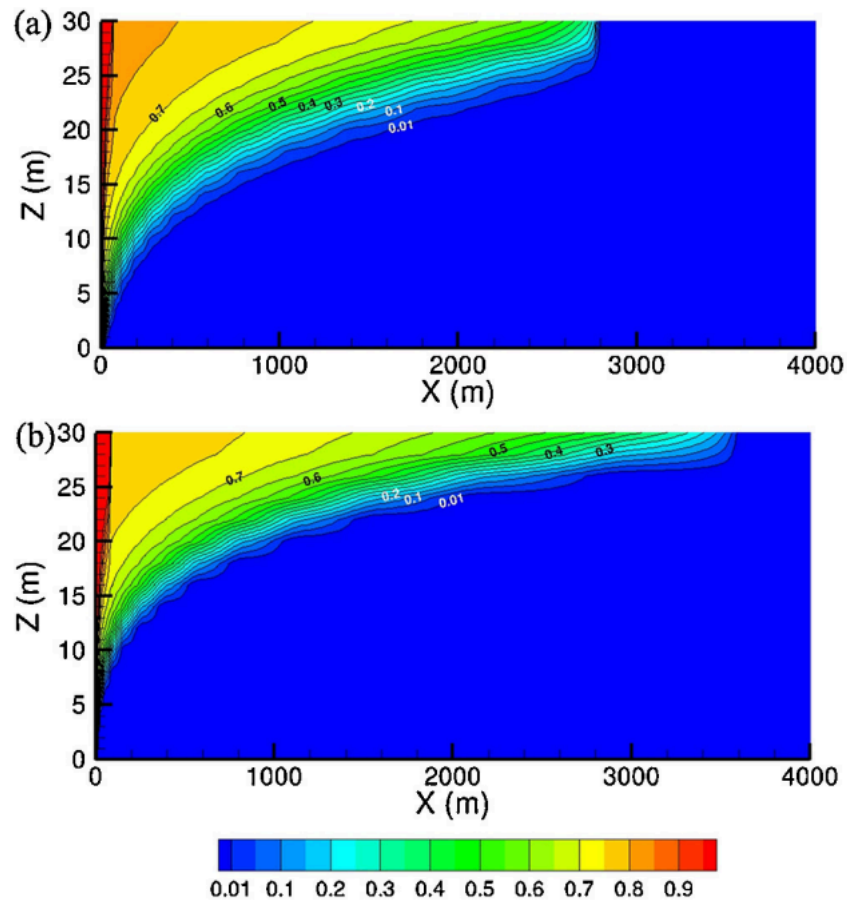


Figure 15 Gas saturation after 30 years of injection into Berea sandstone using the (a) Brooks-Corey, (b) van Genuchten relative permeability and capillary pressure models (M. Oostrom, et al., 2015).

The final remark regarding the work of numerical simulators should be made. The principle behind the simulation is required to solve the system of equations with two-phase pressures and the two-phase saturations as primary unknowns. The additional complication is caused by the dependency of the system on relative permeability (k_r , D) and capillary pressure (P_c), and its effect on saturation, leading to a non-linear system of equations. To solve these non-linearities, a nonlinear solver is required, the common example is Newton's non-linear solver, with the Implicit Pressure – Explicit Saturation (IMPES) approach. Then, the proposed domain is discretized and the system is solved via finite differences or finite elements approach (K.W. Bandilla et al., 2014).

2.4 Physics behind the salt precipitation mechanisms in saline aquifers during CO₂ injection

Many studies have confirmed that the injected super-critical CO₂ displaces the formation brine in the form of two-phase displacement away from the injection point. The trapped/residual brine is left behind the displacement front and remains as thin films on porous media grains, in addition to the confirmed fact that water and CO₂ are mutually soluble, either in a gaseous or supercritical state (Roels et al., 2014). The residual saline water gradually vaporizes into the dry-CO₂ swept zone, leading to an increase in ion concentration and super-saturation of the brine, denoting complete formation dry-out and precipitation of salt in the porous medium when the salinity concentration in brine reaches its solubility limit. This behavior is mostly inherent in the near-injection area (Ott et al., 2010; Pruess & Mueller, 2009; Y. Wang et al., 2010; Kim et al., 2012; Oh et al., 2013). However, opinions differ regarding the salt precipitation pattern and the most influential mechanisms enhancing this process. Some studies have pretended that the salt accumulates locally near the injection point (Ott et al., 2010; Kim et al., 2012; Oh et al., 2013). This precipitation pattern is inherent to the capillary-driven back flow of saline water into the dried-out zone (Pruess & Mueller, 2009; Miri et al., 2015). Therefore, three distinct zones have been identified (Figure 16), where a moving drying front is formed behind the CO₂ displacement of the resident brine (Ghafoori et al., 2017; Nooraiepour et al., 2018). On the contrary, it was observed that dry-out might take place along the entire core length with homogeneous salt precipitation, or even non-local precipitation. This behavior has been reported during the propagation of CO₂ in the saline aquifer with the assumption that reaction kinetics is slower compared to advection rates (Roels et al., 2014; Jones & Detwiler, 2019). While there is no consensus regarding the salt precipitation distribution either local or non-local and its effect on the reservoir permeability, the indisputable dependency was noted on the drying regime and its strong relation to the CO₂ injection rate (Kim et al., 2012; Ott et al., 2013; Miri, 2016). The magnitude of the injection rate breaks the equilibrium between evaporative and capillary fluxes, by changing the pattern of the fluid flow and solute transport behavior and affecting the distribution of the mineralization (Detwiler & Rajaram, 2007).

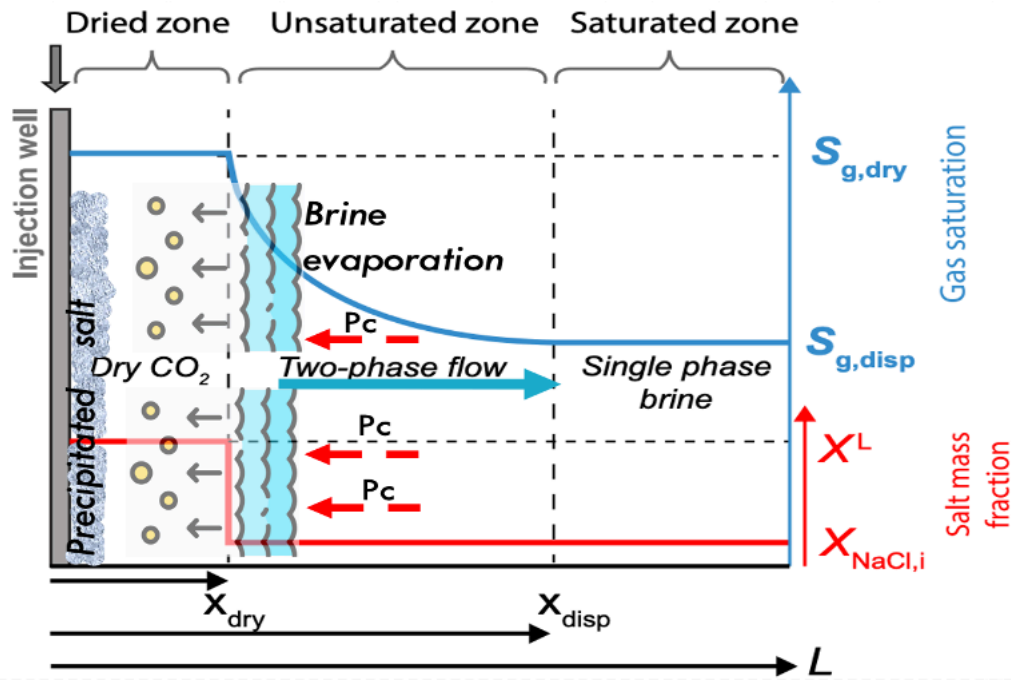


Figure 16 Conceptual propagation front separation into three zones, due to dry-out. L – length of the front from the injected well; X_{disp} and X_{dry} are the length of the displacement and the dry-out fronts, respectively; $S_{g,dry}$ and $S_{g,disp}$ are the saturations of CO_2 at the dry-out zone and displacement front, respectively; X^L – the solubility limit salt mass fraction in brine, and $X_{NaCl,i}$ – the initial salt mass fraction (G.Lima et al., 2020).

2.4.1 Mechanisms and physics of salt precipitation in saline aquifers during CO_2 injection

It is vital to utilize all available tools for testing and mimicking the salt precipitation mechanism. The evaluation can be performed through numerical simulations, core flooding experiments, and micro-fluidics applying different parameters, time, and length scales. Miri and Hellevang (2016) in their study have summarized all available physical mechanisms which lead to and enhance the drying-out process, hence, evaporation of the residual brine and salt precipitation. The mechanisms are listed below and conceptually represented in Figure 17:

- 1) Evaporation of the residual brine into the dry- CO_2 front, after the two-phase displacement of injected sc CO_2 and formation brine;
- 2) Capillary-driven back flow is formed due to the water saturation gradient away from the injection point, bringing the brine back towards the CO_2 dry-out region through interconnected water films.
- 3) Molecular diffusion of salt into the brine aqueous phase, in addition to a self-enhancing process since the salt crystals, is formed;
- 4) Gravity bypass of unswept brine due to buoyancy (gravity “tongue” of CO_2 is formed, leaving the brine underneath the sweeping front);

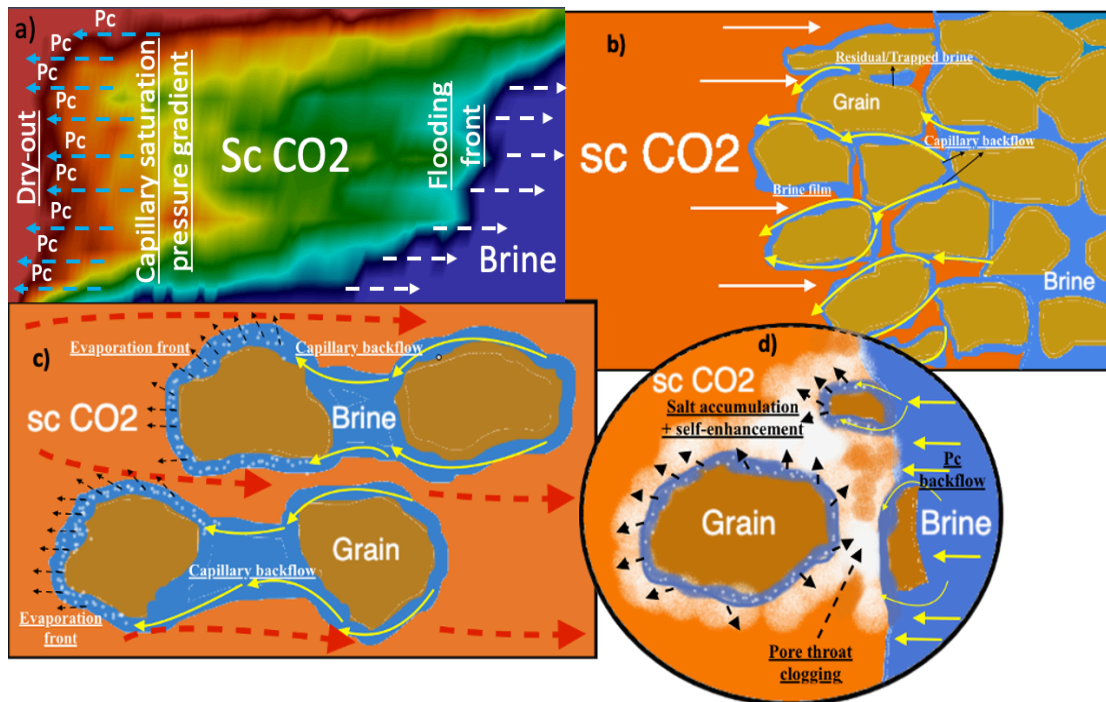


Figure 17 a) Two-phase displacement of Brine by CO₂, formation of the gravity overrun due to buoyancy and capillary pressure back flow due to saturation differences between the swept zone with residual saturation and the zone where displacement has not happened yet. b) Increase of capillary pressure, increase of the back flow, and formation of the bypassed brine in the form of residual saturation and brine film around the grains c) Capillarity of salt drives more brine on films around the grains, initiating the evaporation process into the dry-out zone. d) Precipitation of salt and further self-enhancement leading to clogging of CO₂ pathways, which eventually can lead to complete clogging of the pore throats.

The injection of scCO₂ into the saline aquifer initiates the two-phase displacement mechanism, where primary drainage dominates due to the viscous forces, pushing the formation brine away from the injection side. The movement velocity of this front is strongly related to the injection magnitude, leading to the correlation of the governing underground mechanisms to the injection characteristics. Further propagation of the displacement front leaves the residual brine trapped in the form of thin wetting films covering the grains or liquid bridges between the grains (Miri et al., 2015). The swept region is immediately subjected to the constant flow of the low vapor pressure dry-CO₂, which signifies the initialization of the evaporation mechanism. The described above formulation of the mutual solubilities by (Spycher and Pruess, 2005; Spycher and Pruess, 2010) has shown that water is less soluble in the CO₂ phase contrary to CO₂ in the water phase by itself. Nevertheless, the existence of constant flow would signify the

evaporation of a large portion of brine leading to the development of the dry-out front and then complete dry-out of the formation. The hysteresis effect should not be neglected, because water evaporation affects the relative permeability curves alteration and enhances evaporation. The speed of the dry-out front propagation is significantly slower than the velocity of the displacement front. However, both these fronts contribute to the movement of the water from the near-wellbore area, but time-wisely act differently. In addition, the mechanisms behind displacement and dry-out fronts are different. There is almost no evaporation within the displacement front, while there is no convective flow during dry-out (Ott et al., 2014; Peysson et al., 2014). An additional saturation gradient is created within the dry-out zone due to significant water mass exchange in this area (Peysson et al., 2014). This saturation gradient overpowers the gradient from the pure viscous displacement providing an extra capillary gradient, which is more powerful than the injection pressure gradient. As a result, this additional capillary pressure moves the water back toward the evaporation front, enhancing the evaporation process and precipitation (Pruess and Müller, 2009; Ott et al., 2015). Continuous vaporization increases the mass fraction of salt in the trapped brine activating the salt diffusion mechanism in opposite direction to the drying front (Pruess, 2009; Shahidzadeh-Bonn et al., 2008). The solute diffusion and capillary back flow lead to the brine oversaturation by the salt mass fraction (magnitude tends to fluctuate between 26-27% by mass) signifying the salt precipitation out of the solution. The hydrophilic nature of the precipitated salt provides a self-enhancing feature by imbibing the water from considerable distances to the evaporation front, meaning more precipitation (Miri et al., 2015). Moreover, salinization gives additional stability to the water films around the grains and further enhances the mineralization mechanism (Pruess and Müller, 2009).

2.4.2 Macroscopic salt distribution

Miri and Hellevang (2016) have distinguished three drying regimes - diffusive, capillary, and evaporative. The main attribute which characterizes the specific regime is the relation between evaporation stabilization and capillary fluxes. The identification of the regime is important because it is related to the precipitation pattern, which can be represented in two different forms (local and non-local). According to Miri et al. (2015), local salt precipitation is described as a development of massive salt accumulation where the drying front is stabilized.

The diffusive regime occurs when the capillary back flow fluxes dominate over the evaporation front. This regime is inherent with low injection rates and low evaporation because capillary forces overpower the drying front and bring the brine back towards the injection point. However, this minor vaporization near the injection zone increases the salt supersaturation and enhances salt diffusion, providing homogeneous distribution of salt throughout the porous medium (Peysson et al., 2014).

The capillary regime (Figure 18) happens when the evaporation rate prevails over the capillary back flow at the beginning. However, further propagation of the drying front leads to an increase in water vapor pressure and, hence, a decrease in the evaporation rate and gradual prevalence of the capillary back flow. At some point, these forces equilibrate, and a steady state is reached, stabilizing the precipitation front (Miri and Hellevang, 2016; Ott et al., 2013). However, this equilibration is constantly destabilized due to the powerful capillary suction of formed salt, inducing the additional outflow of the brine to the precipitated area and massive salt accumulation. Nevertheless, it does not suppress the evaporation front from further migration into the porous medium (Ott et al., 2013; Miri et al., 2015).

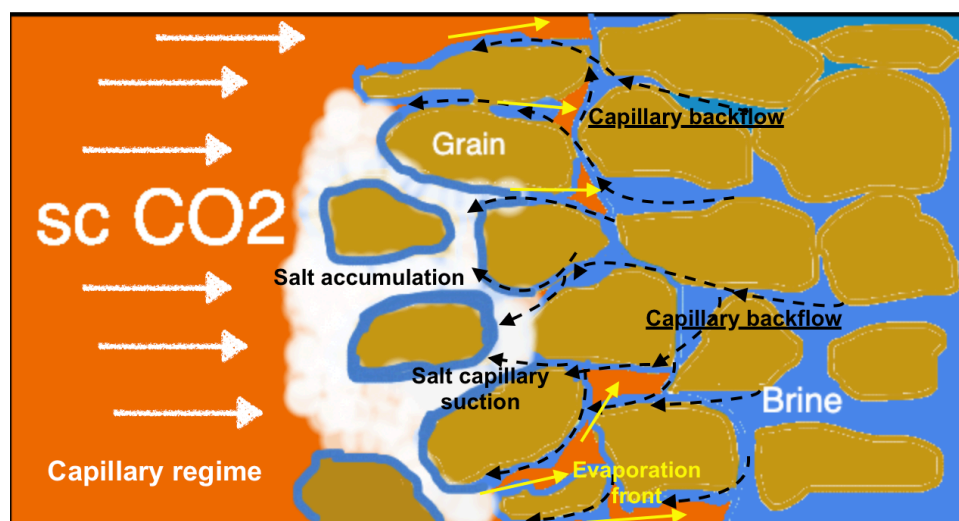


Figure 18 Capillary regime signifies massive salt accumulation due to salt capillary suction.

The evaporative regime (Figure 19) is associated with a critical or above-critical injection rate (Kim et al., 2012; Andre et al., 2014). The high injection rate leads to a greater evaporation front than capillary back flow fluxes. It was noted that this regime contributes to the formation of the advancing drying front, which instantaneously evaporates the residual brine along the migration path into the dry-CO₂ phase. It is generally accepted that salt distributes homogeneously in this region.

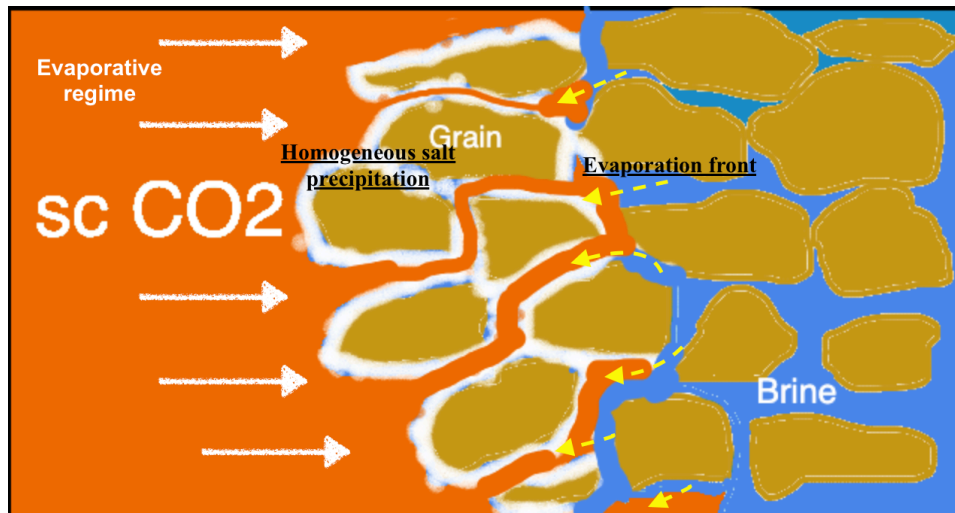


Figure 19 Evaporative regime provides the homogeneous salt distribution along the migration path of the brine around the grains.

Nevertheless, the identification of the existing regime is a challenging task, and the salt distribution pattern is still not easily predicted either. The uncertainties are induced not only by drying regimes but also by the thermodynamic conditions and some properties of the medium, such as the distribution of the pore throats in the porous medium or macro/microporosity (Andre et al., 2014; Ott et al., 2015).

2.4.3 Sensitivity studies on precipitation using a numerical approach

The description of the physical mechanisms related to the salt precipitation has revealed the complexity of this process and proved its dependency on the following parameters: CO₂ injection rate, capillary pressure, thermodynamic conditions (temperature, salinity, mutual solubilities formulation) and formation properties, which would affect CO₂ propagation (porosity, absolute and relative permeability). It has not been mentioned earlier, but formation heterogeneities are also crucial in predicting CO₂ plume migration, hence, dry-out front propagation and salt distribution. CO₂ flows into the more permeable zones creating instabilities and channeling.

To start the review of the sensitivity analysis, the critical observation and comparison between local equilibrium and reaction kinetics approach for mutual solubility modeling should be made. A significant discrepancy in the salt distribution was noted. The physics behind the application of the local equilibrium assumption (Spycher and Pruess, 2005) is provided in detail in Chapter 2.3. However, Roels et al. (2014) have identified a mismatch between numerical and experimental results. It was suggested that the majority of the numerical simulators (e.g. TOUGH2) reveal heterogeneous salt distribution, mainly around the injection point. Nevertheless, it was described before that a diffusive drying regime in analytical cases predicts a homogeneous distribution of precipitants. It was assumed that this incompatibility is subjected to the improper implementation of a local equilibrium phase partitioning. Phase partitioning is the mechanism that is related to Gibbs's free energy. This energy is a consequence of the destabilization of equilibrium caused by CO₂ injection, mainly spatial variations of pressures due to viscous pressure drop, capillary pressure, and concentration change (Sandler, 2006). The system attempts to bring the equilibrium back by releasing the Gibbs free energy in the direction of decreasing chemical potential, creating mass transfer (phase partitioning) along the length of the investigation (Roels et al., 2014). As a result, Pinder and Celia (2006) have proposed the following equation to describe the mass transfer between phases (Eq. 41):

$$41) Q_{\alpha \rightarrow \beta}^i = k_{\alpha \rightarrow \beta}^i (\omega_{\beta}^{i,max} - \omega_{\beta}^i)$$

Where, $Q_{\alpha \rightarrow \beta}^i$ denotes the mass transfer rate of component i from phase α to β , $k_{\alpha \rightarrow \beta}^i$ is mass transfer rate constant (relates the model results to the experimental data) and the term $(\omega_{\beta}^{i,max} - \omega_{\beta}^i)$ describes the difference between the solubility limit and the actual concentration (mass fraction).

The kinetic rate model has revealed the completed dry-out of the domain, it should be mentioned that the size of the investigated domain was relatively small (1 cm in diameter and

3 cm in length). The solid precipitation profile was generally flat due to the uniform mass transfer between phases along the whole length. It is explained by the low saturation gradient and neglectable capillary back flow, resulting in an insignificant impact on the precipitation process (Figure 20).

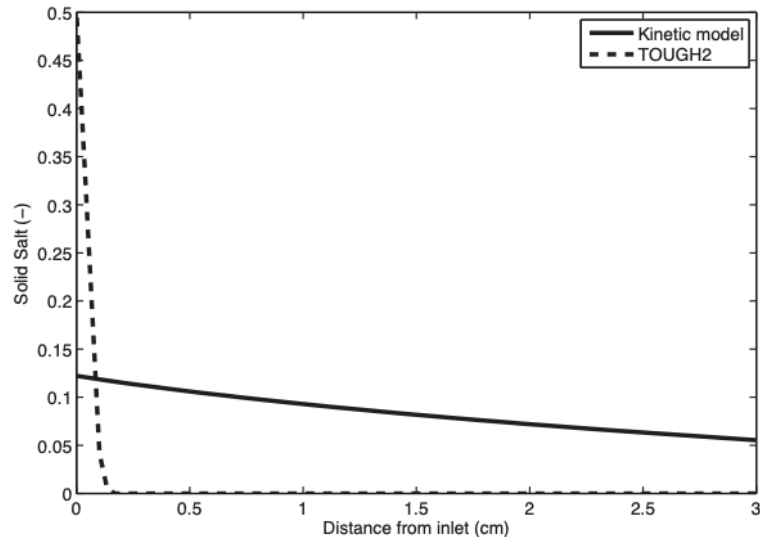


Figure 20 Comparison of solid saturations using kinetic and local equilibrium (TOUGH2) mutual solubilities models (Roels et al., 2014).

1. Injection rate

Pruess and Müller (2009) have tested the influence of different parameters on the magnitude of salt precipitation using general-purpose reservoir simulation code TOUGH2 (Pruess, 2004) in conjunction with a fluid property module “ECO2N”. It has already been mentioned that this simulator is associated with a mutual solubility model assuming a local equilibrium approach (Chapter 2.3) (Spycher and Pruess, 2005). It was concluded that a reduction in injection rate with the assistance of capillary pressure and gravity overrun (which becomes stronger with low rates), would signify higher solid salt concentration. Gravity and capillary effects prevent the propagation of the CO₂ displacement front at the bottom of injected interval. The CO₂ is immobile within this area, producing an almost stationary dry-out front, due to additional capillary-driven back flow of water. It causes significant precipitation that enhances the gravity overrun. It should be noted that within the same research, the highest solid saturation was achieved after an increment in residual saturation. A higher amount of trapped brine signifies more opportunities for evaporation and precipitation.

Case	CO2 Rate (kg/s)	P cap	Solid saturation (%)
1	25	Yes	6.97
2	12.5	Yes	7.13
3	6.25	Yes	7.47

Table 1 Injection rates - sensitivity analysis (adapted from Pruess and Müller, 2009)

Kim et al. (2012) and Wang et al. (2017) have performed a sensitivity analysis using the same TOUGH2 tool with the “ECO2N” module. The same behavior was observed (Figure 21), where lower injection rates lead to higher local solid saturation near the injection point. As the rate increases, the drying front migrates deeper into the formation, showing a more uniform salt distribution.

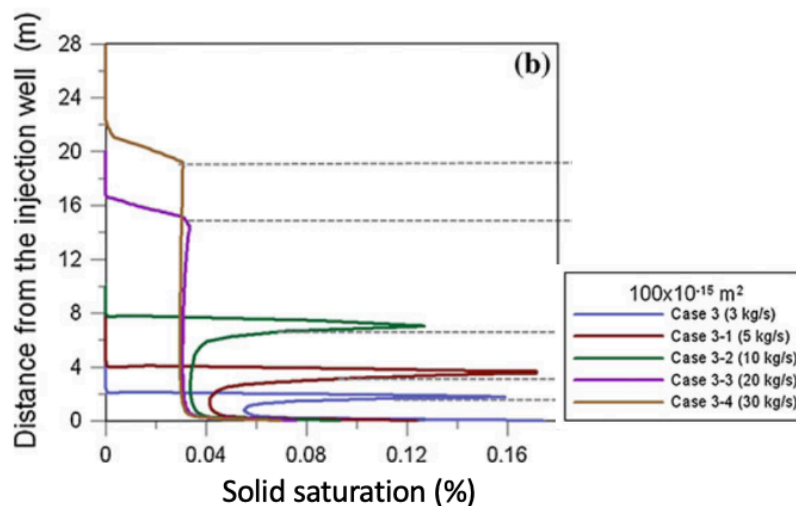


Figure 21 Sensitivity analysis of injection rates (adapted from Kim et al., 2012).

G. Lima et al. (2020) analyzed the impact of precipitation on fracture aperture reduction, testing different injection rates and effective normal stress. The Moose simulator (Permann et al., 2020) was used in this study. The injection rate was expressed in the form of a Peclet number. It was identified that the fracture volumes for low Pe (31.6) have shown a larger reduction in aperture size, hence, more precipitation than in higher Pe cases (100). In addition, the case with higher effective stress has indicated relatively more volume of salt precipitated.

The reaction kinetics approach was applied by H.Ott et al. (2015) to test the effect of the injection rate on the distance of propagation where evaporation takes place. H.Ott et al. (2015) have named it the distance of attraction (I_{evap}) with an explanation - the interval after which the saturation limit in CO₂ was reached. The linear dependency between the distance of attraction and the injection rates was found, however, after the minor instability near the injection point (Figure 22).

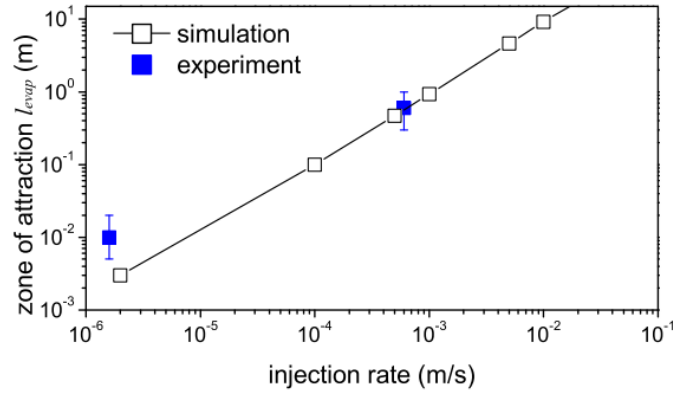


Figure 22 The zone of attraction as a function of injection rate (H.Ott et al.,2015).

Another attempt to test and compare the reaction kinetics and equilibrium approaches, in addition to different injection rates, was performed by S.Parvin et al. (2020). For this purpose, in-house MATLAB simulation software, MRST, (Bao et al., 2017; Lie et al., 2007) in conjunction with an electrolyte version of perturbed chain statistical associated fluid theory (ePC-SAFT) was utilized. The MRST tool has treated the salt as a separate solid phase in addition to gaseous and liquid phases, while ePC-SAFT was responsible for creating the fluid model which would account for the formation dry-out and subsequent halite precipitation. Interesting behavior was observed in comparing two-phase partitioning approaches. Identical results were obtained, especially for higher reaction rate constant ($\sim 10^3$). However, the magnitude of the solid saturation was slightly different, but the extent of the precipitation zone is similar (Figure 23a). Controversially, compare to the other studies, the work of S.Parvin et al. (2020) has identified the higher salt precipitation for the higher injection rates (Figure 23b). This behavior was explained as a higher injection flow rate signifies a higher vaporization rate leading to faster progress of the evaporation front. As a result, more salt is deposited with uniform precipitation throughout the dried zone.

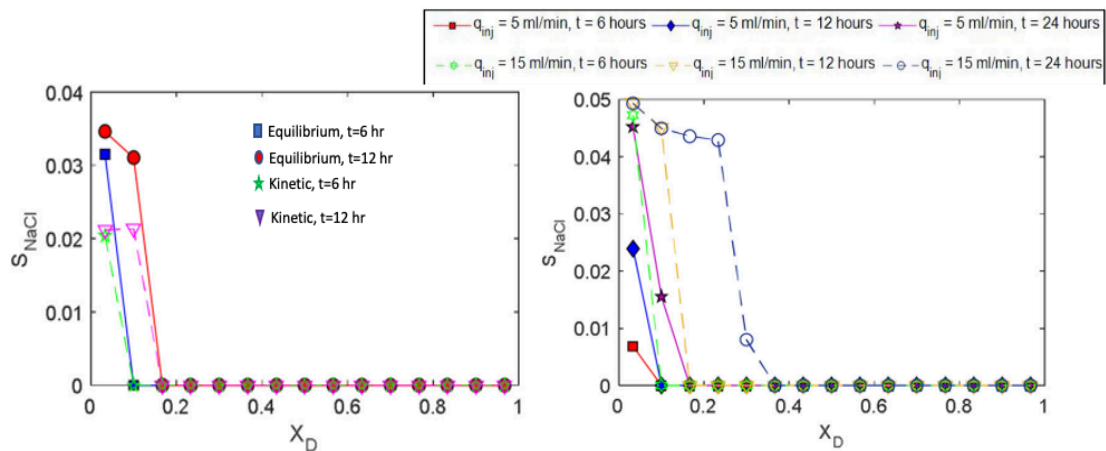


Figure 23 a) Comparison of kinetic and equilibrium models; b) Sensitivity analysis of injection rates (S.Parvin et al., 2020).

2. Capillary pressure

Hypothetically, capillary pressure promotes the activation of brine back flow towards the dry-out zone, enhancing the evaporation and intensity of precipitation (Miri et al., 2015). Some studies claim that it provides a negligible effect on salt precipitation. However, in conjunction with a low injection rate, the effect of capillary pressure can be significantly amplified. For example, the simulation results of Pruess and Müller et al. (2009) have identified minor changes in salt precipitation, where high rates in combination with capillary pressure were tested. On the other hand, during the low-rate injection with capillary pressure, the solid saturation increased from 6.71% to 7.47%. In the Pruess and Müller et al. (2009) sensitivity analysis, a combination of capillary pressure and low rates manifested the highest spike in salt precipitation. In the study of S.Parvin et al. (2020) three different capillary pressure magnitudes were tested – low, high, and custom low capillary pressure model with the salt self-enhancing mechanism. It was noted that the higher the capillary pressure the more salt precipitates behind the evaporation front, altering the precipitation pattern. However, the custom model with low P_c and self-enhancing mechanism has revealed similar to high P_c behavior. The analytical investigations of the P_c impact on the salt precipitation were performed by H.Kelly et al. (2018) and A. M. Norouzi et al. (2022). Both models have confirmed the significant impact of the capillary pressure on the magnitude of salt precipitation. H.Kelly et al. (2018) have used the concept of capillary number to express the impact of capillary pressure on the back flow of brine. It was summarized that the problem is largely controlled by a capillary number, the solid saturation of the precipitated salt around the injection well has linearly increased with decreasing capillary number. A. M. Norouzi et al. (2022) have proposed a novel approach to an analytical solution that considers the impact of capillary pressure. It is based on the fractional flow theory and the definition of shocks under the effect of capillary pressure. The study has confirmed that the propagation distance of the drying-out shock front is reduced under the governance of the capillary forces. As a result, capillary-driven back flow constantly brings the brine towards the dry-out region, enhancing the precipitation process and making it continuous versus time. Therefore, an increase of 14.71% in the average amount of precipitated salt was indicated, in addition to an increment of 58.73% at the near injection well zone (Figure 24).

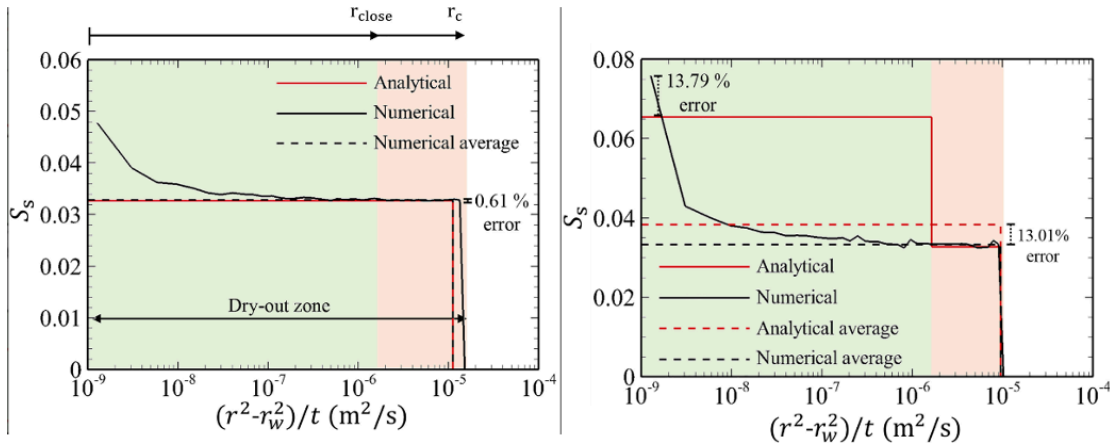


Figure 24 left) the case with no capillary pressure; right) the case with capillary effect (localized salt saturation) (A. M. Norouzi et al., 2022).

3. Temperature, salinity, and clogging models

The temperature increase leads to more gravity segregation between phases due to the lowering of the scCO₂ density. As a result, the migration plume of the CO₂ and, hence, the dry-out zone are extended. In addition, at elevated temperatures the solubility of water in the CO₂ increases, resulting in the rapid achievement of the saturation limit, therefore precipitation starts earlier (Kim et al., 2012; Miri and Hellevang, 2016; S.Parvin et al., 2020).

On the other hand, the increase in salinity induces a slight decrease in water solubility in the CO₂ phase and a reduction in the evaporation rate. However, a noteworthy drop in the dissolution of CO₂ in the brine is observed. The sensitivity analysis conducted by Kim et al. (2012) and S.Parvin et al. (2020) identified more salt precipitation due to the higher initial salinity of the resident brine.

The effect of clogging models is controversial. However, it is important to consider them due to their dependency on the formation impairment and the relationship between porosity and permeability changes (S. Parvin et al., 2020). These models help to translate the changes in pore structure from pore-scale to continuum-scale (upscaling) (Masoudi et al., 2021). The widely applied models for the description of porosity/permeability relations are the cubic Kozeny-Carman grain model (Carman, 1939), Verma and Pruess (V&P) (Verma & Pruess, 1988), and Power Law relations. However, these models are generally a great source of uncertainties because they are based on idealized models of the pore network and might not apply to more complex porous media (G.Limma et al., 2020). For example, V&P is often used for numerical simulators, like TOUGH2 (Pruess, 2004) and there were cases when the permeability was reduced to zero due to finite porosity that corresponded to a fraction of the original porosity (Roels et al., 2016).

Chapter 3

Multiphysics frameworks used in this study

The basic principle behind the work of numerical tools is provided in Chapter 2.3. In this chapter, each multiphysics framework that was used in this study is described in detail.

3.1 TOUGH2 - ECO2N

TOUGH2 is a non-isothermal multiphase fluid flow simulator used for solving and mimicking wide-range heat and mass transfer problems (Pruess, 2004). For better visualization and convenience of use, it was coupled with the graphical user interface (GUI) code PetraSim. This simulator has received its acknowledgement especially in assessing CO₂ geological storage. After implementing the customized EOS routine called ECO2N it has become a vital tool for many researchers for evaluating CO₂-water-salt systems extensively dedicated to the geological storage in saline aquifers (Pruess and Spycher, 2007). It was confirmed that TOUGH2 is capable of reproducing fluid properties within experimental error for the temperature, pressure, and salinity conditions of interest (Pruess, 2005; Pruess and Spycher, 2006). The main attraction of this simulator for this paper is related to the evaluation of salt precipitation mechanism, permeability reduction, and assessment of the factor influencing these processes. The description of the equations involved in the multicomponent non-isothermal multiphase flow in porous media is extensively provided in Chapter 2.3. However, some additional notes should be made. The combinations of the water-CO₂ system are depicted in Figure 25(a). It should be mentioned if the salt component (NaCl) ("salt") exists in the system, the number of combinations doubles (Pan et al., 2015). The presence of the additional solid phase is performed by comparison between the mass fraction of dissolved salt in brine and the solubility limit. If the solubility limit is exceeded, the solid phase is formed. To define the series of equations, four variables are required: pressure, CO₂ gas saturation in two-phase or mass fraction in single-phase conditions, salinity as solid saturation or mass fraction dissolved in brine, and temperature for the non-isothermal case. Then, to solve the residual form of this non-linear system of equations the Newton-Raphson iteration method is used (P. Audigane et al., 2011). As a reminder, TOUGH2/ECO2N uses a local equilibrium phase partitioning (Figure

25b) and the mass fraction of CO₂ in the brine phase and vice versa is calculated according to the solubility limits at certain conditions (temperature and pressure) (Spycher and Pruess, 2005).

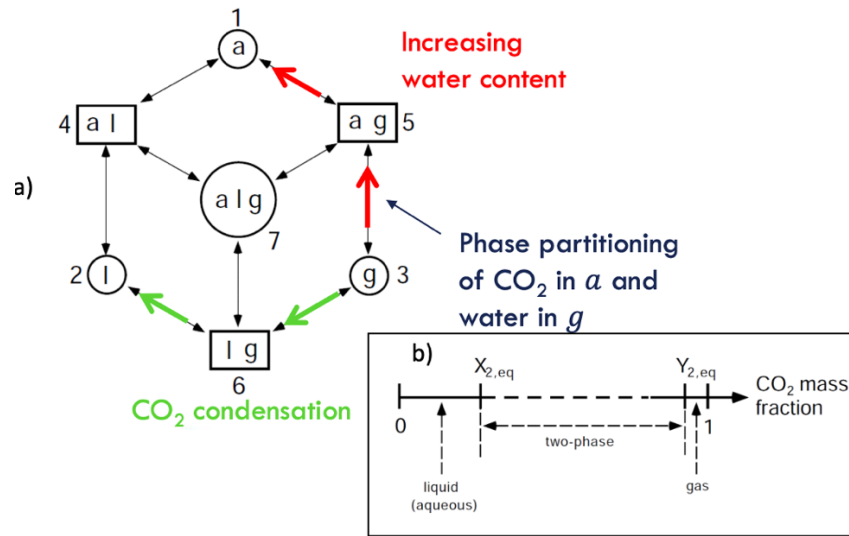


Figure 25 a) The possible combination of phases in the water-CO₂ system; b) The schematic representation of phase partitioning (Pan et al., 2015).

3.2 DuMux

DuMux was developed by the workgroup from Stuttgart University and is mostly used at the Department of Hydromechanics and Modelling of Hydrosystems (Koch, Gläser, et al., 2020). However, it is not a separate simulator tool but can be considered as a multiphysics framework module for simulating fluid flow implemented in the wider framework called DUNE which stands for Distributed Unified Numerics Environment (Koch, Gläser, et al., 2020). The fundamental input files of any simulation in DuMux are built in the form of C++ programming language aside from the main function of the code (Koch, Gläser, et al., 2020). The main additional values of using an open-framework simulator are the possibility to create and introduce user-defined prerequisites and flexibly solve particular problems, in comparison to fixed and unchangeable reservoir simulations, like ECLIPSE. For example, DuMux was acknowledged during numerical studies for the efficiency evaluation of CO₂ storage in the North German Basin and was used in simulation studies performed on the Ketzin pilot site in Brandenburg (Tatomir et al., 2019). Kempka et al., (2013). For the comparison of DuMux and the benchmark simulators TOUGH2 and ECLIPSE, Kempka et al., (2013) performed a numerical evaluation at the Ketzin pilot site into which CO₂ was injected (Figure 26). It was concluded that the results obtained were a good match, just with a slight overestimation of the gas phase for DuMux.

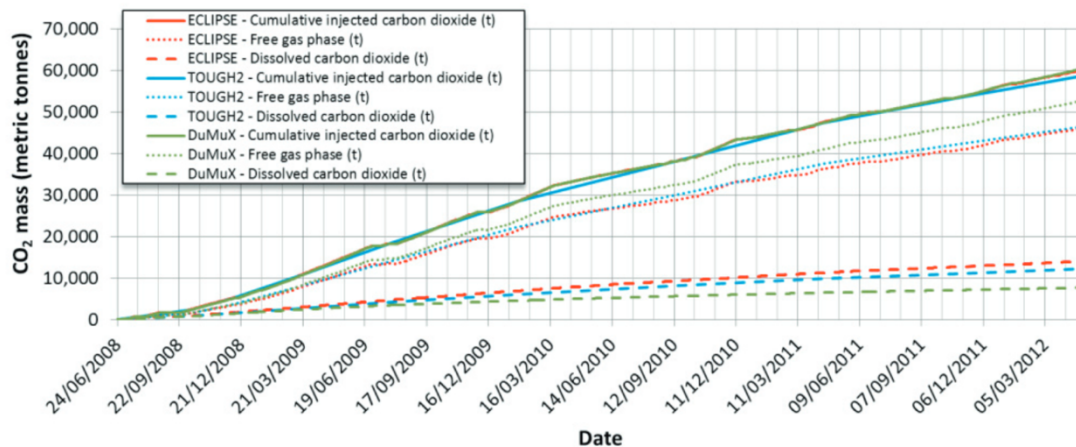


Figure 26 CO_2 mass evaluation with ECLIPSE, TOUGH2, and DuMux simulators (Kempka et al., 2013).

There are three main approaches for spatial discretization available in DuMux - the box method, cell-centered finite volume methods, and the staggered grid scheme (The DuMux Handbook, 2021). For this paper, the main target is the box method because it integrates the benefits of both the Finite Element and Finite Volume methods. The advantage of the FE method is the possibility to use unstructured grids, while the FV method is mass conservative (Flemisch & Class, 2019). For the solution strategy, the equations of multi-phase flow are expressed in the equation for pressure and equations for saturations of phase/component/... transport. The pressure equation is defined as the sum of the mass balance equations and thus results in the total flow of the fluid system. The most appropriate sequential model for the DuMux simulator is the fractional flow formulation for two-phase flow. For this scheme, the IMPlicit Pressure Explicit Saturation algorithm (IMPES) is commonly used (The DuMux Handbook, 2021). Then, a coupled system of nonlinear equations is solved simultaneously and iteratively. In DuMux, numeric differentiation is performed to calculate the Jacobian matrix. For this purpose, the following equation adapted from (Flemisch & Class, 2019) is solved iteratively (Equation 42), where the term L_{k+1} denotes the new iteration, $k + 1$ refers to the current Newton iteration and k is the previous Newton iteration.

$$42) J(L_k)(L_{k+1}-L_k) = -R(L_k)$$

The procedure is repeated until the convergence between two subsequent iterations is reached, resulting in the final solution for the new time step.

The multiphase flow with a specific amount of the participated components can be simulated by referring to one of the models provided by DuMux and then modifying it to the required needs. For example, in this study, the 2pncmin model was used. This model can be interpreted as the two-phase n-component flow of two compressible and partially miscible fluids in

combination with mineral precipitation and dissolution. The standard multiphase Darcy approach is used as the equation for the conservation of momentum (Eq. 12). By inserting Darcy's law into the equations for the conservation of the components, it gets one transport equation for each component. Per default, Darcy's and Fick's laws are used for the fluid phase velocities and the diffusive fluxes. The solid or mineral phase is assumed to consist of a single component. Its mass balance consists only of storage and a source term. The model in principle uses mole fractions instead of mass fractions. To control the phase presence state, variable switch controlling was implemented. The phase switch occurs when the equilibrium concentration of a component in a phase is exceeded, instead of the sum of the components in the virtual phase (the phase which is not present) being greater than unity. The phase partitioning is performed in the "CO₂VolumeVariables" file, in comparison to other models, it does not use a constraint solver for calculating the mole fractions (Figure 27). Instead, the mole fractions are calculated in the FluidSystem under the provided temperature, pressure, and salinity, according to the Spycher and Pruess (2004) derivation. The porosity is updated according to the reduction of the initial (or solid-phase-free porous medium) porosity by the accumulated volume fractions of the solid phases. Additionally, the permeability is recalculated, based on the current porosity, and using the Kozeny-Carman formulation (Eq. 43).

```

a) // if both phases are present the mole fractions in each phase can be calculate
// with the mutual solubility function
if (knownPhaseIdx < 0)
{
    const Scalar molalityNaCl = molFracToMolality(x_NaCl); // molality of NaCl //CHANGED
    const Scalar m0_CO2 = molalityCO2inPureWater(temperature, pg); // molality of CO2 in pure water
    const Scalar gammaStar = activityCoefficient(temperature, pg, molalityNaCl); // activity coefficient of CO2 in brine
    const Scalar m_CO2 = m0_CO2 / gammaStar; // molality of CO2 in brine
    xLCO2 = m_CO2 / (molalityNaCl + 55.508 + m_CO2); // mole fraction of CO2 in brine
    yGH2O = A * (1 - xLCO2 - x_NaCl); // mole fraction of water in the gas phase
}

// if only liquid phase is present the mole fraction of CO2 in brine is given and
// and the virtual equilibrium mole fraction of water in the non-existing gas phase can be estimated
// with the mutual solubility function
if (knownPhaseIdx == lPhaseIdx)
    yGH2O = A * (1 - xLCO2 - x_NaCl);

// if only gas phase is present the mole fraction of water in the gas phase is given and
// and the virtual equilibrium mole fraction of CO2 in the non-existing liquid phase can be estimated
// with the mutual solubility function
if (knownPhaseIdx == gPhaseIdx)
    xLCO2 = 1 - x_NaCl - yGH2O / A;

b) // calculate the phase compositions
typename FluidSystem::ParameterCache paramCache;
// both phases are present
if (phasePresence == bothPhases)
{
    //Get the equilibrium mole fractions from the FluidSystem and set them in the fluidState
    //xCO2 = equilibrium mole fraction of CO2 in the liquid phase
    //yH2O = equilibrium mole fraction of H2O in the gas phase
    const auto xLCO2 = FluidSystem::equilibriumMoleFraction(fluidState, paramCache, phase0Idx);
    const auto xGH2O = FluidSystem::equilibriumMoleFraction(fluidState, paramCache, phase1Idx);
    const auto xLH2O = 1 - xLCO2 - priVars[comp2Idx];
    const auto xGC02 = 1 - xGH2O;
    fluidState.setMoleFraction(phase0Idx, comp0Idx, xLH2O);
    fluidState.setMoleFraction(phase0Idx, comp1Idx, xLCO2);
    fluidState.setMoleFraction(phase0Idx, comp2Idx, priVars[comp2Idx]);
    fluidState.setMoleFraction(phase1Idx, comp0Idx, xGH2O);
    fluidState.setMoleFraction(phase1Idx, comp1Idx, xGC02);
    fluidState.setMoleFraction(phase1Idx, comp2Idx, 0.0);
}

```

Figure 27 CO₂/Brine phases partitioning (part of the code): a) Pre-calculation using Pruess and Spycher's (2004) approach; b) Phase composition calculation within the model.

$$43) \text{ Permeability is calculated from porosity using } k_{ij} = Ak_{ij}^0 \frac{\phi^n}{(1-\phi)^m}$$

Where, k_{ij} is a tensor providing the anisotropy, ϕ is porosity, n and m are positive scalar constants and A is given by $A = k_0(1-\phi_0)^m/\phi_0^n$ (where k_0 and ϕ_0 are a reference permeability and porosity).

The next important consideration is the appropriate fluid system. A brine/CO₂ fluid system is a compositional fluid with brine (H₂O & NaCl) and carbon dioxide as components in both the liquid and the gas (supercritical) phase. Initially, the thermodynamical properties of each component are pre-defined separately, the example of brine viscosity is provided below (Figure 28). Then, each component (CO₂, Brine, NaCl) with pre-calculated fluid properties is imported in a compositional fluid system, where each parameter is found, considering all the physical and thermodynamical mixing mechanisms, the example of liquid density after interaction between CO₂ and Water phases (Figure 29).

```
template <class FluidState>
static Scalar viscosity(const FluidState& fluidState, int phaseIdx = liquidPhaseIdx)
{
    assert(phaseIdx == liquidPhaseIdx);
    const Scalar temperature = fluidState.temperature(phaseIdx);
    const Scalar xNaCl = fluidState.massFraction(phaseIdx, NaClIdx);

    using std::pow;
    using Dune::power;
    using std::exp;
    using std::max;
    const Scalar T = max(temperature, 275.0);
    const Scalar salinity = max(0.0, xNaCl);

    const Scalar T_C = T - 273.15;
    const Scalar A = ((0.42*power((pow(salinity, 0.8)-0.17), 2)) + 0.045)*pow(T_C, 0.8);
    const Scalar mu_brine = 0.1 + (0.333*salinity) + (1.65+(91.9*salinity*salinity*salinity))*exp(-A); // [cP]
    assert(mu_brine > 0.0);
    return mu_brine/1000.0; // [Pa·s]
}
```

Figure 28 Viscosity of brine calculated as a separate component.

```
static Scalar liquidDensityWaterCO2_(Scalar temperature,
                                     Scalar pI,
                                     Scalar xLH2O,
                                     Scalar xLCO2)
{
    const Scalar M_CO2 = CO2::molarMass();
    const Scalar M_H2O = H2O::molarMass();

    const Scalar tempC = temperature - 273.15; /* tempC : temperature in °C */
    const Scalar rho_pure = H2O::liquidDensity(temperature, pI);

    // xLH2O is available, but in case of a pure gas phase
    // the value of M_T for the virtual liquid phase can become very large
    xLH2O = 1.0 - xLCO2;
    const Scalar M_T = M_H2O * xLH2O + M_CO2 * xLCO2;
    const Scalar V_phi = (37.51 +
                        tempC*(-9.585e-2 +
                        tempC*(8.74e-4 -
                        tempC*5.044e-7))) / 1.0e6;
    return 1/(xLCO2 * V_phi/M_T + M_H2O * xLH2O / (rho_pure * M_T));
}
```

Figure 29 Liquid density of CO₂ and Water in the compositional fluid system

Having the functioning fluid system and model it is possible to proceed to the creation of the application, which is composed of the following files:

- the main function (main. cc) which is responsible for defining the solvers (linear/nonlinear), calling the grid assembler, setting the temporal discretization scheme, timing, and exporting the simulation results (Figure 30). This linear solver is based on the biconjugate gradient stabilized method (BiCGSTAB) and the ILU preconditioner (The DuMux Handbook, 2021). BiCGSTAB is an iterative algorithm used to solve large asymmetric linear systems (Ochoń et al., 2013).

```
// the assembler with time loop for instationary problem
using Assembler = FVAssembler<TypeTag, DiffMethod::numeric>;
auto assembler = std::make_shared<Assembler>(problem, gridGeometry, gridVariables, timeLoop, xOld);

// the linear solver
using LinearSolver = Dumux::ILU0BiCGSTABBackend;
auto linearSolver = std::make_shared<LinearSolver>();

// the non-linear solver
using NewtonSolver = NewtonSolver<Assembler, LinearSolver>;
NewtonSolver nonLinearSolver(assembler, linearSolver);
```

Figure 30 Part of the main.cc file, with defined solvers and assemblers.

- the input file (params. input) is used to define the simulation parameters and conditions used at runtime, i.e. such as grid mesh, timestep size, simulation time, temperature, pressure, injection rate, rock properties (porosity, permeability), and flow properties (relative permeabilities and capillary pressure).

```
[SpatialParams]
SolubilityLimit      = 0.26           # [-] solubility limit of NaCl in brine
referencePorosity    = 0.221          # [-] initial porosity
referencePermeability = 9.020478962e-13 # [m²] initial permeability
BrooksCoreyPcEntry   = 2500
BrooksCoreyLambda    = 0.67
VanGenuchtenN        = 1.864         # Van Genuchten parameter
VanGenuchtenAlpha    = 2.4e-4        # Van Genuchten parameter
Swr                  = 0.11          # [-] irreducible liquid saturation
Snr                  = 0.025         # [-] irreducible gas saturation

[Grid]
Positions0 = 0 0.2 1
Positions1 = 0 0.1
Cells0     = 40 80
Cells1     = 10

[Problem]
Name           = test_2pncmini      # [-] name for output files
EnableGravity = true
Temperature    = 315                # [K] initial temperature
InitialPressure = 1.1e7             # [Pa] Initial reservoir pressure
InitialSalinity = 0.24              # [-]=[kgNaCl/kgSolution] Initial salt mass fraction
InjectionRate  = 0.002
```

Figure 31 Part of the params.the input file, with defined conditions and parameters.

- the problem file (problem.hh) which defines the mathematical model, initial and boundary conditions as well as the source/sink terms.

```

NumEqVector source(const Element &element,
                  const FVElementGeometry& fvGeometry,
                  const ElementVolumeVariables& elemVolVars,
                  const SubControlVolume &scv) const
{
    NumEqVector source(0,0);

    const auto& volVars = elemVolVars[scv];

    Scalar moleFracNaCl_wPhase = volVars.moleFraction(LiquidPhaseIdx, NaClIdx);
    Scalar massFracNaCl_Max_wPhase = this->spatialParams().solubilityLimit();
    Scalar moleFracNaCl_Max_wPhase = massToMoleFrac(massFracNaCl_Max_wPhase);
    Scalar saltPorosity = this->spatialParams().minimalPorosity(element, scv);

    // precipitation of amount of salt which hexceeds the solubility limit
    using std::abs;
    Scalar precipSalt = volVars.porosity() * volVars.molarDensity(LiquidPhaseIdx)
                      * volVars.saturation(LiquidPhaseIdx)
                      * abs(moleFracNaCl_wPhase - moleFracNaCl_Max_wPhase)
                      / timeStepSize_;

    if (moleFracNaCl_wPhase < moleFracNaCl_Max_wPhase)
        precipSalt += -1;

    // make sure we don't dissolve more salt than previously precipitated
    if (precipSalt*timeStepSize_ + volVars.solidVolumeFraction(sPhaseIdx)* volVars.solidComponentMolarDensity(sPhaseIdx) < 0)
        precipSalt = -volVars.solidVolumeFraction(sPhaseIdx)* volVars.solidComponentMolarDensity(sPhaseIdx)/timeStepSize_;

    // make sure there is still pore space available for precipitation
    if (volVars.solidVolumeFraction(sPhaseIdx) >> this->spatialParams().referencePorosity(element, scv) - saltPorosity && precipSalt > 0)
        precipSalt = 0;

    source[contiEqIdx + NaClIdx] += -precipSalt;
    source[precipNaClEqIdx] += precipSalt;
    return source;
}

```

Figure 32 Part of the problem.hh file, the example of the salt precipitation mechanism (when the NaCl solubility limit is exceeded), defined as a source term.

- the spatial parameters file (spatialparams.hh) which characterizes the porous medium (relative permeability, capillary pressure, wetting phase, etc.). Regarding the available models for the relative permeability and capillary pressure modelling, DuMux has both the Brooks-Corey (Brooks and Corey, 1966) and van Genuchten's (van Genuchten, 1980) correlations (Chapter 2.3.1).

```

//using PckrSwCurve = FluidMatrix::BrooksCoreyDefault<Scalar>;
using PckrSwCurve = FluidMatrix::VanGenuchtenDefault<Scalar>;

static const int dimWorld = GridView::dimensionworld;

using GlobalPosition = typename SubControlVolume::GlobalPosition;

public:
    // type used for the permeability (i.e. tensor or scalar)
    using PermeabilityType = Scalar;

    SalinizationSpatialParams(std::shared_ptr<const GridGeometry>gridGeometry)
    : ParentType(gridGeometry)
    , pckrSwCurve("SpatialParams"), K_(gridGeometry->gridView().size(0), 0.0)
    {
        temperature_ = getParam<Scalar>("Problem.Temperature");
        solubilityLimit_ = getParam<Scalar>("SpatialParams.SolubilityLimit", 0.26);
        referencePorosity_ = getParam<Scalar>("SpatialParams.referencePorosity", 0.11);
        referencePermeability_ = getParam<Scalar>("SpatialParams.referencePermeability", 2e-14);
    }
}

```

Figure 33 Part of the spatialparams.hh file, where the relative permeability/capillary and reference parameters for the Kozeny-Carman models are pre-defined.

3.3 Moose

Multiphysics Object-Oriented Software Environment (MOOSE) is an open-source C++ framework from Idaho National Laboratory (A.Lindsay et al., 2022) that provides an easily employed design of two underlying software libraries: the libMesh finite element library (B.Kirk et al., 2006), and the PETSc nonlinear solver library (S. Balay et al., 2017). The main attention is dedicated to the porous flow module that was developed for the description of the general non-isothermal, multicomponent, multiphase framework, including advection, diffusion, and dispersion of fluid components and conduction and advection of heat (C.Green, A.Wilkins, 2020). It is based on the high-precision equations of state for both brine and CO₂, implementing mutual solubility of CO₂ into the liquid brine and vice versa water vapor into the CO₂-rich phase (C.Green, A.Wilkins, 2018). The phase partitioning is calculated in the same manner as in the previous simulators, using the accurate fugacity-based formulation by Spycher et al. (2003) and Spycher et al. (2005). If the dissolution of CO₂ into the brine and evaporation of brine into the CO₂ phase happens instantaneously, signifying that these phases are preserved in instantaneous chemical equilibrium without adding reaction kinetics. The porous flow module is capable to work with a variety of non-linear variables, solving the equations based on phase pressures, saturations, mass fractions, and temperature. In addition, the simulation of miscible multiphase problems leads to phase switching (from one phase to two phases and vice versa), depending on the thermodynamical conditions. For this purpose, the primary variable switch mechanism was implemented. For example, to model the flow of only one phase the flowing variable can be used - the pressure, temperature, and mass fraction of a component in the phase (Figure 34). However, if the phase state has switched to a two-phase model, then the mass fraction variable is replaced by the saturation of one of the fluid phases (C.Green, A.Wilkins, 2018).

Phase state	Variable 1	Variable 2	Variable 3
Single phase	P_α	T	X_α^κ
Two phases	P_α	T	S_α

Figure 34 Primary variables in miscible two-phase mode, where P_a represents the pressure of phase a , T denotes the temperature, X_a^κ is the mass fraction of component κ in phase a and S is the saturation of the phase a (C.Green, A.Wilkins, 2018).

The main advantage of Moose over DuMux is the simplicity of use because Moose does not require managing so many different input files. Each term of a partial differential equation, which represents the physical mechanism related to the flow equation, can be simply induced in one input file. In addition, there are several hundred examples of input files, explaining and representing the performance of each part of the Porous Flow module (C.Green, A.Wilkins, 2018). The parts of the input file are provided below:

```

a) [Mesh]
   type = GeneratedMesh
   dim = 2
   nx = 100
   ny = 5
   xmin = 0.1
   xmax = 1.1
   ymin = 0.0
   ymax = 0.1
   []

b) [Kernels]
   [mass0]
   type = PorousFlowMasTimeDerivative
   fluid_component = 0
   variable = pgas
   []
   [flux0]
   type = PorousFlowAdvectiveFlux
   fluid_component = 0
   variable = pgas
   []

```

Figure 35 a) The mesh description; b) The brine phase flow equation as input (mass and advective terms).

```

a) [UserObjects]
   [dictator]
   type = PorousFlowDictator
   porous_flow_vars = 'pgas zi xnacl'
   number_fluid_phases = 2
   number_fluid_components = 3
   []
   [pc]
   type = PorousFlowCapillaryPressureBC
   lambda = 0.67
   pe = 2.5e3
   sat_lr = 0.11
   []

b) [relperm_liquid]
   type = PorousFlowRelativePermeabilityBC
   phase = 0
   s_res = 0.11
   sum_s_res = 0.135
   nw_phase = false
   lambda = 0.67

```

Figure 36 a) The definition of a non-linear variable, several phases, and some components, an example of the Brooks-Corey capillary pressure input; b) Example of the Brooks-Corey relative permeability input.

```

a) [BCs]
   [co2_injection]
   type = PorousFlowSink
   boundary = left
   variable = zi
   flux_function = -0.002
   use_mobility = false
   use_relperm = false
   fluid_phase = 0
   []

b) [rightco2liq]
   type = PorousFlowPiecewiseLinearSink
   boundary = 'right'
   variable = zi
   use_mobility = true
   PorousFlowDictator = dictator
   fluid_phase = 0
   multipliers = '0 1e9'
   PT_shift = '1.1e7'
   pt_vals = '0 1e9'
   mass_fraction_component = 1
   use_relperm = true
   []

```

Figure 37 a) The example of the inflow(source) boundary; b) the example of the outflow boundary related to the liquid phase of the CO₂ component.

Chapter 4

Results and Discussion

4.1 Input parameters

The simulations were performed on the 1-D, 2-D, and 3-D domains with gravity in all cases pointing downwards, therefore the effect of gravity segregation due to density difference and buoyancy effect is observed in the 2-D and 3-D simulations. It was assumed that injection is performed in the Berea sandstone rock core (rock properties are provided in Table 2), with the dimensions of 1 meter in length and 10 centimeters in diameter. The domain is initially fully saturated with brine, with 24% of the mass fraction of dissolved salt (NaCl). At $t = 0$, with the described in Table 2 conditions signifying the critical state of CO_2 , injection starts from the left side of the domain with a constant flow rate. The inlet boundary is represented by NeumannBC boundary conditions, it is used for describing flux boundary conditions on systems of partial differential equations (PDEs). The outlet is represented by a Dirichlet boundary of constant pressure and temperature, it was done to achieve an infinitely acting aquifer system. This means that the last grid block of the simulated domain is located outside the outlet of the porous core plug and has constant properties for all time steps. The upper and lower boundaries were assumed to be impermeable and represented by no-flow NeumannBC to both scCO_2 and brine, mimicking the caprocks positioned above and below providing perfect sealing conditions (Figure 38). The 3-D model was prepared in the three-dimensional finite element mesh generator Gmsh (Geuzaine.C, Remacle J.-F, 2009), with appropriate dimensions and the same boundary conditions. It should be mentioned that there is a misinterpretation of the injection rate for both DuMux and Moose in comparison to TOUGH2. For example, to achieve the desired rate of 20m/min, the value of approximately 0.02 kg/s should be provided as input for DuMux and Moose, while for the TOUGH2 – 0.002 kg/s. Final remark should be made regarding precipitation mechanism for the Moose application. So far, the process of salt precipitation after reaching the solubility limit was not implemented in Moose code, therefore, the evaluation is only performed on salt mass fraction presented in brine, which can tend to maximum value of 1. However, the dry-out region and the time reaching the solubility limit of 26% are reasonably distinguishable.

Parameter	Value	Unit
[Grid]		
Grid mesh dimensions 2-D	100x10	cm
Number of grid cells	1D – 320 grid-blocks in x - direction	2-D – 120 grid-blocks in x-direction; 10 in y-direction
Gravity	Enabled	-
[Fluid system]		
Temperature	315	Kelvin
Pressure	110	Bar
Initial salinity	24	%
Injection rates	2 or 20	ml/min
The solubility limit of salt mass fraction	26	%
[Rock properties]		
Reference porosity	0.221	%
Reference permeability	9.02E-13	m ²
Brooks-Corey entry pressure	2500	Pa
Brooks-Corey lambda	0.67	
Van Genuchten N parameter	1.864	
Van Genuchten alpha	2.4E-04	
Swr	0.11	
Snr	0.025	

Table 2 Initial parameters of the simulated model.

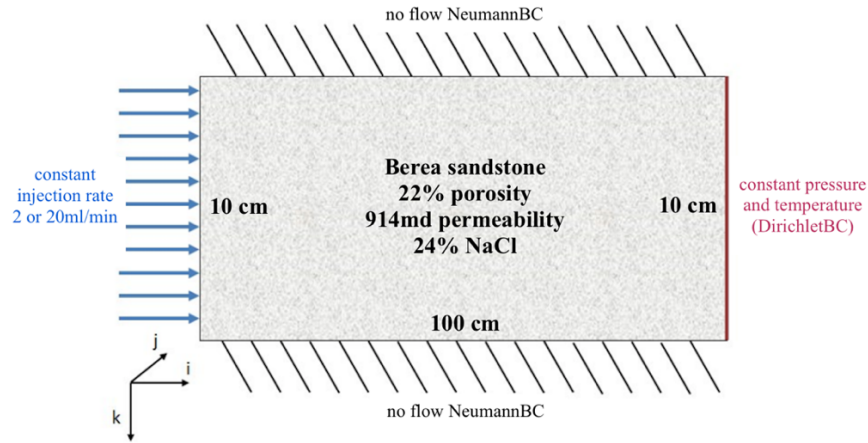


Figure 38 Boundary conditions of the 2-D simulations.

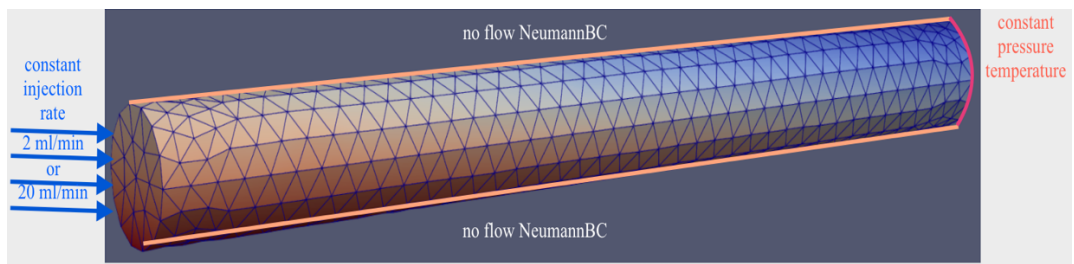


Figure 39 Boundary conditions of the 3-D simulations.

The applied CO₂-brine relative permeability and capillary pressure curves were calculated based on retention relations proposed by van Genuchten (1980) and Brooks–Corey (1964), the applied equations are extensively described in Chapter 2.3.1. The provided values are adopted based on experimental S – Pc and kr – S data performed by Krevor et al.(2012). According to that study, the S – Pc data were obtained by conducting a standard mercury injection method. Then, these data were reproduced to brine–CO₂ systems assuming a brine–CO₂ interfacial tension of 32 mN/m and a contact angle of 40° (Krevor et al.,2012; Oostrom et al.,2016). A series of steady-state drainage experiments were performed to obtain the kr – S relationship, while in-situ saturation was monitored using an X-ray CAT scanner (Krevor et al., 2012; Perrin and Benson, 2010). The data used and relative permeability and capillary pressure curves are presented in Figure 40 and Figure 41a/b.

Model	Berea	
	S – Pc	kr – S
Van Genuchten	$\alpha = 2.4 \times 10^{-4} \text{ 1/Pa}$ $n_v = 1.864$ $m_v = 0.464$ $S_{ij} = 0.11$	$m_v = 0.464$
Brooks-Corey	$P_e = 2.5 \times 10^3 \text{ Pa}$ $\lambda = 0.67$ $S_{ij} = 0.11$	$\lambda = 0.67$

Table 3 Data for modelling the relative permeability and capillary pressure (Oostrom et al.,2016).

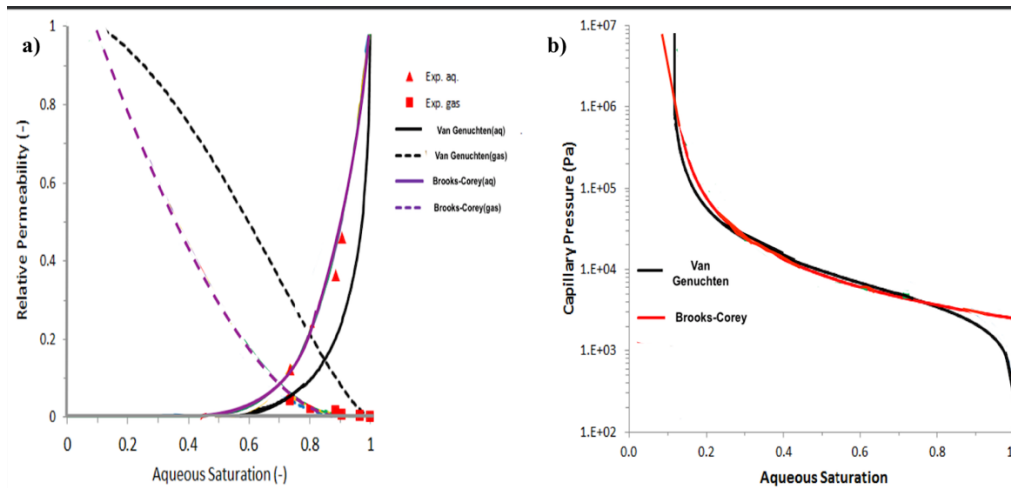


Figure 40 a) The relative permeability curves; b) The capillary pressure curves for Berea sandstone (adopted from Krevor et al.,2012; Oostrom et al.,2016).

The simulations were performed comparing heterogeneous and homogeneous scenarios. To achieve the heterogeneity, the porosity was randomly distributed along the core with a value between 0.19 and 0.23, then by applying the Kozeny-Carman grain model, the permeability was randomly recalculated according to porosity (Figure 41). Another approach was used in DuMux for utilizing heterogeneity. In this case, the heterogeneity was generated applying random fields using lognormal distributions, with initial permeability as mean value and 20 % of it as standard deviation (Figure 42).

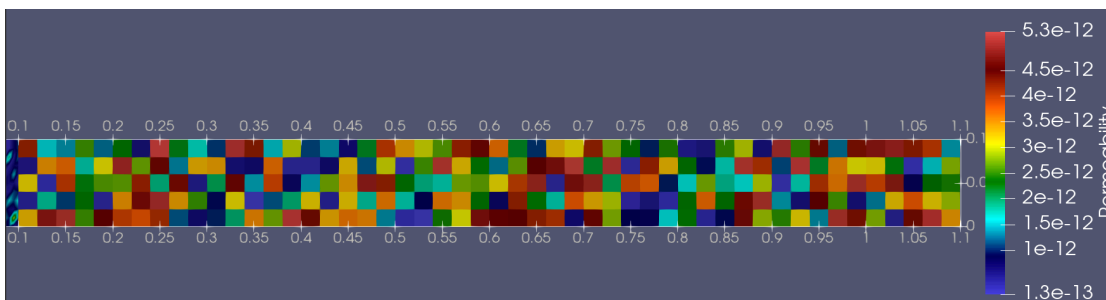


Figure 41 Permeability distribution for the heterogeneous simulation in Moose.

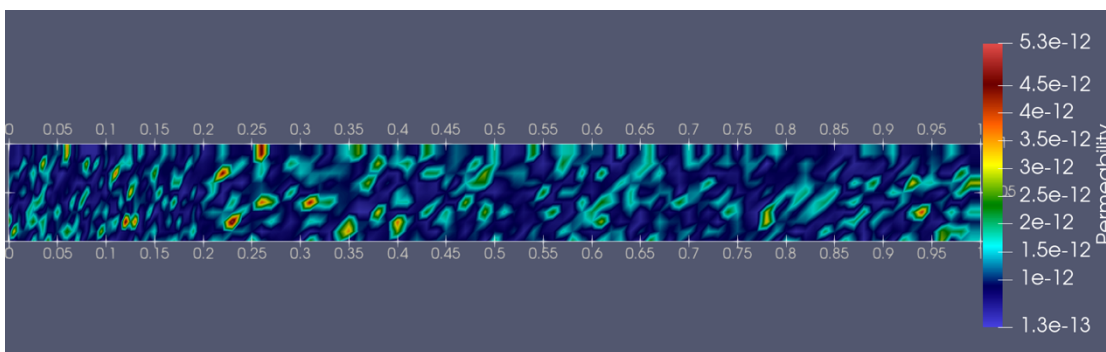


Figure 42 Permeability distribution for the heterogeneous simulation in DuMux.

4.2 Results and Discussion Section

4.2.1 Effect of heterogeneity, relative permeability, and capillary pressure.

1. Effect of relative permeability on front propagation and gas saturation

The contribution from the appropriate relative permeability model was evaluated by assuming the CO₂ injection into a homogeneous 1-D domain of 1m length, which was saturated with 24% brine solution. However, such a drastic simplification of the simulation would not provide realistic results for mimicking laboratory experiments, it provides an insight into the injection process by exploiting the “similarity property” of the mathematical solution (K.Pruess, N.Muller, 2009). In addition, the 2-D simulations were conducted to confirm the observations from the 1-D runs. The starting point was to perform the injection with a rate of 20ml/min and zero capillary pressure. It should be noted that results from TOUGH2 simulator will be included in the comparison. The assumption of the TOUGH2 model is the application of the Van Genuchten relative permeability and capillary pressure.

Interesting behavior can be noted about the front propagation using the Brooks-Corey relative permeability model. The shock front for this model was predicted almost twice larger compared to the Van Genuchten model. However, the extent of the average scCO₂ saturation over the plume length was proportionally shorter, signifying the faster breakthrough for the Van Genuchten model. In Figure 43 it can be observed that for the VG model the breakthrough was around 800 seconds or 0.15PV, while for the BC model the breakthrough was around 2000 seconds or 0.33PV. This behavior can be explained by referring to the Corey liquid relative permeability – Saturation relation, which significantly overestimates liquid relative permeability values of the pertinent saturation range in comparison to the Van Genuchten model. Therefore, the brine is easier to be displaced for the Brooks-Corey model, leading to larger average gas saturations and a shorter plume extent. Contrarily, the application of the VG model leads to the further migration of injected CO₂, because the gas relative permeability values for the VG model are much larger as a function of gas saturation compared to the BC model.

According to Oostrom et al. (2016), the BC relative permeability relation has a better match with the experimental data, resulting in good fits to both the $S - P_c$ and $k_r - S$ experimental data. Therefore, the 2-D simulations are performed mostly considering the BC model as a reference in the evaluation.

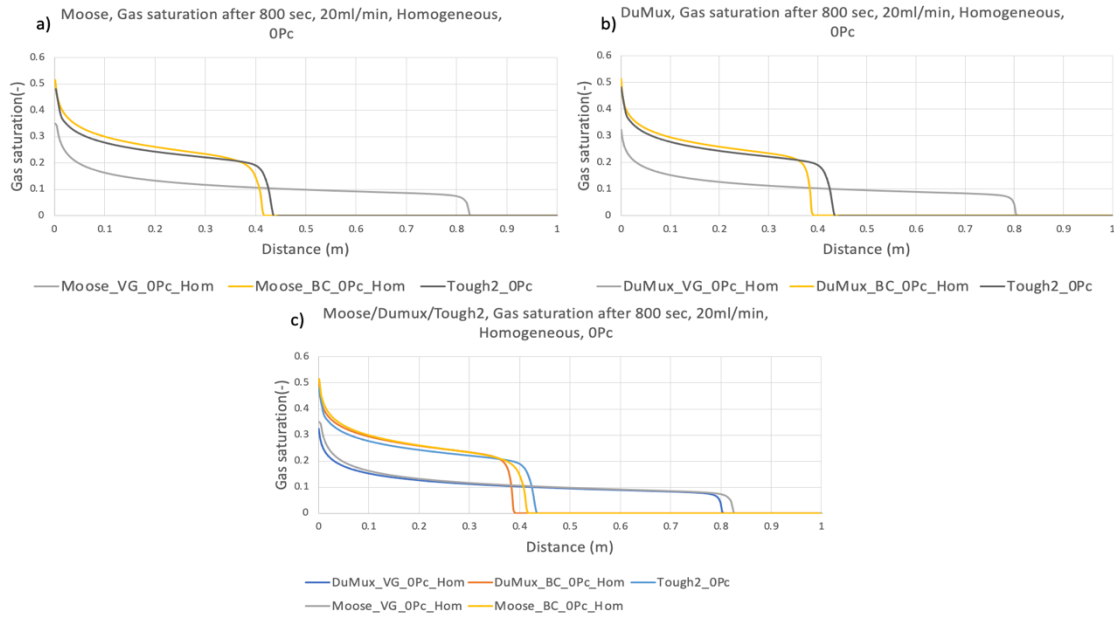


Figure 43 a) Saturation front propagation comparing Brooks-Corey(BC) and Van Genuchten(VG) models, after 800 seconds using Moose; b) Using DuMux; c) Comparison of front propagation for Moose, DuMux and TOUGH2.

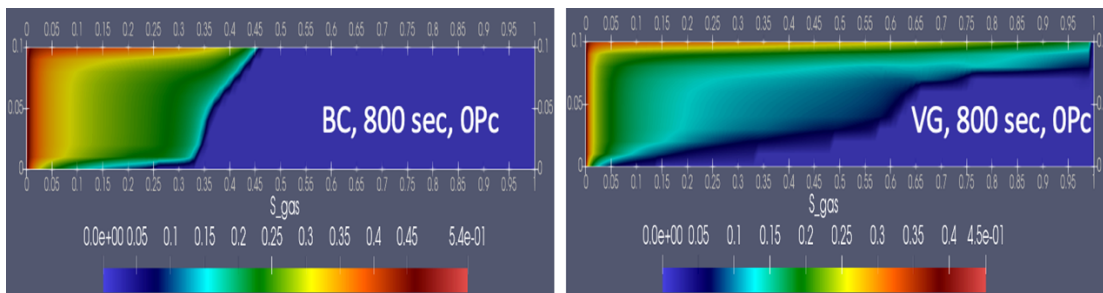


Figure 44 Visual representation of front propagation for (left) Brooks-Corey, (right) Van Genuchten relative permeability models, without capillary pressure.

Throughout the simulations, in the case of using the BC model, the dry-out zone is extended slightly farther and at the same time, the saturation profile after 10PV injected shows higher average saturation along the domain (Figure 45). The farther extent of the dry-out zone for the BC model can be explained by faster achieving the drying-out gas saturation. As it was mentioned before BC provides larger average gas saturations, and after achieving the breakthrough, the parameter such as the extent of the plume (shorter for BC) does not affect on time required to reach the critical gas saturation. However, higher salt precipitation was observed for the VG model (Figure 46 and Figure 48). This behavior is similar to the effect of capillary pressure presence because in Figure 48(a) more localized and higher salt precipitation was observed closer to the inlet. Since the extent of the dry-out zone is less, locally the dry-out saturation is achieved faster leading to slightly more potential for higher and more localized salt precipitation.

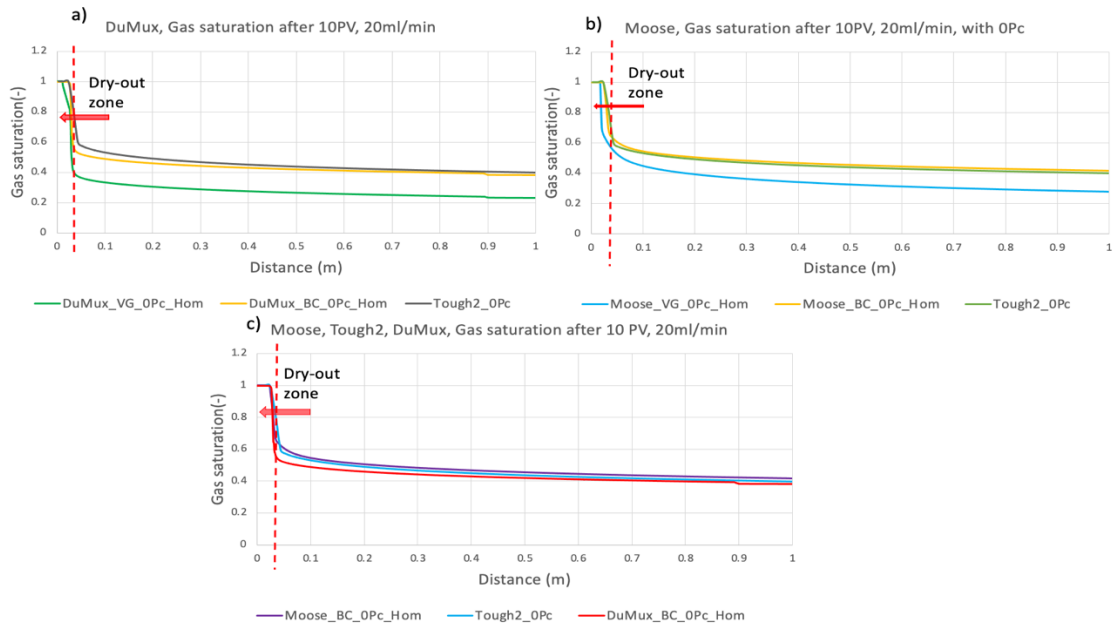


Figure 45 a) Gas saturation distribution along the core after 10PV injected (DuMux); b) Moose; c) Comparison between DuMux, Moose, and TOUGH2.

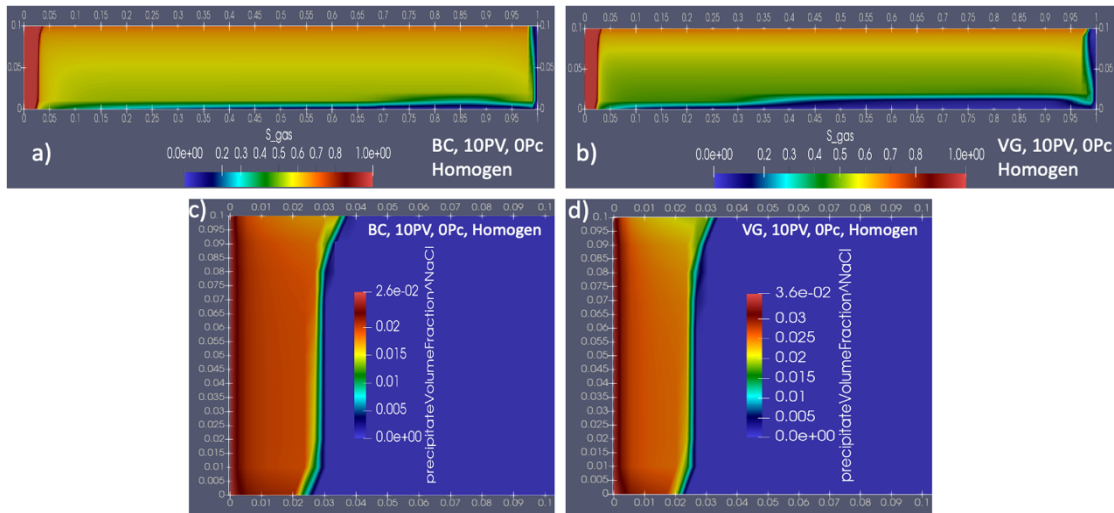


Figure 46 a) Gas saturation distribution along the core after 10PV injected using BC model; b) Gas saturation using VG model; c) The extent of the dry-out zone and salt precipitation using BC model; d) Salt precipitation using VG model.

The impact evaluation from the relative permeability models reveals that the Brooks-Corey approach provides more practical results, specifically in these simulation scenarios, and represented the Berea sandstone core domain. In addition, Figure 45 and Figure 47 show that the performance wisely all three simulators provide comparable results in terms of gas saturation distribution along the core and specifically gas saturation growth at the first grid of the domain, where the gas saturation was reached approximately between 5 and 6 hours of constant injection. The possible mismatch can be caused by different discretization methods, and thermophysical properties calculation because all the simulators refer to the various

equations. For example, TOUGH2 employs a tabular EOS based on Altunin's correlation (1975), while Moose and DuMux refer to the Span and Wagner equation of state. In addition, for brine viscosity calculation TOUGH2 applies the EWASG from a correlation presented by Phillips et al. (1981), but DuMux considers the equation presented by Batzle and Wang (1992).

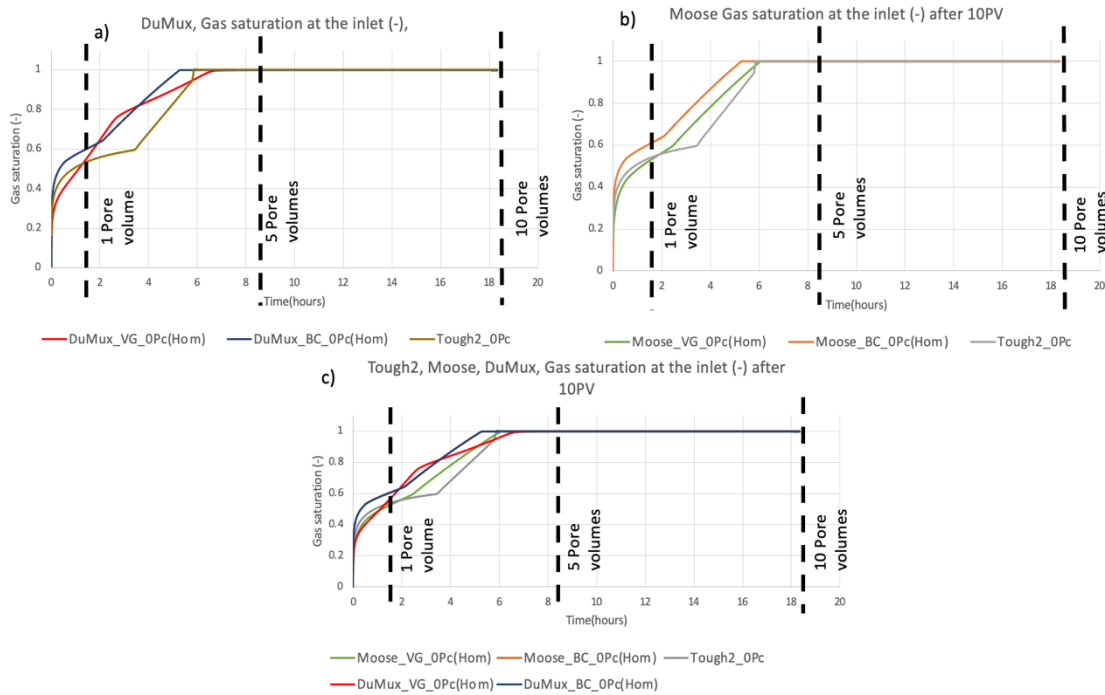


Figure 47 a) Gas saturation at the inlet (1st grid cell) after 10PV injected using DuMux, comparing BC and VG models; b) Gas saturation at the inlet after 10PV injected using Moose; c) The comparison between simulators using different relative permeability models.

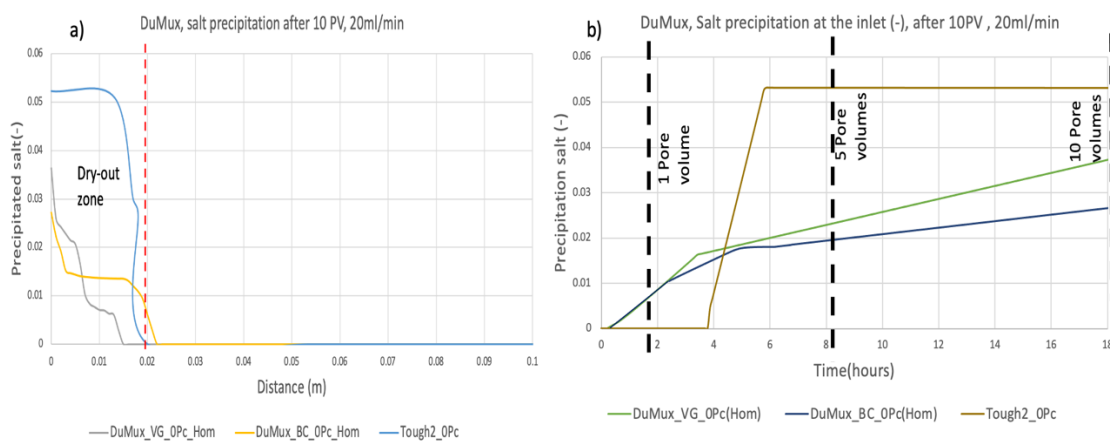


Figure 48 a) Precipitated salt distribution along the domain after 10PV; b) Evolution of salt precipitation at the inlet with the time.

2. Effect of heterogeneity on front propagation, gas saturation, and salt precipitation

Injection of CO₂ into more realistic heterogeneous media results in more-complex processes of multiphase flow, non-uniform formation dry-out, and more distributed salt precipitation. However, the implementation of heterogeneity into numerical simulation is a more complex task, therefore assuming that the heterogeneity was described with one single set of parameters, by averaging of porosity and permeability, the $k_r(S_w)$ and $P_c(S_w)$ are mainly the pseudo functions (H.Ott et al., 2011). For these simulation cases, the heterogeneity was generated from the random distribution of the reference permeability of 810mD with a variability of 20%. From the 1-D results (Figure 49), there is no obvious effect of heterogeneity on the front propagation, only a minor front advantage was distinguished for the Moose simulations. However, in the 2-D visualization (Figure 50) the more prominent effect of heterogeneity can be observed, with faster front propagation of around 5 cm. That is evidently induced by channeling in more permeable zones which signifies more domination in a low-viscous displacing phase. For the VG model there is a strong gravity over-run of the CO₂ phase, resulting in the early breakthrough, which is observed at the top (Figure 50(c), (d)). The channeling mechanism is initiated when the displacement front is governed by the influence of the rock properties, for example, a variation in permeability or highly porous zone, which is in conjunction with variation in relative permeability and capillary pressure. The consequence of channeling results in unswept areas, hence, in higher saturation of the bypassed brine (higher residual saturation).

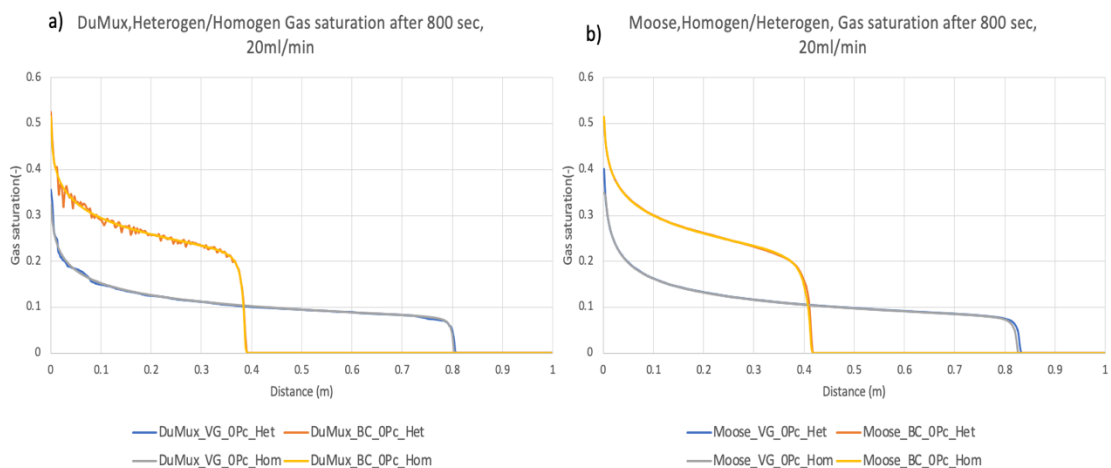


Figure 49 a) Saturation front propagation comparing Homogeneous and Heterogeneous models, after 800 seconds using Moose; b) Using DuMux.

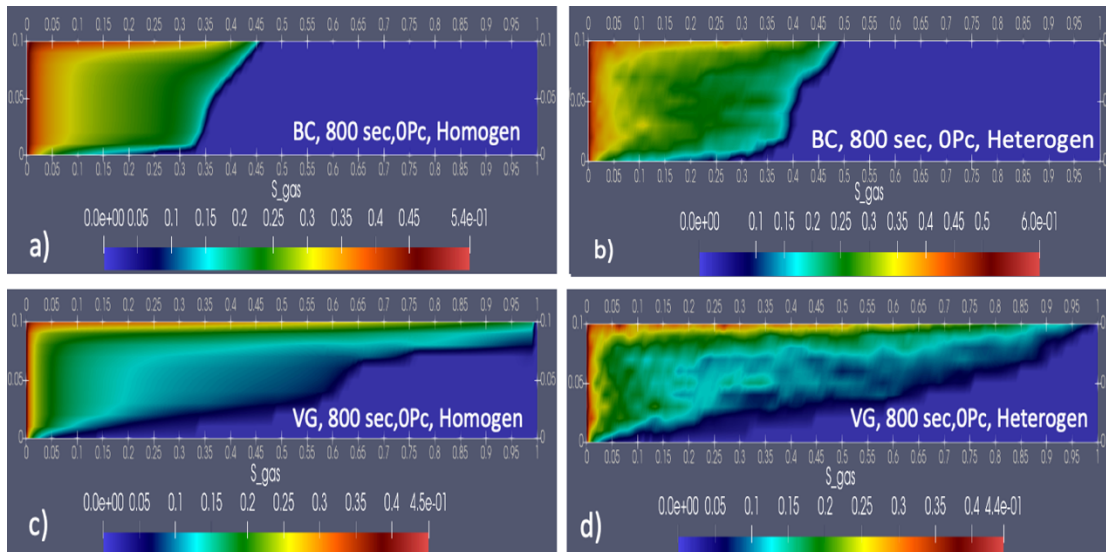


Figure 50 a) and b) Comparison of BC model for Homogeneous/Heterogeneous cases; c) and d) Comparison of VG model for Homogeneous/Heterogeneous cases.

From Figure 51, it can be concluded that such minor variation in heterogeneity does not affect the extent of the dry-out zone. However, further investigation has to be done for more complex rock structure, for example – carbonates. For both simulators, DuMux and Moose assuming 0 Pc conditions and after 10PV of CO₂ injected, the length of the dry-out zone is the same – around 3 cm at the inlet. However, an additional comparison of the VG and BC relative permeability models has shown that due to the average gas saturation for the VG model being notably lower, the extent of the dry-out is respectively shorter. Further, Figure 52 confirmed that due to the faster breakthrough the maximum gas saturation for the heterogeneous cases is achieved faster, but it should be noted that the faster breakthrough and faster progress of gas saturation at the inlet did not have an influence on the dry-out extent.

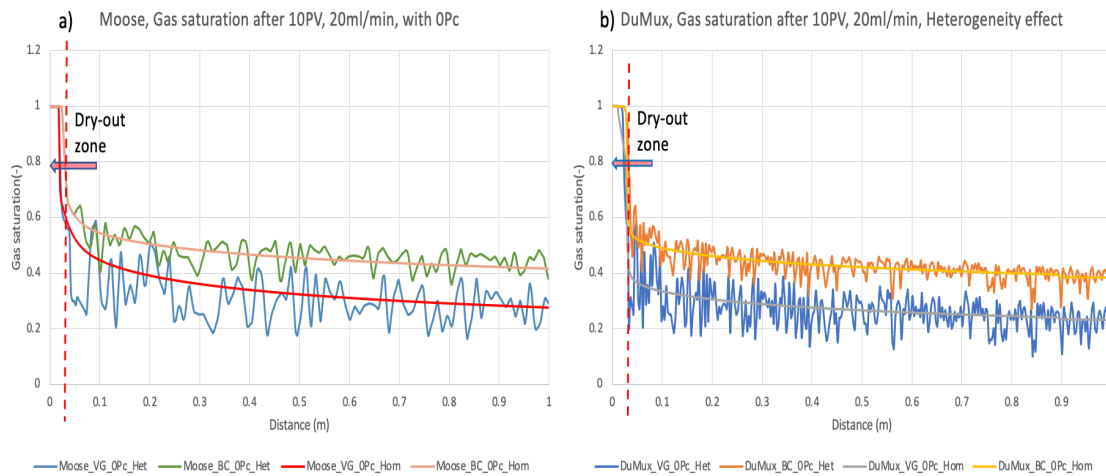


Figure 51 a) Gas saturation(dry-out) along the domain after 10PV injected in Moose; b) Gas saturation(dry-out) after 10PV injected in DuMux.

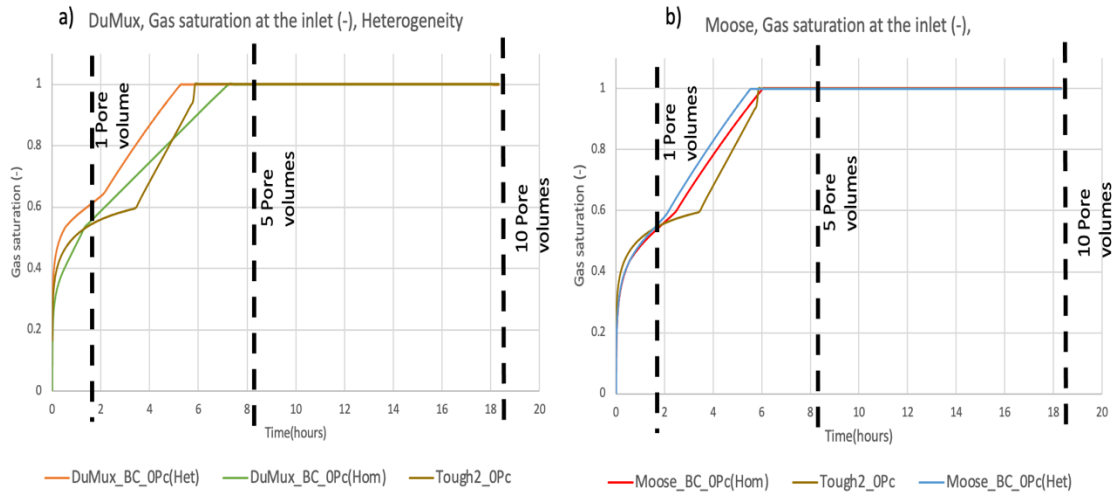


Figure 52 a) Gas saturation at the inlet (1st grid cell) after 10PV injected using DuMux, heterogeneity evaluation; b) Gas saturation at the inlet after 10PV injected using Moose.

In terms of salt precipitation, the heterogeneity is only influenced by the pattern and distribution of the precipitate. It can be seen in Figure 53 and Figure 54 that the extent of the precipitation is the same for homogeneous and heterogeneous cases – 3 cm, but in Figure 54 the minor spikes in the amount of precipitation are distinguishable. This can signify that salt is asymmetry accumulated at the zones of higher permeability. Hypothetically, with the assumption of reaction kinetics, this salt distribution would be more visible, where the brine from the highly permeable pore throats would be evaporated faster, leading to more distributed precipitation. In addition, the significant effect of heterogeneity is more expressed under the additional action of capillary back flow. Having a more prominent distribution of the pore throats would result in more opportunities for the brine to be supplied in the dry-out area due to capillary pressure back flow, resulting in more evaporation and, hence, more precipitation for the heterogeneous cases.

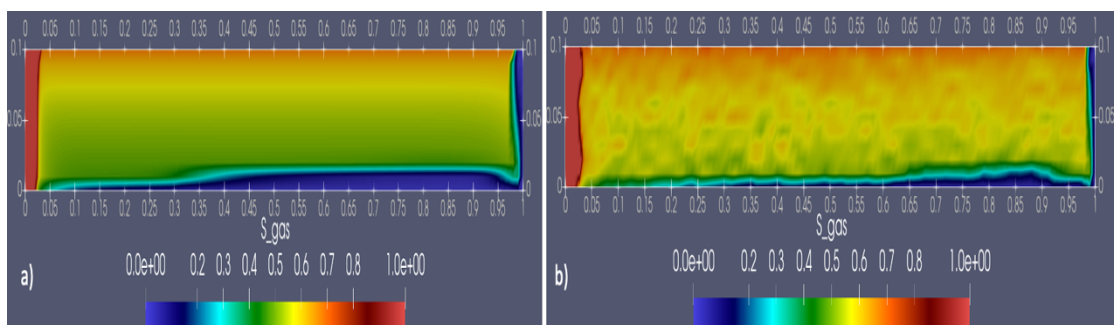


Figure 53 a) 2-D representation of gas saturation after 10PV (Homogeneous); b) 2-D representation of gas saturation after 10PV (Heterogeneous).

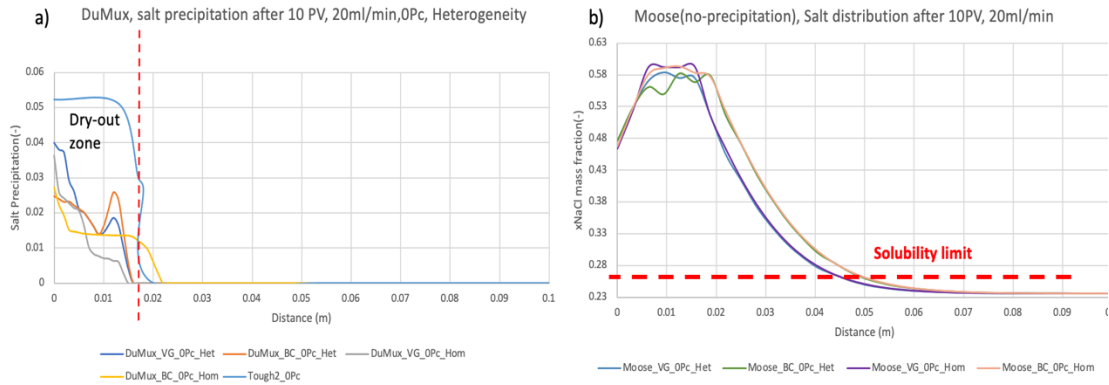


Figure 54 a) Salt precipitation along the domain after 10PV injected using DuMux; b) Mass fraction of NaCl in brine along the domain after 10PV injected using Moose.

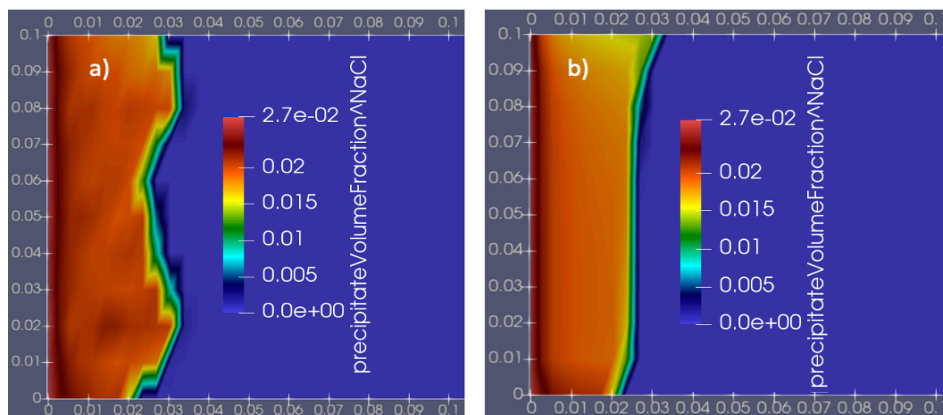


Figure 55 a) Salt precipitation at the inlet after 10PV injected for heterogeneous case; b) Salt precipitation at the inlet after 10PV was injected for a homogeneous case.

3. Effect of capillary pressure on gas saturation and salt precipitation

Capillary pressure can be considered the most influential parameter in the localization of precipitation. In numerical simulations, the magnitude of capillary pressure is dictated by pore-geometry distribution, for the BC capillary pressure model the pore-geometry factor is represented by $\underline{\lambda}$, while for the VG by $\underline{\alpha}$. The simulation domains with higher capillary pressure (more compacted grains) result in more significant capillary back-flow, affecting the localization of deposited salt. The results of the simulation cases have confirmed the generally accepted behavior when the capillary pressure provides an additional supply of fresh brine to the drying front. In terms of front propagation and spreading of the gas saturation, there is a clear effect from the capillary pressure (Figure 56 and Figure 57). The front becomes more stable and homogeneous with slight gravity overrun, this is due to greater influence from capillary forces than from the heterogeneity channeling, resulting in the front smeared out. The

lower gas saturation is denoted by constant capillary back flow, bringing the fresh brine closer to the inlet (Figure 56(c)(d)). Hence, the distinguishable dry-out front has not been formed after 10PV was injected, requiring more volume of CO₂ and time for its formation. From Figure 57, it can be noted that there is a pronounced saturation gradient, which is governed by the capillary end-effect, signifying a geometrical property. However, in laboratory core scale experiments this capillary end effect is inhibited by capillary forces, mainly capillary redistribution due to back flow. In addition, Ott et al. (2015) have assumed based on the experimental data that water evaporates over the entire core length, equalizing the brine saturation by the presence of constant back flow, neglecting the end effect. The next Figure 58 provides comparable results for the gas saturation at the inlet. It can be concluded that there is a slight overestimation from the TOUGH2, due to different input parameters – the VG model for the capillary pressure and homogeneity of the domain.

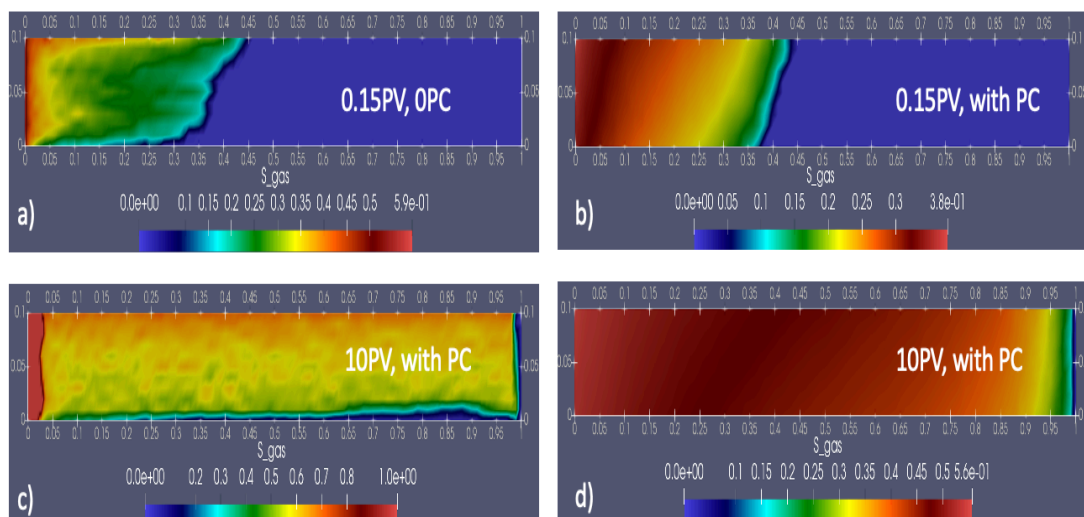


Figure 56 a) Gas saturation along the domain after 0.15PV injected without Pc; b) Gas saturation after 0.15PV injected with the effect of Pc; c) Gas saturation after 10PV injected without the effect of Pc; d) Gas saturation after 10PV injected with the effect of Pc.

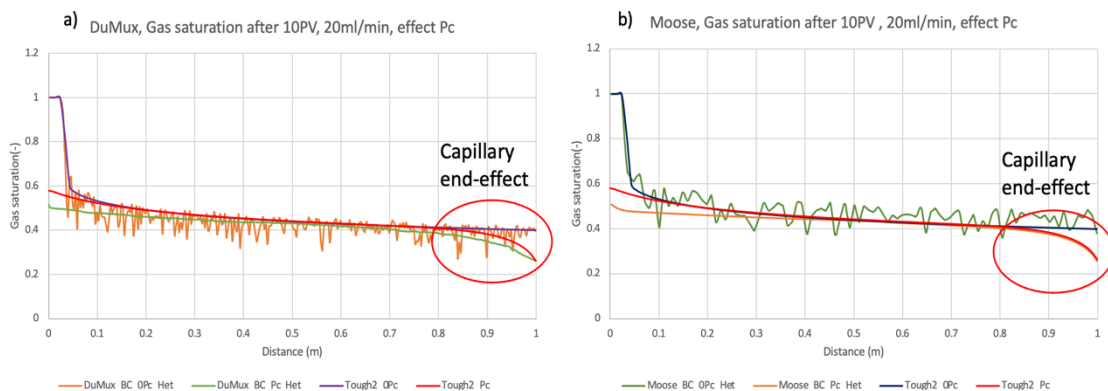


Figure 57 a) Comparison of Pc/no Pc gas saturation distribution along the domain after 10PV injected using DuMux; b) Gas saturation distribution along the domain after 10PV injected using Moose.

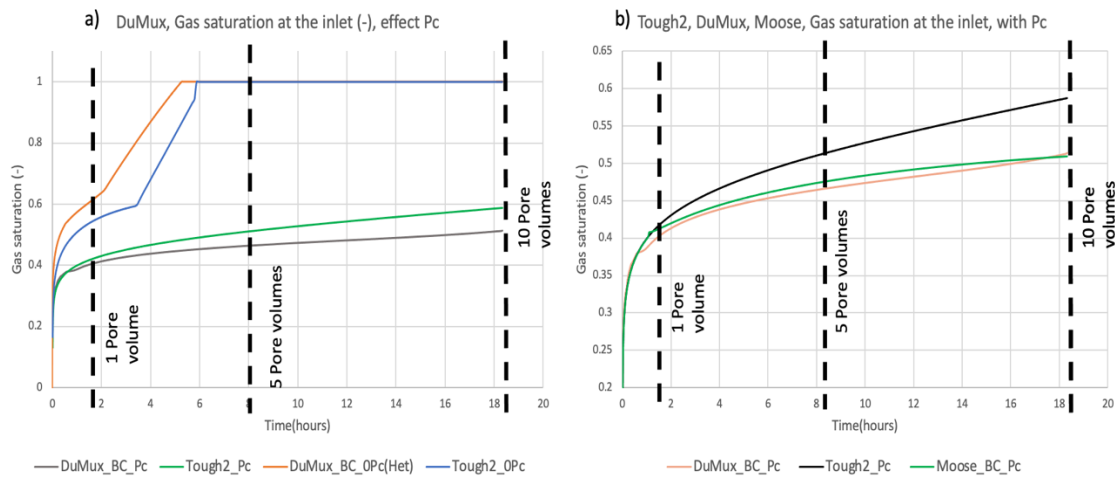


Figure 58 a) Gas saturation at the inlet (1st grid cell) after 10PV injected using DuMux, capillary pressure evaluation; b) Comparison of the simulators with active capillary pressure

Results show that the appearance of the capillary pressure gradient induces the capillary-driven back flow which drives the brine toward the dry-out region, making the evaporation and precipitation processes continuous and more dominant versus time. Furthermore, since more water is evaporated in the dry CO₂ stream, a higher concentration of salt in the trapped brine is observed, leading to more salt deposition. In Figure 59 and Figure 60 the significantly higher solid salt concentration can be noted, in addition to more localized salt precipitation at the inlet. Activation of the capillary pressure has resulted in a spike in salt deposition from 5% to 30%. All three simulators have shown matchable results and similar precipitation patterns (Figure 59), where the cases with acting capillary pressure have revealed higher solid saturation, which is mainly localized at the very inlet.

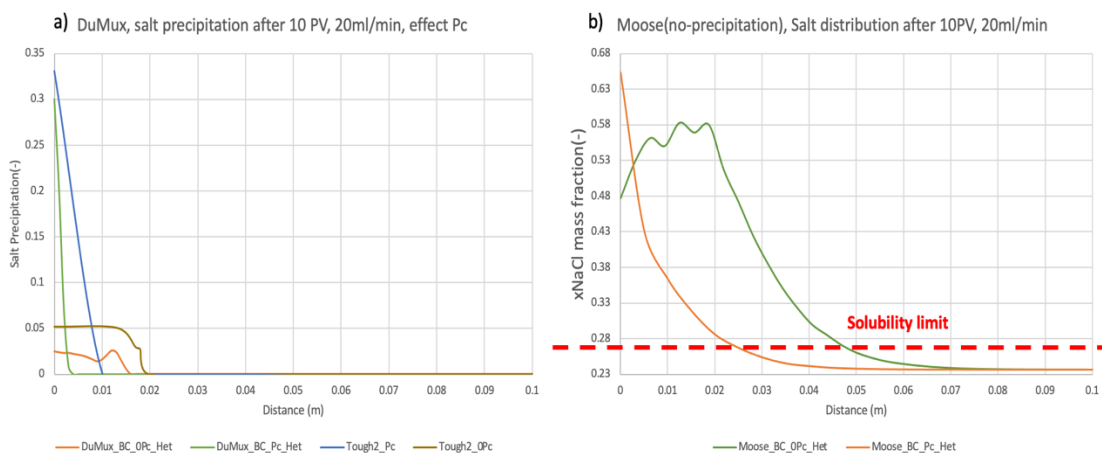


Figure 59 a) Salt precipitation along the domain after 10PV injected using DuMux, evaluating the effect of PC; b) Mass fraction of NaCl in brine along the domain after 10PV injected using Moose.

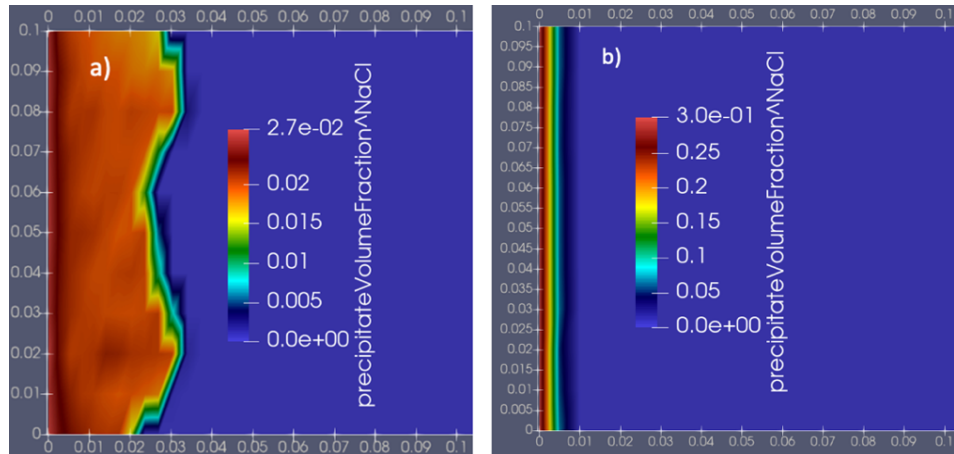


Figure 60 a) 2-D Salt precipitation at the inlet without P_c ; b) 2-D Salt precipitation at the inlet with acting P_c

The visual representation of capillary back flow is represented in Figure 61, where the arrows point towards the act of the capillary forces. Initially, in Figure 61(a) there is no back flow can be observed, however, with increasing gas saturation at the inlet and initialization of the dry-out front, the brine phase is brought back under capillary force towards the injection boundary. The capillary pressure gradients are largest at the dry-out. The final evaluation of the capillary pressure effect was performed by assessing permeability and porosity reduction (Figure 62). The more localized and higher deposits of salt precipitation have resulted in approximately 45% permeability reduction and 38% porosity reduction. However, it should be mentioned that both these parameters are coupled by the Kozeny-Carman grain model (Carman, 1939).

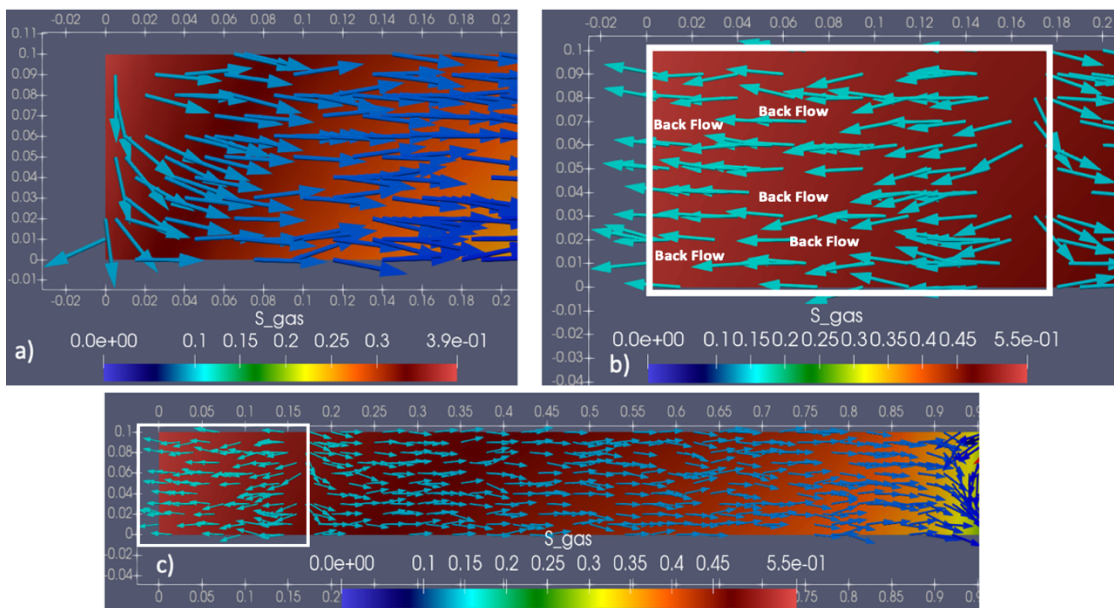


Figure 61 a) Action of capillary forces after 0.15PV injected; b) and c) Action of capillary forces after 10PV injected.

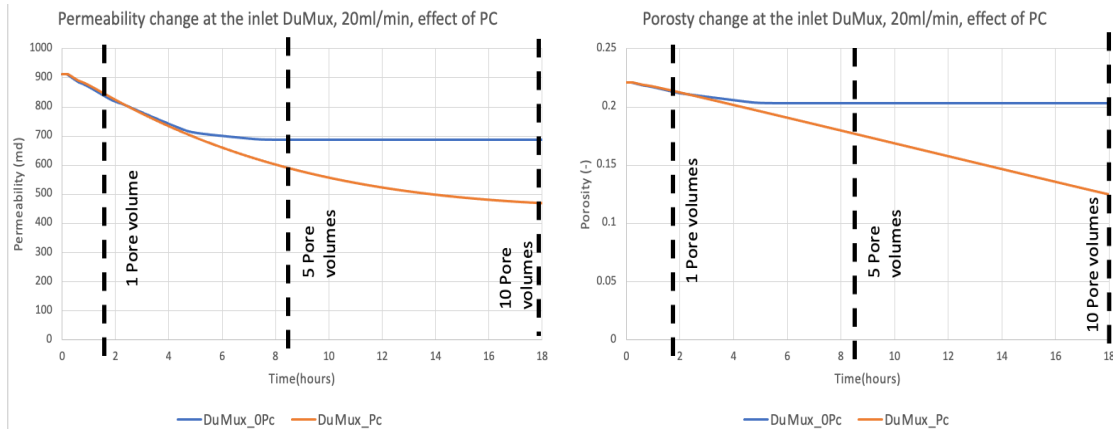


Figure 62 a) Permeability reduction at the inlet with Pc and without Pc; b) Porosity reduction at the inlet with Pc and without Pc

4. Evaluation of the lower injection rate of 2ml/min

The reduction of the injection rate to 2ml/min has not shown a significant difference in the magnitude and localization of the salt precipitation for both DuMux and TOUGH2, just a slightly higher solid concentration of about 2% was observed for the lower injection rate case (Figure 64). The possible explanation for this behavior is behind expertise between the capillary force and convective force. Figure 63 can be seen that a higher injection rate leads to higher capillary pressure, while lower capillary pressure for a lower injection rate respectively. Therefore, the higher capillary pressure governs the back flow effect for the 20ml/min and vice versa.

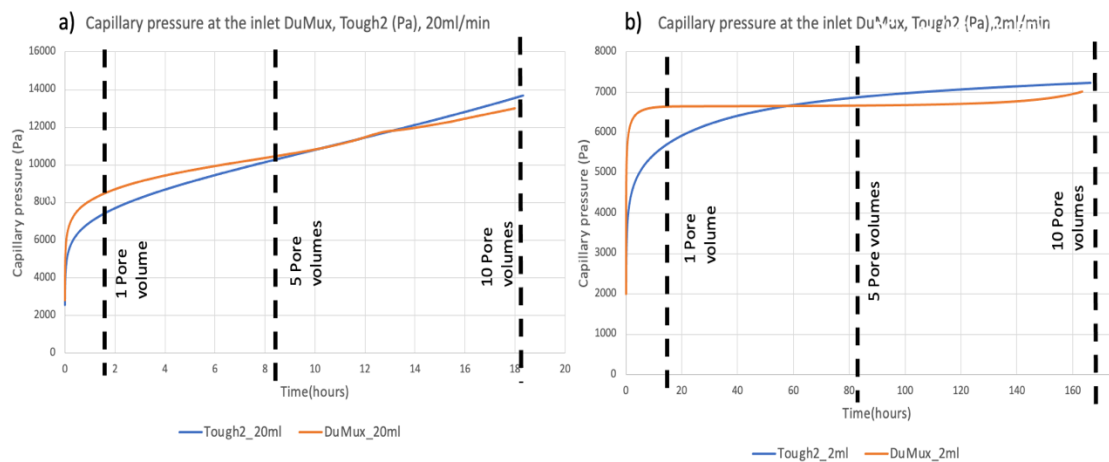


Figure 63 a) Capillary pressure evolution at the inlet injecting 20ml/min; b) a) Capillary pressure evolution at the inlet injecting 2ml/min

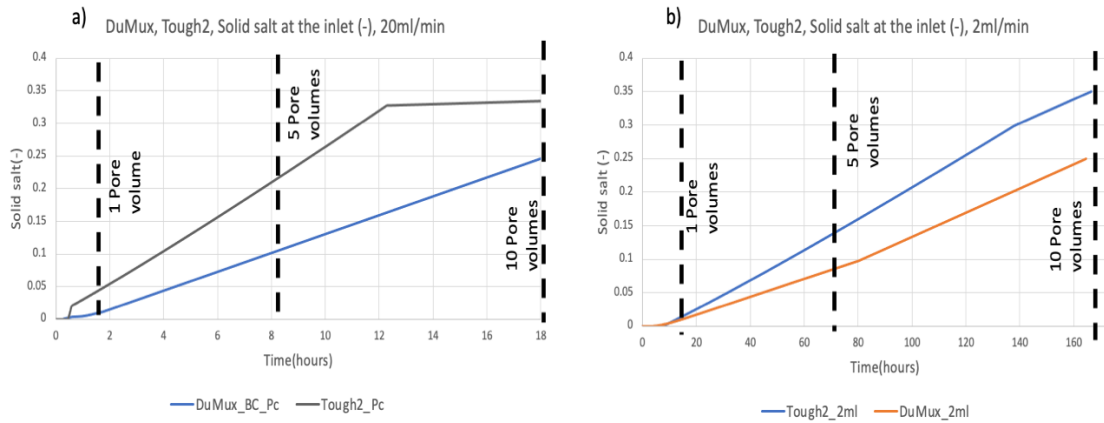


Figure 64 a) Solid salt at the inlet (1st grid cell) after 10PV injected using DuMux and TOUGH2, 20 ml/min; b) Solid salt at the inlet after 10PV injected using DuMux and TOUGH2, 2ml/min

5. Complete clogging at 25.5PV – 0 porosity and 0 permeability

The complete clogging of the inlet zone was observed after 25.5PV using DuMux software. However, a similar consequence was observed in TOUGH2 just slightly earlier, after around 23PV (Figure 66). The precipitate is homogeneously distributed around the injection area, completely covering just the first 0.03 cm of the investigated domain, resulting in the simulation shut down after approximately 45 hours of simulated time. In addition, the relatively small completely dry-out zone can be observed in Figure 67(a). The evolution of the permeability and porosity of the first grid block is represented in Figure 66(a)(b). It can be seen that the highest clogging and, hence, evaporation was observed between 1PV and 5PV injected, and the precipitation mechanism was activated just after 0.5PV injected or 1 hour of simulation time.

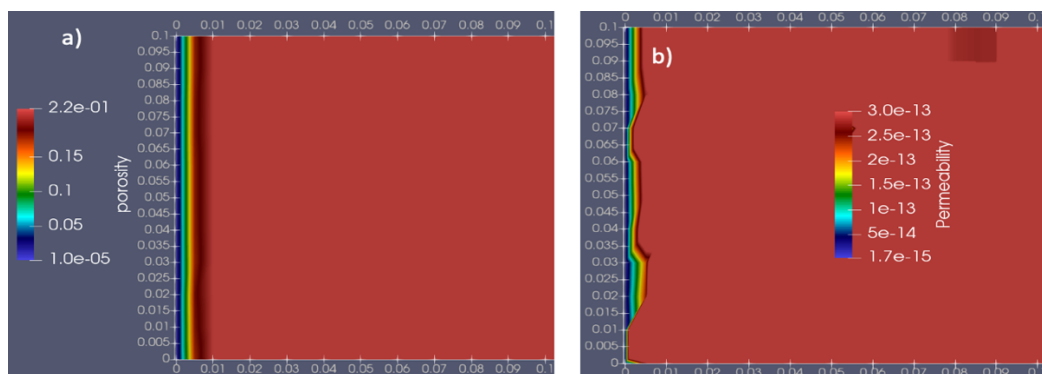


Figure 65 a) Porosity blockage at the inlet after 25.5PV injected; b) Permeability blockage at the inlet after 25.5PV injected

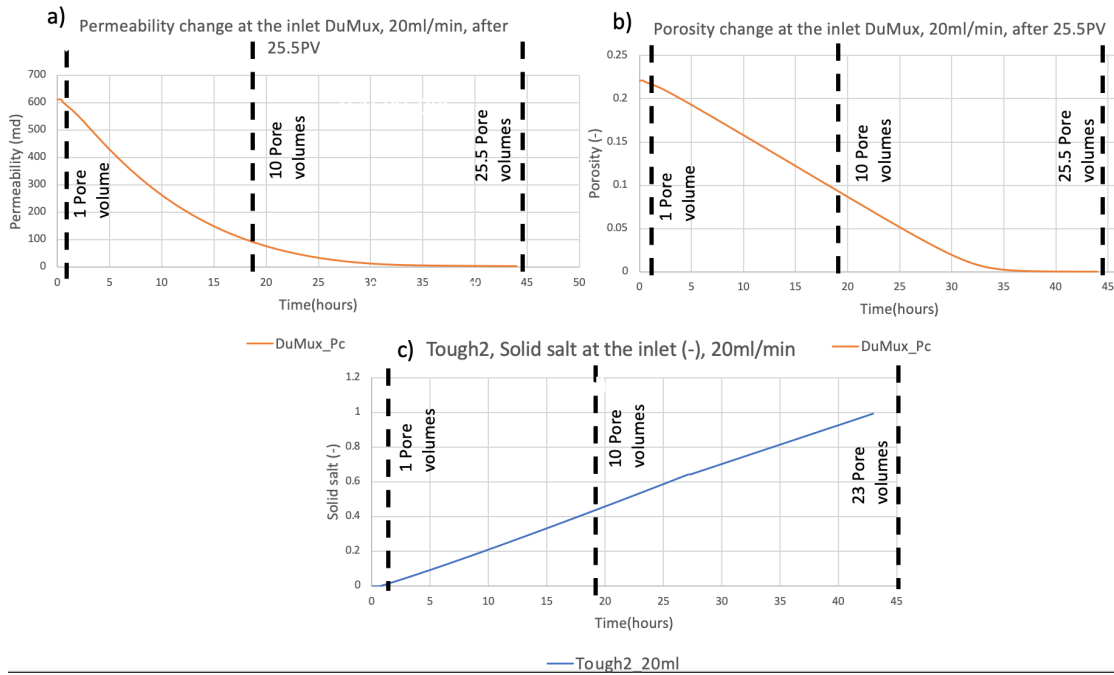


Figure 66 a) Permeability evolution at the first grid block after 25.5PV DuMux; b) Permeability evolution at the first grid block after 25.5PV DuMux; c) Solid salt concentration at the first grid block using TOUGH2

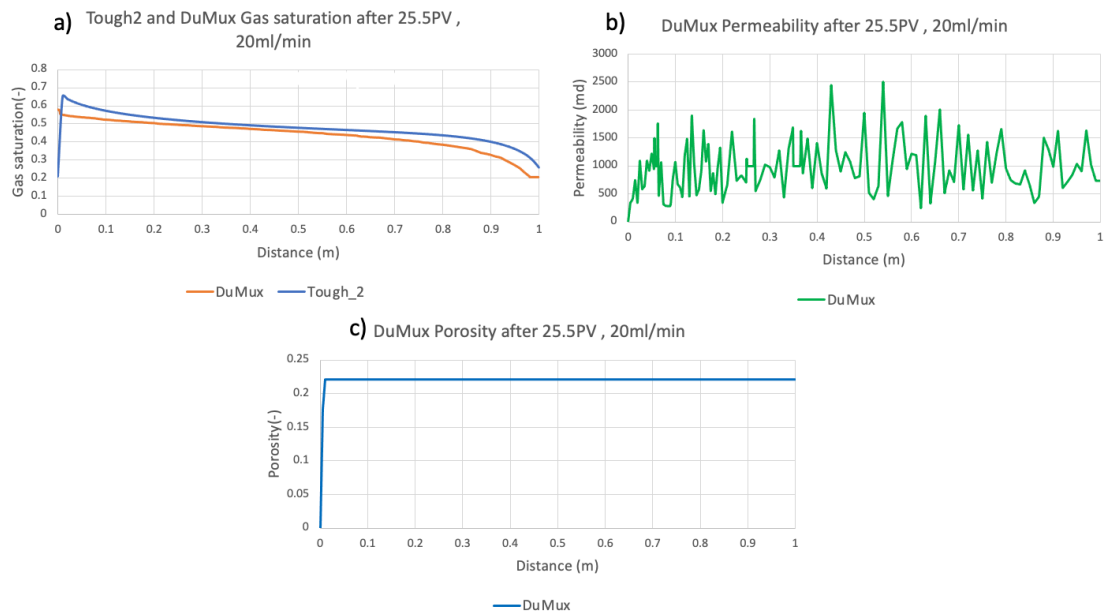


Figure 67 a) Gas saturation distribution along the domain after 25.5PV DuMux and TOUGH2; b) Permeability distribution along the domain after 25.5PV DuMux; c) Porosity distribution along the domain after 25.5PV.

6. 3-D model visualization

The final step was to perform the simulation in the 3-D domain, just for a better visual understanding of the salt distribution at the inlet and gas saturation (Figure 69) along the simulated core. It can be observed (Figure 68) that the highest NaCl concentration is located at the upper part of the inlet boundary, due to higher gas saturation at the top. It seems that due to gravity and buoyancy force the CO₂ has mostly migrated to the upper part, forming a dry-CO₂ flow, where the brine is evaporated.

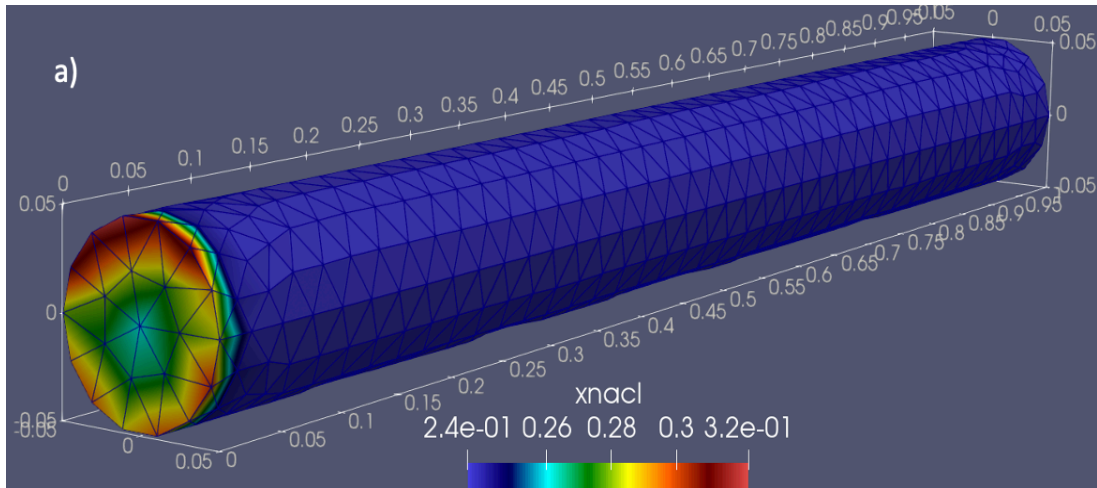


Figure 68 3-D representation of NaCl mass fraction in brine after 10PV injected, using Moose.

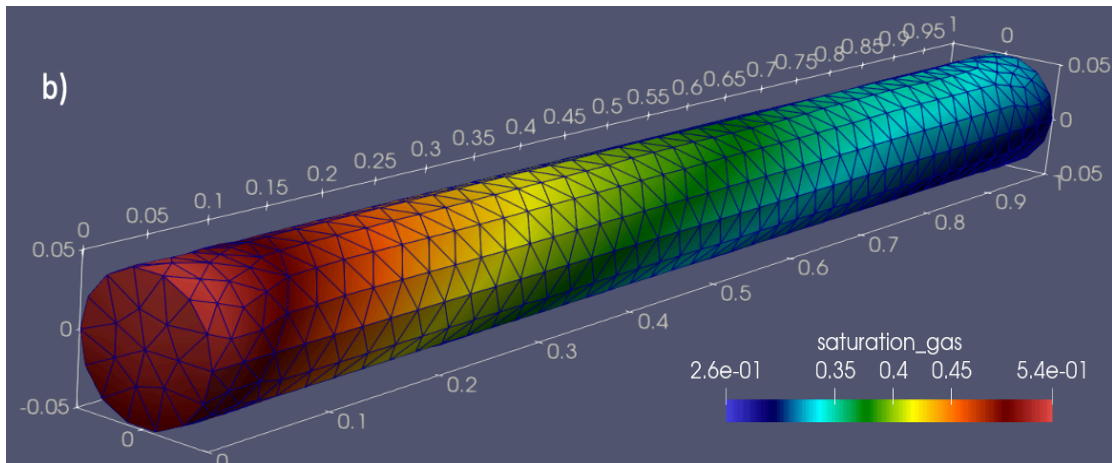


Figure 69 3-D representation of gas saturation after 10PV, using Moose.

Chapter 5

Conclusion

5.1 Summary

In this study, the application of the multiphysics frameworks Dumux and Moose for investigation of the CO₂/Brine displacement mechanisms and in principal salt precipitation due to brine evaporation was shown. In addition to the sensitivity analysis on the salt precipitation from the specific relative permeability models, heterogeneity, capillary pressure, and injection rate. It was a novel approach for incorporating formation drying-out and halite-precipitation modeling within the DuMux environment because no study has been done before using this tool and evaluating the drying-out mechanism due to constant scCO₂ injection. To do so, the base 2pnmin model was modified for implementation in conjunction with the fluid system where NaCl was considered as a separate component. For the Moose software, the input file was written with the requirements of the investigation and parameters for the dry-out analysis. The benchmark simulation cases were prepared for both simulators DuMux and Moose for future development. Because in this study only the local equilibrium assumption for the mutual solubilities between CO₂ and brine phases was considered. Both DuMux and Moose have shown successful modeling of the CO₂/Brine displacement process with the evaporation effect. The salting-out mechanism was only implemented within DuMux simulations. The validity of these multiphysics frameworks was proven by comparing the obtained results, mainly gas saturation propagation and magnitude of precipitation, with the well-known simulator TOUGH2. The good match was demonstrated along different simulation cases, demonstrating the ability of DuMux and Moose to cover a variety of physical mechanisms. The sensitivity analysis has revealed the importance of selecting the appropriate relative model for a more realistic simulation. Considering this study, the best results were obtained with the Brooks-Corey relative permeability and capillary pressure models. It was also mentioned that in these

scenarios the heterogeneity did not provide a significant effect on the magnitude of precipitation, just slightly changing the salt distribution near the injection boundary. Furthermore, the reduction of the injection rate from 20ml/min to 2ml/min has revealed just a minor change in the volume of salt precipitation. The possible explanation of this behavior was related to the growth of capillary pressure with higher injection rates, therefore, this increase in capillary pressure balances the effect of advective forces related to the injection influx. Finally, it was confirmed that with additional development the DuMux tool can be a good option for improving interpretations of laboratory experiments. Comparing these two simulators, DuMux has shown itself as more developed and more ultimate software for future CO₂/ CCS projects, although DuMux is more complex in use. Even though it has a structured system of input files, which can be easily modified and implemented to a certain need, there is no doubt that extensive work has to be done in the direction of providing more guidance towards user's friendly environment, where everything can be easily understood, for example, more meaningful and descriptive handbook.

5.2 Future Work

Although the benchmark models were developed, and the results are comparable with the TOUGH2 simulator, the main source of uncertainties still arises due to the local equilibrium assumption in the description of phase partitioning between CO₂ and brine. Therefore, the main task for future work is to develop the kinetic model for the CO₂ and brine phase partitioning within the DuMux environment. Since the local equilibrium approach overestimates the near injection clogging by salt accumulation. However, in real scenarios, the precipitation can happen significantly further under the governance of low flow velocities. For future work, a good starting point would be to investigate the part of the code represented in Figure 70, which in theory can be modified similarly as the Eq. (41), which describes the reaction kinetics mass transfer between phases.

```
// calculate fluxes
// liquid phase
Scalar evaporationRateMole = 0;
if (moleFracH2OInside - moleFracRefH2O > 0)
{
    evaporationRateMole = massTransferCoefficient
        * volVars.diffusionCoefficient(gasPhaseIdx, AirIdx, H2OIdx)
        * (moleFracH2OInside - moleFracRefH2O)
        / boundaryLayerThickness
        * volVars.molarDensity(gasPhaseIdx);
}
else
{
    evaporationRateMole = massTransferCoefficient
        * volVars.diffusionCoefficient(gasPhaseIdx, AirIdx, H2OIdx)
        * (moleFracH2OInside - moleFracRefH2O)
        / boundaryLayerThickness
        * 1.2;
```

Figure 70 The part of the 2pncmin base problem (DuMux), which can be considered for modification for future reaction kinetics model development.

References

- Ajayi, T., Gomes, J.S. & Bera, A. (2018) 'A review of CO₂ storage in geological formations emphasizing modeling, monitoring and capacity estimation approaches. *Pet. Sci.* **16**, 1028–1063 (2019). <https://doi.org/10.1007/s12182-019-0340-8>
- André, L., Peysson, Y. and Azaroual, M. (2014) 'Well injectivity during CO₂ storage operations in deep saline aquifers – Part 2: Numerical numerical simulations of drying, salt deposit mechanisms and role of capillary forces', *International Journal of Greenhouse Gas Control*, vol. 22, pp. 301–312.
- Altunin, V.V, (1975) *Thermophysical properties of carbon dioxide*, Publishing House of Standards, 551 pp
- Audigane, P., Chiaberge, C., Mathurin, F., Lions, J., & Picot-Colbeaux, G. (2011). A workflow for handling heterogeneous 3D models with the TOUGH2 family of codes: Applications to numerical modeling of CO₂ geological storage. *Computers & Geosciences*, 37(4), 610–620.
- Balay, S., Abhyankar, S., Adams, M., Brown, J., Brune, P., Buschelman, K., Dalcin, L., Eijkhout, V., Gropp, W., Kaushik, D., & others. (2019). *PETSc Users Manual*. Argonne National Lab. (ANL), Argonne, IL (United States).
- Bandilla, K. W., Celia, M. A., & Leister, E. (2014). Impact of Model Complexity on CO₂ plume modeling at Sleipner. *Energy Procedia*, 63, 3405–3415.
- Bear, J., (1972) *Dynamics of fluids in porous media*. Elsevier, New York
- Bennion, D. and Bachu, S., (2006). Dependence on temperature, pressure, and salinity of the IFT and relative permeability displacement characteristics of CO₂ injected in deep saline aquifers.
- Benson, S. M., & Cole, D. R. (2008). CO₂ Sequestration in Deep Sedimentary Formations. *Elements*, 4(5), 325–331. doi:10.2113/gselements.4.5.325

- Bette, S. and Heinemann, R. F. (1989) 'Compositional Modeling of High-Temperature Gas-Condensate Reservoirs With Water Vaporization', SPE Symposium on Reservoir Simulation. Houston, Texas, 1989-02-06, Society of Petroleum Engineers.
- Brooks, R.H., Corey, A.T., 1964. Hydraulic Properties of Porous Media. Hydrology Papers. Colorado State University, Fort Collins, CO.
- Burnside, N. and Naylor, M., 2014a. Review and implications of relative permeability of CO₂-brine systems and residual trapping of CO₂. *International Journal of Greenhouse Gas Control*, 23: 1-11.
- Carlson, C. A., Bates, N. R., Hansell, D. A. and Steinberg, D. K. (2009) 'Carbon Cycle', in Steele, J. H., Thorpe, S. A. and Turekian, K. K. (eds) *Encyclopedia of ocean sciences*, 2nd edn, San Diego, CA, Academic Press, pp. 477–486.
- Celia, M. A., Bachu, S., Nordbotten, J. M., & Bandilla, K. W. (2015). Status of CO₂ storage in deep saline aquifers with emphasis on modeling approaches and practical simulations. *Water Resources Research*, 51(9), 6846–6892.
- Class, H., Ebigbo, A., Helmig, R., Dahle, H. K., Nordbotten, J. M., Celia, M. A., ... Wei, L. (2009). A benchmark study on problems related to CO₂ storage in geologic formations. *Computational Geosciences*, 13(4), 409–434.
- Climate Central.(2022). Peak CO₂ & Heat-trapping Emissions. “Climate Matters”[Online]
- Corey, A. T. (1954), The interrelation between gas and oil relative permeabilities, *Prod. Mon.*, **19**, 38– 41.
- Detwiler, R. L., & Rajaram, H. (2007). Predicting dissolution patterns in variable aperture fractures: Evaluation of an enhanced depth-averaged computational model. *Water Resources Research*, 43(4).
- Doughty, C., and K. Pruess (1992), A similarity solution for two-phase water, air and heat flow near a linear heat source in a porous medium, *J. Geophys. Res.*, **97**(B2), 1821– 1838
- Duan, Z., R. Sun (2003), An improved model calculating CO₂ solubility in pure water and aqueous NaCl solutions from 273 to 533 K and from 0 to 2000 bar. *Chemical geology*, 193(3-4):257–271
- Garcia, J.E., (2001). Density of aqueous solutions of CO₂. Technical Report, LBNL
- Geuzaine.C, Remacle J.-F. (2009). Gmsh: a three-dimensional finite element mesh generator with built-in pre- and post-processing facilities. *International Journal for Numerical Methods in Engineering* 79(11), pp. 1309-1331.

- Ghafoori, M., Tabatabaei-Nejad, S. A., & Khodapanah, E. (2017). Modeling rock fluid interactions due to CO₂ injection into sandstone and carbonate aquifer
- Green, C. P., Ennis-King, J., La Force, T., & Wilkins, A. (2018). Community code for simulating CO₂ storage: Modelling multiphase flow with coupled geomechanics and geochemistry using the open-source multiphysics framework MOOSE. 14th Greenhouse Gas Control Technologies Conference Melbourne, 21-26 October 2018, 1–15.
- Grimm Lima, M., Schädle, P., Green, C. P., Vogler, D., Saar, M. O., & Kong, X.-Z. (2020). Permeability impairment and salt precipitation patterns during CO₂ injection into single natural brine-filled fractures. *Water Resources Research*, **56**(8), e2020WR027213.
- Hannah, L. J. (2015) *Climate change biology* [Online], 2nd edn, Amsterdam, Elsevier, Acad. Press. Available at <http://www.sciencedirect.com/science/book/9780124202184>.
- IEA, (2022) *Bioenergy with Carbon Capture and Storage* [Online]
- Intergovernmental Panel on Climate Change (2005) *Carbon Dioxide Capture and Storage*.
- Intergovernmental Panel on Climate Change (2022) *IPCC assessment report*, Geneva, IPCC Secretariat.
- Jones, T. A., & Detwiler, R. L. (2019). Mineral precipitation in fractures: Using the level set method to quantify the role of mineral heterogeneity on transport properties. *Water Resources Research*.
- Juanes et al., 2006 R. Juanes, E.J. Spiteri, F.M. Orr Jr., M.J. Blunt Impact of relative permeability hysteresis on geological CO₂ storage *Water Resources Research*, 42 (2006), p. W12418
- Kelly, H. L., & Mathias, S. A. (2018). Capillary processes increase salt precipitation during CO₂ injection in saline formations. *Journal of Fluid Mechanics*, **852**, 398–421.
- Kempka, T., Class, H., Görke, U.-J., Norden, B., Kolditz, O., Kühn, M., Walter, L., Wang, W., & Zehner, B. (2013). A Dynamic Flow Simulation Code Intercomparison based on the Revised Static Model of the Ketzin Pilot Site. *Energy Procedia*, 40, 418–427. <https://doi.org/10.1016/j.egypro.2013.08.048>
- Kim, K.-Y., Han, W. S., Oh, J., Kim, T. and Kim, J.-C. (2012) 'Characteristics of Salt Precipitation and the Associated Pressure Build-Up during CO₂ Storage in Saline Aquifers', *Transport in Porous Media*, vol. 92, no. 2, pp. 397–418.
- Kirk, B. S., Peterson, J. W., Stogner, R. H., & Carey, G. F. (2006). libMesh: a C++ library for parallel adaptive mesh refinement/coarsening simulations. *Eng. Comp.*, 22(3-4), 237–254. <https://doi.org/10.1007/s00366-006-0049-3>

Koch, T., Gläser, D., Weishaupt, K., Ackermann, S., Beck, M., Becker, B., ... Flemisch, B. (2020). DuMux 3 – an open-source simulator for solving flow and transport problems in porous media with a focus on model coupling. *Computers & Mathematics with Applications*.

Krevor, S.C.M., Pini, R., Zuo, L., Benson, S.M., 2012. Relative permeability and trapping of CO₂ and water in sandstone rocks at reservoir conditions. *Water Resour. Res.* 48.

Lindsay A, Stogner R, Gaston D, Schwen D, Matthews C, Jiang W, et al.,(2022). 2.0 - MOOSE: Enabling massively parallel Multiphysics simulation. <https://doi.org/10.1016/j.softx.2022.101202>.

Loria, P., & Bright, M. B. H. (2021). Lessons captured from 50 years of CCS projects. *The Electricity Journal*, 34(7), 106998.

Maldal T. and Tappel, I.M., 2004, CO₂ underground storage for Snøhvit gas field development, *Energy*, 29: 1403–1411.

Masoudi, M., Fazeli, H., Miri, R. and Hellevang, H. (2021) 'Pore scale modeling and evaluation of clogging behavior of salt crystal aggregates in CO₂-rich phase during carbon storage', *International Journal of Greenhouse Gas Control*, vol. 111, p. 103475.

Miri, R. and Hellevang, H. (2016) 'Salt precipitation during CO₂ storage—A review', *International Journal of Greenhouse Gas Control*, vol. 51, pp. 136–147.

Miri, R., van Noort, R., Aagaard, P. and Hellevang, H. (2015) 'New insights on the physics of salt precipitation during injection of CO₂ into saline aquifers', *International Journal of Greenhouse Gas Control*, vol. 43, pp. 10–21.

Muller, N., Qi, R., Mackie, E., Pruess, K. and Blunt, M. J. (2009) 'CO₂ injection impairment due to halite precipitation', *Energy Procedia*, vol. 1, no. 1, pp. 3507–3514.

Niessner, J., Hassanizadeh, S. M., & Crandall, D. (2008). *Modeling Two-Phase Flow in Porous Media Including Fluid-Fluid Interfacial Area*. Volume 12: Mechanics of Solids, Structures and Fluids.

Nooraiepour, M., Fazeli, H., Miri, R., & Hellevang, H. (2018). Effect of CO₂ phase states and flow rate on salt precipitation in shale caprocks a mi933 crofluidic study. *Environmental Science & Technology*, 52 , 6050–6060.

Norouzi, A. M., Niasar, V., Gluyas, J. G., & Babaei, M. (2022). Analytical solution for predicting salt precipitation during CO₂ injection into saline aquifers in presence of capillary pressure. *Water Resources Research*, 58, e2022WR032612.

- Oh, J., Kim, K.-Y., Han, W. S., Kim, T., Kim, J.-C. and Park, E. (2013) 'Experimental and numerical study on supercritical CO₂/brine transport in a fractured rock: Implications of mass transfer, capillary pressure and storage capacity', *Advances in Water Resources*, vol. 62, pp. 442–453.
- Oostrom, M., White, M. D., Porse, S. L., Krevor, S. C. M., & Mathias, S. A. (2016). Comparison of relative permeability–saturation–capillary pressure models for simulation of reservoir CO₂ injection. *International Journal of Greenhouse Gas Control*, 45, 70–85.
- Ott, H., Kloe, K. de, Marcelis, F. and Makurat, A. (2011) 'Injection of supercritical CO₂ in brine saturated sandstone: Pattern formation during salt precipitation', *Energy Procedia*, vol. 4, pp. 4425–4432.
- Ott, H., Snippe, J., Kloe, K. de, Husain, H. and Abri, A. (2013) 'Salt Precipitation Due to Sc-gas Injection: Single Versus Multi-porosity Rocks', *Energy Procedia*, vol. 37, pp. 3319–3330.
- Ott, H., Andrew, M., Snippe, J. and Blunt, M. J. (2014) 'Microscale solute transport and precipitation in complex rock during drying', *Geophysical Research Letters*, vol. 41, no. 23, pp. 8369–8376.
- Ott, H., Roels, S. M. and Kloe, K. de (2015) 'Salt precipitation due to supercritical gas injection: I. Capillary-driven flow in unimodal sandstone', *International Journal of Greenhouse Gas Control*, vol. 43, pp. 247–255.
- Ott, H., Snippe, J. and Kloe, K. de (2021) 'Salt precipitation due to supercritical gas injection: II. Capillary transport in multi porosity rocks', *International Journal of Greenhouse Gas Control*, vol. 105, p. 103233.
- Pan, L., Spycher, N., Doughty, C., & Pruess, K. (2015). ECO₂N V2.0: A TOUGH2 fluid property module for modeling CO₂-H₂O-NACL systems to elevated temperatures of up to 300°C. *Greenhouse Gases: Science and Technology*, 7(2), 313–327.
- Patel, S. (2019), What Are Supercritical CO₂ Power Cycles? [Online].
- Perrin, J.-C., Benson, S., 2010. An experimental study on the influence of sub-core scale heterogeneities on CO₂ distribution in reservoir rocks. *Transp. Porous Media* 82 (1), 93–109.
- Peysson, Y. (2012) 'Permeability alteration induced by drying of brines in porous media', *The European Physical Journal Applied Physics*, vol. 60, no. 2, p. 24206.
- Preston, C., Monea, M., Jazrawi, W., Brown, K., Whittaker, S., White, D., Law, D., Chalaturnyk, R. and Rostron, B. (2005) 'IEA GHG Weyburn CO₂ monitoring and storage project', *Fuel Processing Technology*, vol. 86, 14-15, pp. 1547–1568.

Pruess, K. (2004), The TOUGH codes—A family of simulation tools for multiphase flow and transport processes in permeable media, *Vadose Zone J.*, **3**, 738– 746.

Pruess, K. (2005), ECO2N: A TOUGH2 fluid property module for mixtures of water, NaCl, and CO₂, Rep. LBNL-57952, Lawrence Berkeley Natl. Lab., Berkeley, Calif.

Pruess, K., & Spycher, N. (2007). ECO2N – A fluid property module for the TOUGH2 code for studies of CO₂ storage in saline aquifers. *Energy Conversion and Management*, 48(6), 1761–1767.

Pruess, K. and Müller, N. (2009) 'Formation dry-out from CO₂ injection into saline aquifers: 1. Effects of solids precipitation and their mitigation', *Water Resources Research*, vol. 45, no.3.

Parvin, S., Masoudi, M., A. Sundal, R.Miri (2020) 'Continuum scale modelling of salt precipitation in the context of CO₂ storage in saline aquifers with MRST compositional _ Elsevier Enhanced Reader'.

Roels, S. M., Ott, H., & Zitha, P. L. J. (2014). μ -CT analysis and numerical simulation of drying effects of CO₂ injection into brine-saturated porous media. *International Journal of Greenhouse Gas Control*, 27, 146–154.

Saadatpoor E, Bryant S, Sepehrnoori K., (2010) New trapping mechanism in carbon sequestration. *Transport in Porous Media*;82(1):3—17.

Shell U.K. Limited Peterhead CCS Project: Stakeholder and Public Engagement and Stakeholder and Public Engagement and Communications Plan [Online].

Schumer C., Boehm S., Fransen.T., (2022) '6 Takeaways from the 2022 IPCC Climate Change Mitigation Report'. World resources insittitute.

Span,R and Wagner W.,(1996) "A New Equation of State for Carbon Dioxide Covering the Fluid Region from the Triple-Point Temperature to 1100 K at Pressures up to 800 MPa," *J. Phys. Chem. Ref. Data*, vol. 25, no. 6, pp. 1509–1596.

Spycher, N., Pruess, K., & Ennis-King, J. (2003). CO₂-H₂O mixtures in the geological sequestration of CO₂. I. Assessment and calculation of mutual solubilities from 12 to 100°C and up to 600 bar. *Geochimica et Cosmochimica Acta*, 67(16), 3015–3031.

Spycher, N., & Pruess, K. (2004). Partitioning in Chloride brines at 12-100°C and up to 600 bar (Vol. 9). CO₂-H₂O mixtures in the geological sequestration of CO₂.

Spycher, N., and K. Pruess (2005), CO₂-H₂O mixtures in the geological sequestration of CO₂. II. Partitioning in chloride brines at 12–100°C and up to 600 bar, *Geochim. Cosmochim. Acta*, **69**(13), 3309– 3320.

- Spycher, N., & Pruess, K. (2009). A Phase-Partitioning Model for CO₂-Brine Mixtures at Elevated Temperatures and Pressures: Application to CO₂-Enhanced Geothermal Systems. *Transport in Porous Media*, 82(1), 173–196.
- Steele, J. H., Thorpe, S. A. and Turekian, K. K. (eds) (2009) *Encyclopedia of ocean sciences*, 2nd edn, San Diego, CA, Academic Press.
- Tatomir, A., Dimache, A.-N., Iulian, I., & Sauter, M. (2019). Modelling of CO₂ storage in geological formations with DuMux, a free-open-source numerical framework. A possible tool to assess geological storage of carbon dioxide in Romania. *E3S Web of Conferences*, 85, 07002.
- The DuMux developers. (2022). *Dumux handbook v3.3*. <https://dumux.org/docs/handbook/releases/3.3/dumux-handbook.pdf>
- The Global CCS Institute (2022) Carbon capture and storage images [Online].
- Townsend and Gillespie, (2020) *Scaling Up the CCS Market to Deliver Net-Zero Emissions.*, p.14.
- van Genuchten, M. T. A. (1980), Closed-form equation for predicting the hydraulic conductivity of unsaturated soils, *Soil Sci. Soc. Am. J.*, **44**, 892– 898.
- Verma, A. and Pruess, K. (1988) 'Thermohydrological conditions and silica redistribution near high-level nuclear wastes emplaced in saturated geological formations', *Journal of Geophysical Research*, vol. 93, B2, p. 1159.
- Y. Wang, E. Mackie, J. Rohan, T. Luce, R. Knabe and M. Appel (2009) 'Experimental Study on Halite Precipitation During CO₂ Sequestration'.
- Y. Wang, T. Lucea, C. Ishizawa, M. Shuck, K. Smith, H. Ott and M. Appel (2010) 'Halite Precipitation and Permeability During Supercritical CO₂ Core Flood'.
- Wang, Y., Ren, J., Hu, S., & Feng, D. (2017). Global Sensitivity Analysis to Assess Salt Precipitation for CO₂ Geological Storage in Deep Saline Aquifers. *Geofluids*, 2017, 1–16.
- William F Lamb et al 2021 *Environ. Res. Lett.* **16** 073005.
- Wilkins et al., (2020). PoroFlow: a multiphysics simulation code for coupled problems in porous media. *Journal of Open Source Software*, 5(55), 2176 .
- World Meteorological Organization (WMO) (2021) 'Greenhouse Gas Bulletin: Another Year Another Record' The World Meteorological Organization is the United Nations [Online]

List of Figures

Figure 1 Globally averaged greenhouse gas concentrations and global anthropogenic CO ₂ emissions (IPCC, 2014).....	12
Figure 2 Comparison of CO ₂ emissions from fossil fuel projects vs. global CO ₂ limits (C. Schumer et al, 2022).....	12
Figure 3 Globally averaged CO ₂ mole fraction (left) and its growth rate (right) from 1984 to 2020. Increases in successive annual means are shown as the shaded columns on (right). The red line on (left) is the monthly mean with the seasonal variation removed; the blue dots and blue line on (left) depict the monthly averages (WMO Global Atmosphere Watch, 2021). ...	13
Figure 4 Overview of the suitable geological formations for carbon dioxide storage (Global CCS Institute, 2022).....	14
Figure 5 Number of CCS facilities by scale, location, and phase of development as of June 2021 (P. Loria 2021).....	15
Figure 6 Different CO ₂ trapping mechanisms during the geological storage process (T. Ajayi et al, 2019).....	16
Figure 7 Governing processes after the injection of CO ₂ into saline aquifers (IPCC Special Report, 2005).....	17
Figure 8 CO ₂ trapping mechanisms at Geologic CO ₂ Sequestration sites (Jun, Young-Shin & Zhang, Lijie & Min, Yujia & Li, Qingyun., 2017).....	18
Figure 9 Phase diagram of CO ₂ (S.Patel, 2019).	20
Figure 10 Schematic of the CO ₂ injection front, with the thickness of the CO ₂ denoted by $h(r,t)$, and the drying front, with thickness denoted by $i(r,t)$ (Nordbotten and Celia, 2006a).	21
Figure 11 Dissolved CO ₂ mass fraction in brine - comparison between MOOSE and TOUGH2 (C. Green., et al, 2018).	27
Figure 12 Immiscible displacement of brine by CO ₂ (Berg and Ott, 2012).....	29
Figure 13 Flood displacement simulation model with 0 Pc and different Corey exponents (Berg and Ott, 2012).	30
Figure 14 Transition from unstable to stable displacement with increasing IFTs – Pc (Corey exponents were the same) (Berg and Ott, 2012).	31
Figure 15 Gas saturation after 30 years of injection into Berea sandstone using the (a) Brooks-Corey, (b) van Genuchten relative permeability and capillary pressure models(M. Oostrom, et al., 2015).	33
Figure 16 Conceptual propagation front separation into three zones, due to dry-out. L – length of the front from the injected well; X_{disp} and X_{dry} are the length of the displacement and the dry-out fronts, respectively; $S_{g, dry}$ and $S_{g, disp}$ are the saturations of CO ₂ at the dry-out zone and displacement front, respectively; X^L – the solubility limit salt mass fraction in brine, and $X_{NaCl,i}$ – the initial salt mass fraction (G.Lima et al., 2020).	35
Figure 17 a) Two-phase displacement of Brine by CO ₂ , formation of the gravity overrun due to buoyancy and capillary pressure back flow due to saturation differences between the swept zone with residual saturation and the zone where displacement has not happened yet. b) Increase of capillary pressure, increase of the back flow, and formation of the bypassed brine in the form of residual saturation and brine film around the grains c) Capillarity of salt drives more brine on films around the grains, initiating the evaporation process into the dry-out zone. d) Precipitation of salt and further self-enhancement leading to clogging of CO ₂ pathways, which eventually can lead to complete clogging of the pore throats.	36
Figure 18 Capillary regime signifies massive salt accumulation due to salt capillary suction.	38
Figure 19 Evaporative regime provides the homogeneous salt distribution along the migration path of the brine around the grains.	39
Figure 20 Comparison of solid saturations using kinetic and local equilibrium (TOUGH2) mutual solubilities models (Roels et al., 2014).	41
Figure 21 Sensitivity analysis of injection rates (adapted from Kim et al., 2012).	42
Figure 22 The zone of attraction as a function of injection rate (H.Ott et al.,2015).	43

Figure 23 a) Comparison of kinetic and equilibrium models; b) Sensitivity analysis of injection rates (S.Parvin et al., 2020).....	43
Figure 24 left) the case with no capillary pressure; right) the case with capillary effect (localized salt saturation) (A. M. Norouzi et al., 2022).....	45
Figure 25 a) The possible combination of phases in the water-CO ₂ system; b) The schematic representation of phase partitioning (Pan et al., 2015).	47
Figure 26 CO ₂ mass evaluation with ECLIPSE, TOUGH2, and DuMux simulators (Kempka et al., 2013).....	48
Figure 27 CO ₂ /Brine phases partitioning (part of the code): a)Pre-calculation using Pruess and Spycher's (2004) approach; b) Phase composition calculation within the model.	49
Figure 28 Viscosity of brine calculated as a separate component.	50
Figure 29 Liquid density of CO ₂ and Water in the compositional fluid system	50
Figure 30 Part of the main.cc file, with defined solvers and assemblers.	51
Figure 31 Part of the params.the input file, with defined conditions and parameters.	51
Figure 32 Part of the problem.hh file, the example of the salt precipitation mechanism (when the NaCl solubility limit is exceeded), defined as a source term.	52
Figure 33 Part of the spatialparams.hh file, where the relative permeability/capillary and reference parameters for the Kozeny-Carman models are pre-defined.	52
Figure 34 Primary variables in miscible two-phase mode, where P a represents the pressure of phase a, T denotes the temperature, X_a^k is the mass fraction of component k in phase a and S is the saturation of the phase a (C.Green, A.Wilkins, 2018).	53
Figure 35 a) The mesh description; b) The brine phase flow equation as input (mass and advective terms).....	54
Figure 36 a) The definition of a non-linear variable, several phases, and some components, an example of the Brooks-Corey capillary pressure input; b) Example of the Brooks-Corey relative permeability input.....	54
Figure 37 a) The example of the inflow(source) boundary; b) the example of the outflow boundary related to the liquid phase of the CO ₂ component.	54
Figure 38 Boundary conditions of the 2-D simulations.	57
Figure 39 Boundary conditions of the 3-D simulations.	57
Figure 40 a) The relative permeability curves; b) The capillary pressure curves for Berea sandstone (adopted from Krevor et al.,2012; Oostrom et al.,2016).	58
Figure 41 Permeability distribution for the heterogeneous simulation in Moose.	58
Figure 42 Permeability distribution for the heterogeneous simulation in DuMux.....	58
Figure 43 a) Saturation front propagation comparing Brooks-Corey(BC) and Van Genuchten(VG) models, after 800 seconds using Moose; b) Using DuMux; c) Comparison of front propagation for Moose, DuMux and TOUGH2.....	60
Figure 44 Visual representation of front propagation for (left) Brooks-Corey,(right) Van Genuchten relative permeability models, without capillary pressure.....	60
Figure 45 a) Gas saturation distribution along the core after 10PV injected (DuMux); b) Moose; c) Comparison between DuMux, Moose, and TOUGH2.	61
Figure 46 a) Gas saturation distribution along the core after 10PV injected using BC model; b) Gas saturation using VG model; c) The extent of the dry-out zone and salt precipitation using BC model; d) Salt precipitation using VG model.....	61
Figure 47 a) Gas saturation at the inlet (1 st grid cell) after 10PV injected using DuMux, comparing BC and VG models; b) Gas saturation at the inlet after 10PV injected using Moose; c) The comparison between simulators using different relative permeability models.	62
Figure 48 a) Precipitated salt distribution along the domain after 10PVI; b) Evolution of salt precipitation at the inlet with the time.	62
Figure 49 a) Saturation front propagation comparing Homogeneous and Heterogeneous models, after 800 seconds using Moose; b) Using DuMux.	63
Figure 50 a) and b) Comparison of BC model for Homogeneous/Heterogeneous cases; c) and d) Comparison of VG model for Homogeneous/Heterogeneous cases.....	64

Figure 51 a) Gas saturation(dry-out) along the domain after 10PV injected in Moose; b) Gas saturation(dry-out) after 10PV injected in DuMux.	64
Figure 52 a) Gas saturation at the inlet (1 st grid cell) after 10PV injected using DuMux, heterogeneity evaluation; b) Gas saturation at the inlet after 10PV injected using Moose.....	65
Figure 53 a)2-D representation of gas saturation after 10PV (Homogeneous);b) 2-D representation of gas saturation after 10PV (Heterogeneous).....	65
Figure 54 a) Salt precipitation along the domain after 10PV injected using DuMux; b) Mass fraction of NaCl in brine along the domain after 10PV injected using Moose.	66
Figure 55 a) Salt precipitation at the inlet after 10PV injected for heterogeneous case; b) Salt precipitation at the inlet after 10PV was injected for a homogeneous case.	66
Figure 56 a) Gas saturation along the domain after 0.15PV injected without Pc; b) Gas saturation after 0.15PV injected with the effect of Pc; c) Gas saturation after 10PV injected without the effect of Pc; d) Gas saturation after 10PV injected with the effect of Pc.....	67
Figure 57 a) Comparison of Pc/no Pc gas saturation distribution along the domain after 10PV injected using DuMux; b) Gas saturation distribution along the domain after 10PV injected using Moose.....	67
Figure 58 a) Gas saturation at the inlet (1 st grid cell) after 10PV injected using DuMux, capillary pressure evaluation; b) Comparison of the simulators with active capillary pressure	68
Figure 59 a) Salt precipitation along the domain after 10PV injected using DuMux, evaluating the effect of PC; b) Mass fraction of NaCl in brine along the domain after 10PV injected using Moose.	68
Figure 60 a) 2-D Salt precipitation at the inlet without Pc; b) 2-D Salt precipitation at the inlet with acting Pc	69
Figure 61 a) Action of capillary forces after 0.15PV injected; b) and c) Action of capillary forces after 10PV injected.	69
Figure 62 a) Permeability reduction at the inlet with Pc and without Pc; b) Porosity reduction at the inlet with Pc and without Pc	70
Figure 63 a) Capillary pressure evolution at the inlet injecting 20ml/min; b) a) Capillary pressure evolution at the inlet injecting 2ml/min	70
Figure 64 a) Solid salt at the inlet (1 st grid cell) after 10PV injected using DuMux and TOUGH2,20 ml/min; b) Solid salt at the inlet after 10PV injected using DuMux and TOUGH2, 2ml/min.....	71
Figure 65 a)Porosity blockage at the inlet after 25.5PV injected; b) Permeability blockage at the inlet after 25.5PV injected	71
Figure 66 a) Permeability evolution at the first grid block after 25.5PV DuMux; b) Permeability evolution at the first grid block after 25.5PV DuMux; c)Solid salt concentration at the first grid block using TOUGH2.....	72
Figure 67 a)Gas saturation distribution along the domain after 25.5PV DuMux and TOUGH2; b) Permeability distribution along the domain after 25.5PV DuMux; c) Porosity distribution along the domain after 25.5PV	72
Figure 68 3-D representation of NaCl mass fraction in brine after 10PV injected, using Moose.	73
Figure 69 3-D representation of gas saturation after 10PV, using Moose.	73
Figure 70 The part of the 2pncmin base problem (DuMux), which can be considered for modification for future reaction kinetics model development.	76

List of Tables

Table 1 Injection rates - sensitivity analysis (adapted from Pruess and Müller, 2009).....	42
Table 2 Initial parameters of the simulated model.	56
Table 3 Data for modelling the relative permeability and capillary pressure (Oostrom et al.,2016).	57

Abbreviations

FE	Finite Element
PC	Capillary pressure
Kr	Relative Permeability
CCS	Carbon Capture and Storage
CO ₂	Carbon dioxide
ml/min	Millilitre per min
NaCl	Sodium Chloride
Ppm	Parts per million
BC	The Brooks Corey model
VG	The Van Genuchten model
PV	Pore Volume